UNIVERSITY OF CALIFORNIA SAN DIEGO

Jumbo Phages Assemble a Nucleus-Like Structure in *Pseudomonas*

A dissertation submitted in partial satisfaction of the
requirements for the degree Doctor of Philosophy

in

Biology

by

Katrina Tram Anh Nguyen

Committee in charge:

Professor Joe Pogliano, Chair
Professor Elizabeth Villa, Co-Chair
Professor Arshad Desai
Professor James Golden
Professor Justin Meyer
Professor Kit Pogliano

2019

The Dissertation of Katrina Tram Anh Nguyen is approved, and it is acceptable in quality and form for publication on microfilm and electronically:

_____

_____

_____

_____

_____
Co-Chair

_____
Chair

University of California San Diego

2019

TABLE OF CONTENTS

LIST OF FIGURES

LIST OF TABLES

ACKNOWLEDGEMENTS

I would like to acknowledge and thank Professor Joe Pogliano for his guidance and support from the very beginning of my scientific career and throughout the many years I have spent in his lab. I want to thank all the lab members and alumni. The combined Pogliano labs have been my home and my family for a decade now and I am so grateful. I would also like to thank my committee members for their wisdom and enthusiasm plus my family and friends for their love and support.

Chapter 2, in full, is a reprint of the material as it appears in the January 12, 2017 edition of *Science*. Chaikeeratisak, V., Nguyen, K., Khanna, K., Brilot, A.F., Erb, M.L., Coker, J.K., Vavilina, A., Newton, G.L., Buschauer, R., Pogliano, K., Villa, E., Agard, D.A., Pogliano, J. (2017). Assembly of a nucleus-like structure during viral replication in bacteria. *Science 355*, 194-197. The dissertation author was a significant contributor to this paper.

Chapter 3, in full, is a reprint of the material as it appears in the August 15, 2017 edition of *Cell Reports*. Chaikeeratisak, V., Nguyen, K., Egan M., Erb, M.L., Vavilina, A., Pogliano, J (2017). The Phage Nucleus and Tubulin Spindle Are Conserved among Large *Pseudomonas* Phages. *Cell Reports*, Volume 20, Issue 7, 1563 – 1571. The dissertation author was a significant contributor to this paper.

Chapter 4, in full, has been submitted for publication of the material as it may appear in *Cell*, 2019. Chaikeeratisak, V., Khanna, K., Nguyen, K., Sugie, J., Egan, M., Erb, M.L., Vavilina, A., Nonejuie, P., Pogliano, K., Nieweglowska, E., Villa, E., Agard,

D.A., Pogliano, J. (2019). Viral Capsid Trafficking along Treadmilling Tubulin Filaments in Bacteria. *Cell*. The dissertation author was a significant contributor to this paper.

Chapter 6 is currently being prepared for submission for publication of the material. This chapter was co-authored with Joseph Sugie, Kanika Khanna, MacKennon Egan, Chris Beierschmitt, Elizabeth Villa, and Joe Pogliano. The dissertation author was the primary investigator and author of this material.

VITA

2012	Bachelor of Science, University of California San Diego
2012-2013	Teaching Assistant, University of California San Diego
2019	Doctor of Philosophy, University of California San Diego

PUBLICATIONS

Chaikeeratisak, V., Khanna, K., **Nguyen, K**., Sugie, J., Egan, M., Erb, M.L., Vavilina, A., Nonejuie, P., Pogliano, K., Nieweglowska, E., Villa, E., Agard, D.A., Pogliano, J. (2019). Viral Capsid Trafficking along Treadmilling Tubulin Filaments in Bacteria. *Cell*.

Chaikeeratisak, V., **Nguyen, K**., Egan, M., Erb, M.L., Vavilina, A., Pogliano, J (2017). The Phage Nucleus and Tubulin Spindle Are Conserved among Large *Pseudomonas* Phages. *Cell Reports*, Volume 20, Issue 7, 1563 – 1571

Chaikeeratisak, V., **Nguyen, K**., Khanna, K., Brilot, A.F., Erb, M.L., Coker, J.K., Vavilina, A., Newton, G.L., Buschauer, R., Pogliano, K., Villa, E., Agard, D.A., Pogliano, J. (2017). Assembly of a nucleus-like structure during viral replication in bacteria. *Science 355*, 194-197.

Parent, K.N., Erb, M.L., Cardone,G., **Nguyen**, K., Gilcrease, E.B., Porcek, N.B., Pogliano, J., Baker, T.S., Casjens, S.R. (2014) OmpA and OmpC are critical host factors for bacteriophage Sf6 entry in *Shigella. Mol. Microbiol.,* 92, pp. 47–60

J.A. Kraemer, M.L. Erb, C.A. Waddling, E.A. Montabana, E.A. Zehr, H. Wang, **K. Nguyen**, D.S. Pham, D.A. Agard, J. Pogliano (2012) A phage tubulin assembles dynamic filaments by an atypical mechanism to center viral DNA within the host cell. *Cell*, 149 pp. 1488–1499

W.H. Pope, et al. (2011) Expanding the diversity of mycobacteriophages: insights into genome architecture and evolution. *PLoS One* 6:e16329e16329

ABSTRACT OF THE DISSERTATION

Jumbo phages assemble a nucleus-like structure in Pseudomonas

by

Katrina Tram Anh Nguyen

Doctor of Philosophy in Biology

University of California San Diego, 2019

Professor Joe Pogliano, Chair
Professor Elizabeth Villa, Co-Chair

Upon infection of host cells, jumbo *Pseudomonas* phages 201Φ2-1, ΦKZ, and ΦPA3 assemble a "phage nucleus" that encloses replicating viral DNA. The proteinaceous compartment segregates both phage and bacterial host proteins based on their function. Fluorescent microscopy indicates that proteins related to DNA transcription and translation, including phage homologs of RNA polymerase and DNA helicase as well as the bacterial DNA topoisomerase I, are localized inside the phage nucleus. The host ribosomes and other proteins related to translation are excluded from the nucleus along with phage-encoded metabolic enzymes. Each phage encodes a three-stranded tubulin, PhuZ, that forms a bipolar spindle array in the cell. PhuZ pushes the phage nucleus from

one cell pole to midcell then maintains the centered position. After capsids are assembled on the bacterial cell membrane, they traffic along PhuZ filaments to the phage nucleus and dock on the nuclear shell for DNA packaging. Following encapsidation of DNA, filled capsid particles migrate away from the nucleus to complete maturation in the cytoplasm. With genomes ranging from 280-316kb, proportionately large capsid sizes, and relatively small burst sizes, these phages have likely evolved this complicated system to reproduce more efficiently. In addition, the nuclear shell may protect viral DNA from host defenses. It is currently unknown how protein sorting occurs in this structure. However, one notable quirk of the ΦKZ infection system may eventually provide insight into the transport system. One variant of GFP, specifically GFPmut1, is transported into the ΦKZ phage nucleus. Furthermore, any protein fused to GFPmut1 on either the C or N terminus will also be transported into the phage nucleus. Although it is still unclear exactly why this happens, we have been able to utilize this for selective transport into the ΦKZ nucleus. GFPmut1 can be used as a tool for fluorescent labelling and targeting of proteins into the ΦKZ phage nucleus.

Chapter 1: Introduction

Phage

Our planet is swarming with ruthless killing machines – invaders that are invisible to the naked eye but can be found in every corner of the earth, from the depths of the ocean to the human gut. Bacteriophages, also known as phages, are viruses that infect bacteria or archaea by invading cells and hijacking their machinery to reproduce. Upon recognizing a bacterium, phages bind to it and inject their genetic material into the cell. From that point, infection can take two major routes. Lytic or virulent phages reproduce immediately upon entering a cell: manufacturing up to hundreds of progeny in a matter of minutes, then destroying their host to escape. Temperate or lysogenic phages infiltrate the host, hiding their DNA inside the cell then waiting until the time is right to enter the lytic cycle.

Phages were first described a century ago by Felix d'Herelle and Frederick Twort [1, 2]. Since then, these viruses have been recognized as colonizers of nearly every habitat. The global population of phages is estimated to be 10^{31} with 10^{24} productive viral infections occurring every second [3]. However, though phages are the most numerous and diverse entity on earth, still relatively little is known about them [4]. The genetic material of phages varies, in every combination of single-stranded or double-stranded, RNA or DNA. Genomes range in size, from the 3.5kb ssRNA phage MS2 to over 500kb, such as the dsDNA *Bacillus* phage G [5]. Phage genomes are usually encapsulated a proteinaceous capsid, though some phages use only a lipid envelope and some utilize both [6]. Capsids can also have a variety of tails attached to them, some of which use tail fibers that bind to the host cell or contractile machinery for genome injection. Based on

their morphology, phages can be categorized as filamentous, cubic, or pleomorphic but the majority of currently characterized phages are tailed [6] .

The ubiquity of phages in diverse environments means they play roles in innumerable processes, from universal food webs to intercellular interactions. Phages are responsible for lysing up to 40% of bacteria in the ocean each day [7]. Prophages, lysogens within a cell, can regulate the biology of their hosts. For example, cyanobacterial phages encode genes for photosynthesis, which can assist or repair their host's proteins, resulting in increased photosynthetic ability [8]. In this way and many others, phages are contributing to carbon turnover and oxygen production in the ocean, affecting the global climate. Lysogenic phage also confer virulence factors to some of the deadliest human pathogens, including *Escherichia*, *Salmonella*, *Staphylococcus*, *Streptococcus*, and *Vibrio* [9]. Phages facilitate horizontal gene transfer between infected bacteria, transferring large sections of DNA, even antibiotic resistance cassettes, between cells [10]. In addition, genetic differences between individuals are often due to the presence of phages. The small genetic dissimilarities between closely related bacteria can also be attributed to their prophages [11] This even extends to humans -- recent studies have indicated that the greatest genetic difference between identical twins is due to the different phages in their microbiome [12]. In addition to their genetic contributions, phages also affect bacterial evolution through the predator-prey relationship. Bacteria are constantly evolving to evade their parasitic infectors, and phage consistently evolve alongside them in an arms race [11]. The immense range of phages across our planet ensures that these viruses play a number of essential roles in nature.

Historically, phages have contributed greatly to many scientific fields. After their discovery, the earliest molecular biologists began to utilize phages as tools for discovery. The Hershey-Chase experiment used radiolabeled phages to establish the central dogma, confirming that DNA was the genetic material [13]. Phage ΦX174 was the first complete genome to be sequenced by Sanger in 1977 and communities of marine phages were the first samples to be shotgun sequenced [14, 15]. A number of phage proteins, such as RNA and DNA polymerases, ligases, and nucleases, as well as bacterial restriction endonucleases that naturally target phage genomes, are essential tools in molecular biology today. Phages themselves are utilized to transduce DNA between bacteria. Most recently, the discovery of CRISPR-cas, bacteria defense systems against phage, are now being utilized in the laboratory to give us the greatest genome editing capabilities to date. In addition, the current epidemic of antibiotic resistance in bacteria has again brought phages into the forefront of medicine. Though phages have been explored as antibacterial agents from their discovery, phage therapy has not been seriously considered in the United States until very recently. However, recent successes have been sparked interest in phage therapy once more [16].

ΦKZ family

The ΦKZ is a family of virulent phages with exceptionally large genomes [17]. These phages are highly divergent – from other phages as well as within the family [18]. The majority of ΦKZ phages infect *Pseudomonas* species, but some members of the family infect *Erwinia* or *Ralstonia* [19, 20]. Several family members have been investigated as tools for phage therapy against *Pseudomonas aeruginosa* [21, 22]. The

phage ΦPA3, with a genome of 309,208bp, can also be used as a generalized transducing phage [23]. As the phage for which the family was named, the 280,334bp *P. aeruginosa* phage ΦKZ is the most well-studied [24]. ΦKZ contains a proteinaceous inner body within each phage capsid, which is thought to be a spool for phage DNA [25, 26]. The inner body may be injected into the cell along with other phage proteins [27, 28]. ΦKZ also encodes two separate RNA polymerases, one associated with virion proteins, and a cellular polymerase with five subunits [29]. Rifampicin, which targets bacterial polymerase, has no effect on ΦKZ replication, indicating that the phage polymerase is unaffected by the antibiotic and that the phage does not use the bacterial polymerase for replication [29, 30]. The viral polymerase is likely conserved in the 316,647bp *Pseudomonas chlororaphis* phage 201Φ2-1, as similar polymerases were also identified in the ΦKZ virion through proteomic studies [18]. The ΦKZ phages are also notable for encoding a tubulin homolog, PhuZ, which was previously unheard of in phages [31].

The Prokaryotic Cytoskeleton

In fact, the cytoskeleton was long thought to be exclusive to eukaryotes. However, homologs to each of the major categories of cytoskeletal proteins: actin, tubulin, and intermediate filaments, have been discovered in bacteria and archaea, as well as an additional prokaryotic-specific group, Walker A Cytoskeletal ATPases. Much like their eukaryotic counterparts, cytoskeletal proteins in prokaryotes provide cell shape, structure, and organization.

Bacterial actins were first discovered through structure-based sequence alignment and are still generally identified by the presence of five conserved motifs in the nucleotide-

binding pocket [32]. Previously, phylogenetic analysis identified more than 40 families of actins, found on chromosomes, plasmids, and phage genomes [33]. One major family of actins, MreB, is responsible for cell shape in elongated bacteria and a number of other cell processes [34]. Most other actins are involved in segregation of DNA, including some encoded by bacteriophages. The *Bacillus thuringiensis* phage 305Φ8-36 encodes an actin-like protein previously designated as gp207 [35]. Based on conservation of the actin signature motif, the phage protein was sorted into the Alp6 family. AlpA-GFP fusions formed long filaments when expressed in *E. coli*, but the function is unknown [33]. AlpC is an actin-like protein encoded by CGP3, a *Corynebacterium glutamicum* prophage. AlpA, a DNA-binding protein on the same operon, binds a phage DNA consensus sequence, called alpS, composed of repeats upstream of the alpAC promoter. During phage induction, AlpC filaments bind to AlpA to push excised viral DNA to the cell membrane where further replication can occur [36].

Eukaryotes utilize tubulin for cell shape, transport within the cell, and cell division. Microtubules are stiff hollow tubes, comprised of 13 protofilaments of α and β tubulin heterodimers [37]. A key characteristic of tubulin is the ability to use dynamic instability, rapid cycles of growth and disassembly, for movement. Prokaryotic tubulins share this dynamic quality as well as many of the same functions. In general, prokaryotic tubulins are comprised of fewer (1-5) protofilament strands [38-42]. Like bacterial actins, prokaryotic tubulins are used for DNA segregation. The TubZ family, found in *Bacillus* species, forms dynamic polarized filaments that transition between two-stranded and four-stranded [38]. TubZ treadmills, growing at the plus end while shrinking or

depolymerizing at the minus end, to push plasmids apart for efficient segregation during cell division [43]. The most well-characterized prokaryotic actin is FtsZ, which polymerizes into a single-stranded filament responsible for assembling a cytokinetic ring that contracts to divide bacterial and archaeal cells [44]. FtsZ is highly conserved in most bacterial families. The wide distribution of FtsZ and its high level of similarity to eukaryotic actin at the structural level suggest that actin is an ancient protein that existed in the lineage of our last common ancestor [45, 46]. Archaea have been found to encode additional diverse tubulins: three families of FtsZ; a group of eukaryotic tubulins; and a third group of archaea-specific tubulins, CetZ [47].

Though few viruses are known to encode their own cytoskeletal elements, some utilize the cytoskeletal proteins of their hosts for their own replication. Various eukaryotic viruses have been found to hijack the mammalian cytoskeleton for both intracellular and extracellular transport. Vaccinia viruses utilize both actin and tubulin from the host cell. Intracellularly, microtubules have been shown to transport viruses, first as unenveloped virions then as mature viruses, throughout the cell [48, 49]. In order to exit the cell, mature viruses trigger polymerization of the bacterial actin network beneath virions positioned at the cell membrane. The resulting actin tails launch single viruses out of a cell for intercellular spread [50-52]. Herpesviruses are also transported bidirectionally along microtubules to reach the nucleus and for egress out of the cell [53-55]. Interestingly, herpesviruses are thought to be descended from bacteriophages [56]. Recent evidence has shown that bacteriophages also manipulate the cytoskeletons of their host cells. MreB, in particular, has been found to play a role in organization of bacteriophage DNA

in infected cells. The *Bacillus subtilis* Φ29 phage encodes one protein that interacts directly with MreB to attach viral DNA to the cell membrane and other that associates with the FtsZ ring to promote replication [57, 58].

Within the past few years, several phage-encoded tubulins have been discovered and characterized. A tubulin homolog encoded by the lysogenic phage, c-st, was found to partition prophage plasmids in *Clostridium botulinum* during division [59, 60]. An actin-like protein encoded by *Corynebacterium glutamicum* prophage CGP3 polymerizes to organize viral DNA molecules during replication [36]. A tubulin homolog was also found to be conserved in the genomes of the ΦKZ phage family [31].

PhuZ

PhuZ, for phage-encoded TubZ, was first discovered in 201Φ2-1, a phage with a genome of 316kb that infects *Pseudomonas chlororaphis* [18]. While PhuZ shares little similarity with either eukaryotic tubulin or FtsZ at the amino acid level, certain key domains, including the tubulin fold, are conserved. However, PhuZ has a unique C-terminal extension that is essential for polymerization of filaments [31]. PhuZ was found to polymerize and show dynamic instability both in vitro and in vivo. A GFP fusion to PhuZ produced fluorescent bipolar spindle in phage-infected cells, with one filament extending from each cell pole to the cell center. Between the polymers, a mass of DNA was observed at midcell [31]. Fluorescence in situ hybridization (FISH) indicated that the infection nucleoid was comprised solely of viral DNA, as bacterial chromosomal DNA was degraded in the early stages of infection [61]. When point mutations were made in the catalytic T7 loop of PhuZ, the polymers were unable to hydrolyze GTP and became static.

Expression of these mutant filaments resulted in mispositioned infection nucleoids, where the DNA was present at the cell pole rather than the cell center. In addition, burst size was reduced approximately 50% by the mutant PhuZ [31]. Like eukaryotic microtubules, PhuZ is dynamically unstable, meaning that the filaments stochastically switch between cycles of growth and depolymerization. This constant movement is responsible for pushing the infection nucleoid to the center of an infected cell. The filaments are anchored at the poles of the bacterial cell and demonstrate polarity as well, growing from one end of the filament while depolymerizing at the other end [61].

Many of the phages in the same family, including *Pseudomonas aeruginosa* phages ΦKZ, and ΦPA3, also encode the PhuZ protein [62]. The 201Φ2-1 PhuZ microtubule is composed of three twisted strands, which is a unique conformation [39, 41]. The crystal structure of PhuZ from the ΦKZ phage was found to be highly analogous to that of 201Φ2-1 PhuZ [59]. The conservation of certain critical interactions as well as averaging of filament segments suggest that ΦPA3 PhuZ also forms the same twisted three-stranded polymer [41]. The distinctive triple-stranded structure of PhuZ suggests that it may be an evolutionary intermediate between simple bacterial filaments and the more complicated eukaryotic tubulin.

The Phage Nucleus

In fact, many facets of the ΦKZ family infection system show characteristics of an intermediary step between eukaryotes and bacteria. These large bacteriophages were found to reorganize a bacterium upon infection – into something resembling the most singular hallmark of eukaryotes: the nucleus. This “phage nucleus” might represent the

most primitive example of separation between cell processes. DNA and RNA, plus proteins related to DNA replication and transcription, are confined inside a compartment while protein translation occurs in the cytoplasm. The major components of the phage nucleus were found to be conserved in two related phages, ΦKZ and ΦPA3, which infect *Pseudomonas aeruginosa* [62]. An investigation of PhuZ in conjunction with the major capsid proteins of 201Φ2-1 and ΦPA3 found that capsids move along PhuZ filaments toward the phage nucleus for DNA packaging. While dynamic instability is utilized to center the phage nucleus in the early stages of infection, the tubulin later switches to a treadmilling mechanism. PhuZ subunits are constantly added to one end of the filament while the other end depolymerizes at a slower rate, resulting in constant movement in one direction. Treadmilling also allows the PhuZ spindle to rotate the phage nucleus so that capsids can be more easily and evenly distributed around its surface. Though many facets of the phage nucleus are conserved, differences do exist between the three phages. Components of the shell that form the phage nucleus compartment differ, in both sequence and phenotype. In addition, the ΦKZ nuclear transport system has one striking but peculiar distinction. The fluorescent protein GFPmut1, alone or fused to another protein, is transported into the ΦKZ phage nucleus. Although the mechanism of transport is still unclear, we have been able to utilize this to manipulate selective transport into the ΦKZ nucleus. GFPmut1 can be used for fluorescent labelling, targeting of proteins into the ΦKZ phage nucleus and study of the phage nucleus transport system.

References

1. d'Herelle F. 1917. Sur un microbe invisible antagoniste des bacilles dysentériques. CR Acad Sci Paris.

2. Twort FW. 1915. An Investigation On The Nature Of Ultra-Microscopic Viruses. The Lancet 186:1241-1243.

3. Hendrix R. 2010. Recoding in bacteriophages. , p 249-258. *In* Atkins JG, RF (ed), *Recoding: Expansion of Decoding Rules Enriches Gene Expression*. Springer.

4. Hatfull GF. 2015. Dark Matter of the Biosphere: the Amazing World of Bacteriophage Diversity. J Virol 89:8107-10.

5. Salmond GP, Fineran PC. 2015. A century of the phage: past, present and future, p 777-86, Nat Rev Microbiol, vol 13, England.

6. Ackermann HW, Prangishvili D. 2012. Prokaryote viruses studied by electron microscopy. Arch Virol 157:1843-9.

7. Danovaro R, Corinaldesi C, Dell'anno A, Fuhrman JA, Middelburg JJ, Noble RT, Suttle CA. 2011. Marine viruses and global climate change. FEMS Microbiol Rev 35:993-1034.

8. Sharon I, Battchikova N, Aro EM, Giglione C, Meinnel T, Glaser F, Pinter RY, Breitbart M, Rohwer F, Beja O. 2011. Comparative metagenomics of microbial traits within oceanic viral communities. Isme j 5:1178-90.

9. Keen EC. 2015. A century of phage research: Bacteriophages and the shaping of modern biology. Bioessays 37:6-9.

10. Hendrix RW, Lawrence JG, Hatfull GF, Casjens S. 2000. The origins and ongoing evolution of viruses. Trends Microbiol 8:504-8.

11. Rohwer F, Segall AM. 2015. A Century of Phage Lessons. Nature 528:46-8.

12. Reyes A, Haynes M, Hanson N, Angly FE, Heath AC, Rohwer F, Gordon JI. 2010. Viruses in the faecal microbiota of monozygotic twins and their mothers. Nature 466:334-8.

13. Hershey AD, Chase M. 1952. Independent functions of viral protein and nucleic acid in growth of bacteriophage. J Gen Physiol 36:39-56.

14. Sanger F, Coulson AR, Friedmann T, Air GM, Barrell BG, Brown NL, Fiddes JC, Hutchison CA, 3rd, Slocombe PM, Smith M. 1978. The nucleotide sequence of bacteriophage phiX174. J Mol Biol 125:225-46.

15. Breitbart M, Salamon P, Andresen B, Mahaffy JM, Segall AM, Mead D, Azam F, Rohwer F. 2002. Genomic analysis of uncultured marine viral communities. Proc Natl Acad Sci U S A 99:14250-5.

16. Health U. 2019. Phage 101 - Bacteriophage Therapy - UC San Diego Health, *on* UCSDHealth. https://health.ucsd.edu/news/topics/phage-therapy/Pages/Phage-101.aspx.

17. Krylov VN, Dela Cruz DM, Hertveldt K, Ackermann HW. 2007. "phiKZ-like viruses", a proposed new genus of myovirus bacteriophages. Arch Virol 152:1955-9.

18. Thomas JA, Rolando MR, Carroll CA, Shen PS, Belnap DM, Weintraub ST, Serwer P, Hardies SC. 2008. Characterization of Pseudomonas chlororaphis myovirus 201varphi2-1 via genomic sequencing, mass spectrometry, and electron microscopy. Virology 376:330-8.

19. Arens DK, Brady TS, Carter JL, Pape JA, Robinson DM, Russell KA, Staley LA, Stettler JM, Tateoka OB, Townsend MH, Whitley KV, Wienclaw TM, Williamson TL, Johnson SM, Grose JH. 2018. Characterization of two related Erwinia myoviruses that are distant relatives of the PhiKZ-like Jumbo phages. PLoS One 13:e0200202.

20. Bhunchoth A, Blanc-Mathieu R, Mihara T, Nishimura Y, Askora A, Phironrit N, Leksomboon C, Chatchawankanphanich O, Kawasaki T, Nakano M, Fujie M, Ogata H, Yamada T. 2016. Two asian jumbo phages, varphiRSL2 and varphiRSF1, infect Ralstonia solanacearum and show common features of varphiKZ-related phages. Virology 494:56-66.

21. Latz S, Kruttgen A, Hafner H, Buhl EM, Ritter K, Horz HP. 2017. Differential Effect of Newly Isolated Phages Belonging to PB1-Like, phiKZ-Like and LUZ24-Like Viruses against Multi-Drug Resistant Pseudomonas aeruginosa under Varying Growth Conditions. Viruses 9.

22. Danis-Wlodarczyk K, Vandenheuvel D, Jang HB, Briers Y, Olszak T, Arabski M, Wasik S, Drabik M, Higgins G, Tyrrell J, Harvey BJ, Noben JP, Lavigne R, Drulis-Kawa Z. 2016. A proposed integrated approach for the preclinical evaluation of phage therapy in Pseudomonas infections. Sci Rep 6:28115.

23. Monson R, Foulds I, Foweraker J, Welch M, Salmond GP. 2011. The Pseudomonas aeruginosa generalized transducing phage phiPA3 is a new member of the phiKZ-like group of 'jumbo' phages, and infects model laboratory strains and clinical isolates from cystic fibrosis patients. Microbiology 157:859-67.

24. Krylov VN, Smirnova TA, Minenkova IB, Plotnikova TG, Zhazikov IZ, Khrenova EA. 1984. Pseudomonas bacteriophage phi KZ contains an inner body in its capsid. Can J Microbiol 30:758-62.

25. Wu W, Thomas JA, Cheng N, Black LW, Steven AC. 2012. Bubblegrams reveal the inner body of bacteriophage ϕKZ. Science 335:182.

26. Thomas JA, Weintraub ST, Wu W, Winkler DC, Cheng N, Steven AC, Black LW. 2012. Extensive proteolysis of head and inner body proteins by a morphogenetic protease in the giant Pseudomonas aeruginosa phage phiKZ. Mol Microbiol 84:324-39.

27. Wu W, Thomas JA, Cheng N, Black LW, Steven AC. 2012. Bubblegrams reveal the inner body of bacteriophage phiKZ. Science 335:182.

28. Yakunina M, Artamonova T, Borukhov S, Makarova KS, Severinov K, Minakhin L. 2015. A non-canonical multisubunit RNA polymerase encoded by a giant bacteriophage. Nucleic Acids Res 43:10411-20.

29. Matsui T, Yoshikawa G, Mihara T, Chatchawankanphanich O, Kawasaki T, Nakano M, Fujie M, Ogata H, Yamada T. 2017. Replications of Two Closely Related Groups of Jumbo Phages Show Different Level of Dependence on Host-encoded RNA Polymerase. Front Microbiol 8:1010.

30. Kraemer JA, Erb ML, Waddling CA, Montabana EA, Zehr EA, Wang H, Nguyen K, Pham DS, Agard DA, Pogliano J. 2012. A phage tubulin assembles dynamic filaments by an atypical mechanism to center viral DNA within the host cell. Cell 149:1488-99.

31. Bork P, Sander C, Valencia A. 1992. An ATPase domain common to prokaryotic cell cycle proteins, sugar kinases, actin, and hsp70 heat shock proteins. Proc Natl Acad Sci U S A 89:7290-4.

32. Derman AI, Becker EC, Truong BD, Fujioka A, Tucey TM, Erb ML, Patterson PC, Pogliano J. 2009. Phylogenetic analysis identifies many uncharacterized actin-like proteins (Alps) in bacteria: regulated polymerization, dynamic instability and treadmilling in Alp7A. Mol Microbiol 73:534-52.

33. Jones LJ, Carballido-Lopez R, Errington J. 2001. Control of cell shape in bacteria: helical, actin-like filaments in Bacillus subtilis. Cell 104:913-22.

34. Thomas JA, Hardies SC, Rolando M, Hayes SJ, Lieman K, Carroll CA, Weintraub ST, Serwer P. 2007. Complete genomic sequence and mass spectrometric analysis of highly diverse, atypical Bacillus thuringiensis phage 0305phi8-36. Virology 368:405-21.

35. Donovan C, Heyer A, Pfeifer E, Polen T, Wittmann A, Kramer R, Frunzke J, Bramkamp M. 2015. A prophage-encoded actin-like protein required for efficient viral DNA replication in bacteria. Nucleic Acids Res 43:5002-16.

36. Sui H, Downing KH. 2010. Structural basis of interprotofilament interaction and lateral deformation of microtubules. Structure 18:1022-31.

37. Montabana EA, Agard DA. 2014. Bacterial tubulin TubZ-Bt transitions between a two-stranded intermediate and a four-stranded filament upon GTP hydrolysis. Proc Natl Acad Sci U S A 111:3407-12.

38. Erickson HP, Taylor DW, Taylor KA, Bramhill D. 1996. Bacterial cell division protein FtsZ assembles into protofilament sheets and minirings, structural homologs of tubulin polymers. Proc Natl Acad Sci U S A 93:519-23.

39. Deng X, Fink G, Bharat TAM, He S, Kureisaite-Ciziene D, Lowe J. 2017. Four-stranded mini microtubules formed by Prosthecobacter BtubAB show dynamic instability. Proc Natl Acad Sci U S A 114:E5950-e5958.

40. Zehr EA, Kraemer JA, Erb ML, Coker JK, Montabana EA, Pogliano J, Agard DA. 2014. The structure and assembly mechanism of a novel three-stranded tubulin filament that centers phage DNA. Structure 22:539-48.

41. Pilhofer M, Ladinsky MS, McDowall AW, Petroni G, Jensen GJ. 2011. Microtubules in bacteria: Ancient tubulins build a five-protofilament homolog of the eukaryotic cytoskeleton. PLoS Biol 9:e1001213.

42. Larsen RA, Cusumano C, Fujioka A, Lim-Fong G, Patterson P, Pogliano J. 2007. Treadmilling of a prokaryotic tubulin-like protein, TubZ, required for plasmid stability in Bacillus thuringiensis. Genes Dev 21:1340-52.

43. Margolin W. 2005. FtsZ and the division of prokaryotic cells and organelles. Nat Rev Mol Cell Biol 6:862-71.

44. Wickstead B, Gull K. 2011. The evolution of the cytoskeleton. J Cell Biol 194:513-25.

45. van den Ent F, Amos LA, Löwe J. 2001. Prokaryotic origin of the actin cytoskeleton. Nature 413:39-44.

46. Aylett CHS, Duggin IG. 2017. The Tubulin Superfamily in Archaea, p 393-417. *In* Löwe J, Amos LA (ed), Prokaryotic Cytoskeletons: Filamentous Protein Polymers Active in the Cytoplasm of Bacterial and Archaeal Cells. Springer International Publishing, Cham.

47. Carter GC, Rodger G, Murphy BJ, Law M, Krauss O, Hollinshead M, Smith GL. 2003. Vaccinia virus cores are transported on microtubules. J Gen Virol 84:2443-58.

48. Ward BM, Moss B. 2001. Vaccinia virus intracellular movement is associated with microtubules and independent of actin tails. J Virol 75:11651-63.

49. Way M. 1998. Interaction of vaccinia virus with the actin cytoskeleton. Folia Microbiol (Praha) 43:305-10.

50. Rottner K, Stradal TE. 2009. Poxviruses taking a ride on actin: new users of known hardware. Cell Host Microbe 6:497-9.

51. Schmidt FI, Mercer J. 2012. Vaccinia virus egress: actin OUT with clathrin. Cell Host Microbe 12:263-5.

52. Smith GA, Gross SP, Enquist LW. 2001. Herpesviruses use bidirectional fast-axonal transport to spread in sensory neurons. Proc Natl Acad Sci U S A 98:3466-70.

53. Ward BM. 2011. The taking of the cytoskeleton one two three: how viruses utilize the cytoskeleton during egress. Virology 411:244-50.

54. Lyman MG, Enquist LW. 2009. Herpesvirus interactions with the host cytoskeleton. J Virol 83:2058-66.

55. Selvarajan Sigamani S, Zhao H, Kamau YN, Baines JD, Tang L. 2013. The structure of the herpes simplex virus DNA-packaging terminase pUL15 nuclease domain suggests an evolutionary lineage among eukaryotic and prokaryotic viruses. J Virol 87:7140-8.

56. Ballesteros-Plaza D, Holguera I, Scheffers DJ, Salas M, Munoz-Espin D. 2013. Phage 29 phi protein p1 promotes replication by associating with the FtsZ ring of the divisome in Bacillus subtilis. Proc Natl Acad Sci U S A 110:12313-8.

57. Munoz-Espin D, Daniel R, Kawai Y, Carballido-Lopez R, Castilla-Llorente V, Errington J, Meijer WJ, Salas M. 2009. The actin-like MreB cytoskeleton organizes viral DNA replication in bacteria. Proc Natl Acad Sci U S A 106:13347-52.

58. Oliva MA, Martin-Galiano AJ, Sakaguchi Y, Andreu JM. 2012. Tubulin homolog TubZ in a phage-encoded partition system. Proc Natl Acad Sci U S A 109:7711-6.

59. Sakaguchi Y, Hayashi T, Kurokawa K, Nakayama K, Oshima K, Fujinaga Y, Ohnishi M, Ohtsubo E, Hattori M, Oguma K. 2005. The genome sequence of

Clostridium botulinum type C neurotoxin-converting phage and the molecular mechanisms of unstable lysogeny. Proc Natl Acad Sci U S A 102:17472-7.

60. Erb ML, Kraemer JA, Coker JK, Chaikeeratisak V, Nonejuie P, Agard DA, Pogliano J. 2014. A bacteriophage tubulin harnesses dynamic instability to center DNA in infected cells. Elife 3.

61. Chaikeeratisak V, Nguyen K, Egan ME, Erb ML, Vavilina A, Pogliano J. 2017. The Phage Nucleus and Tubulin Spindle Are Conserved among Large Pseudomonas Phages. Cell Rep 20:1563-1571.

REPORT

CELL BIOLOGY

Assembly of a nucleus-like structure during viral replication in bacteria

Vorrapon Chaikeeratisak,[1] Katrina Nguyen,[1] Kanika Khanna,[1] Axel F. Brilot,[2] Marcella L. Erb,[1] Joanna K. C. Coker,[1] Anastasia Vavilina,[1] Gerald L. Newton,[1] Robert Buschauer,[3] Kit Pogliano,[1] Elizabeth Villa,[3] David A. Agard,[2] Joe Pogliano[1]*

We observed the assembly of a nucleus-like structure in bacteria during viral infection. Using fluorescence microscopy and cryo-electron tomography, we showed that *Pseudomonas chlororaphis* phage 201ϕ2-1 assembled a compartment that separated viral DNA from the cytoplasm. The phage compartment was centered by a bipolar tubulin-based spindle, and it segregated phage and bacterial proteins according to function. Proteins involved in DNA replication and transcription localized inside the compartment, whereas proteins involved in translation and nucleotide synthesis localized outside. Later during infection, viral capsids assembled on the cytoplasmic membrane and moved to the surface of the compartment for DNA packaging. Ultimately, viral particles were released from the compartment and the cell lysed. These results demonstrate that phages have evolved a specialized structure to compartmentalize viral replication.

Viruses have been coevolving with cellular life for more than 2 billion years (*1*). We recently described a bacteriophage reproduction pathway in *Pseudomonas* species in which a phage-encoded tubulin-like cytoskeletal protein (PhuZ) forms a bipolar spindle that positions replicating phage DNA at the cell midpoint (*2*–*6*). To search for other proteins required for this pathway, we used mass spectrometry to identify phage 201ϕ2-1 proteins expressed during lytic growth (*7*–*9*) and then created fusions of these proteins to green fluorescent protein (GFP) for localization profiling (table S1). We next examined the localization pattern of each protein in cells before and during phage infection. gp105 is the first and most highly expressed phage protein after infection (Fig. 1F). In uninfected cells, GFP-gp105 was uniformly distributed, but surprisingly, it formed a somewhat spherically shaped structure surrounding phage DNA at the midcell after 45 min of infection (Fig. 1A). This structure was observed in every infected cell, with 87% of cells containing a single structure and the remaining cells containing either two (10%) or three structures (3%) (fig. S1). In photobleaching experiments, fluorescence from GFP-gp105 did not recover after 16 min, which indicates that GFP-gp105 formed a relatively stable structure around the phage DNA (Fig. 1B).

[1]Division of Biological Sciences, University of California San Diego, La Jolla, CA 92093, USA. [2]Howard Hughes Medical Institute (HHMI) and the Department of Biochemistry and Biophysics, University of California San Francisco, San Francisco, CA 94158, USA. [3]Department of Chemistry and Biochemistry, University of California San Diego, La Jolla, CA 92093, USA.
***Corresponding author. Email: jpogliano@ucsd.edu**

To understand the timing of the formation of this structure, we performed time-lapse microscopy in which we expressed GFP-gp105 in *P. chlororaphis* and then followed its assembly during phage infection. We also expressed mCherry-PhuZ to simultaneously monitor spindle assembly. Upon addition of phage to the cells, GFP-gp105 formed a small focus near the cell pole and mCherry-PhuZ assembled filaments at both cell poles, setting up the bipolar spindle (Fig. 1C). Over time, PhuZ polymers pushed the GFP-gp105 shell to the cell center (Fig. 1C), confirming that these dynamically unstable filaments center phage DNA by a pushing mechanism. The small GFP-gp105 shell increased in size while being pushed to the midcell [Fig. 1C, 33 to 41 min postinfection (mpi), and movie S1], where it continued to grow (Fig. 1C, 43 to 65 mpi, and movie S1) as DNA replication progressed (*5*). Centrally positioned GFP-gp105 shells continued to be pushed back and forth by opposing filaments of the bipolar PhuZ spindle, causing them to oscillate near the cell center (fig. S2 and movie S2). When opposing PhuZ filaments pushed transversely on opposite sides of the GFP-gp105 shell, the entire structure rotated in position (Fig. 1C, right, and movie S3). In the presence of a mutant PhuZ protein ($PhuZ^{D190A}$) that is unable to hydrolyze GTP (guanosine triphosphate) and forms static filaments, the GFP-gp105 shell remained at the cell pole and exhibited little motion, suggesting that both movement and rotation of the shell were caused by forces exerted by the PhuZ spindle (Fig. 1, D and E).

Localization profiling of GFP fusions to 52 phage proteins revealed a high level of organization inside the infected cell in which many proteins were localized inside the gp105 shell along with the phage DNA whereas other proteins were excluded (figs. S3 to S5). Proteins suspected to be involved in DNA replication (Fig. 2A) or transcription (Fig. 2B) colocalized with the DNA inside the shell (fig. S3). This included phage encoded homologs of DNA helicase (gp197), DNA ligase (gp333), RNase H (gp240), RecA (gp237), and two homologs of the β′ subunits of RNA polymerase (gp107 and gp130) (Fig. 2, A and B). In addition, host DNA topoisomerase I was found inside the gp105 shell, indicating that localization to the shell was not limited to phage proteins (Fig. 2A). Three phage proteins of unknown function—gp124, gp125, and gp126—also localized inside the shell, and we thus speculate that they might be involved in DNA processes such as replication, transcription, or recombination (fig. S4). In contrast, GFP fusions to host proteins involved in translation, including the 50*S* ribosomal proteins L20 and L28, the translation initiation factor 1 (IF1), and the peptide chain release factor 3 (RF3), were located in the cytoplasm outside of the shell (Fig. 2C). Phage homologs of the metabolic enzymes thymidylate kinase (gp287), which catalyzes phosphorylation of thymidine monophosphate to thymidine diphosphate, and thymidylate synthase (gp350), which catalyzes the conversion of deoxyuridine monophosphate to deoxythymidine monophosphate, were also excluded from the shell (Fig. 2D), as was GFP alone (fig. S5). This subcellular compartmentalization of enzymes and DNA resembles the organization of eukaryotic cells containing a nucleus.

To gain insight into the mechanism by which proteins might enter the structure, we performed time-lapse microscopy on cells that expressed a GFP-tagged copy of the phage-encoded RecA homolog gp237. Before infection, gp237-GFP was located in the cytoplasm, but after addition of phage, it gradually accumulated inside the growing phage compartment and nearly undetectable levels remained in the cytoplasm after 30 min (Fig. 2, G and H, and movie S4). Thus, proteins can translocate to the phage compartment post-translationally. Once inside, gp237-GFP formed foci (Fig. 2E) that rotated together with the mCherry-gp105 shell, completing one rotation in ~30 s, suggesting that the entire structure rotates as a singular unit (Fig. 2F, movie S5, and fig. S6).

Localization profiling of phage structural proteins allowed us to study phage particle maturation and assembly. GFP fusions to the predicted major capsid protein gp200 and the internal head protein gp246 demonstrated an orchestrated assembly process. Approximately 40 mpi, empty capsids assembled near the cell membrane (Fig. 3C, 43 mpi), forming bright green foci. Capsids (green) then migrated from the membrane to the surface of the phage compartment (red) (Fig. 3C, 46 mpi, and movie S6) and accumulated on the outside of the mCherry-gp105 shell (Fig. 3, C to E). In time-lapse microscopy over shorter time scales, the capsids and the phage compartment rotated together as

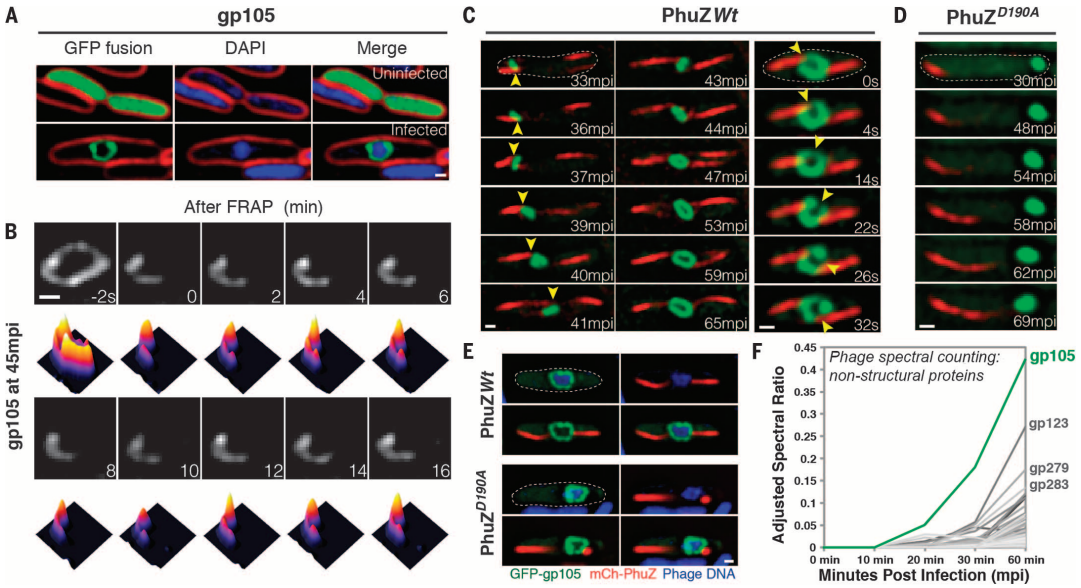

Fig. 1. gp105, an early and highly expressed phage protein, forms a shell around viral DNA during phage infection. (**A**) N-terminal fusion of gp105 to GFP (GFP-gp105; green) is diffuse in uninfected *P. chlororaphis* cells (top) and assembles a shell that encloses the phage DNA at 45 min postinfection (mpi) with phage 201ϕ2-1 (bottom). Cell membranes were stained with FM 4-64 (red), and DNA was stained with DAPI (blue). (**B**) Fluorescence recovery after photobleaching (FRAP) of the GFP-gp105 shell at 45 mpi. The bleached area of the shell generated at time 0 min does not recover over the course of 16 min. Heat maps show GFP intensity corresponding to the images above. (**C** and **D**) Time-lapse imaging (measured in minutes postinfection or seconds) of GFP-gp105 in the presence of mCherry-tagged (red) (C) wild-type PhuZ and (D) mutant PhuZ^{D190A}. (C) As indicated by arrowheads, the shell moves to the midcell and rotates (in this case, clockwise) during phage infection in the presence of wild-type PhuZ. See also movies S1 and S3. (D) In the presence of PhuZ^{D190A}, the shell remains at the cell pole throughout the experiment and does not rotate. A lack of rotation is sometimes observed in the presence of wild-type PhuZ for larger gp105 shells such as that shown in (B). Dashed circles indicate the border of the cells. (**E**) Static images of infected host cells expressing GFP-gp105 together with either wild-type mCherry-PhuZ or mutant mCherry-PhuZ^{D190A} at 60 mpi. Phage DNA was stained blue with DAPI. (A to E) Scale bars, 0.5 μm. (**F**) Protein mass spectrometry analysis of phage-infected cells showing putative nonstructural phage proteins until 60 mpi. The gp105 protein (green line) is the most highly expressed phage protein. (See table S1.)

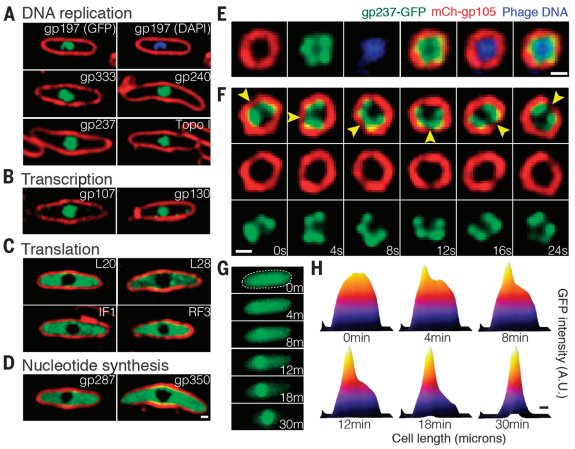

Fig. 2. DNA replication and transcription occur inside the phage compartment, whereas translation occurs outside. (**A** to **D**) Localization profiling of GFP-tagged phage and host proteins involved in various functions at 60 mpi. All proteins were fused to GFP (green), DNA was stained with DAPI (blue), and membranes were stained with FM 4-64 (red). (A) Proteins predicted to be involved in DNA replication, including the phage proteins gp237 (RecA homolog), gp197 (helicase homolog), gp333 (ligase homolog), gp240 (RNase H homolog), and host DNA topoisomerase I. (B) Two phage-encoded proteins predicted to be involved in transcription, gp107 and gp130 (RNA polymerase β′ subunit homologs). (C) Host proteins involved in translation, including ribosomal proteins L20 and L28, translation initiation factor 1 (IF1), and peptide chain release factor 3 (RF3). (D) Phage proteins predicted to be involved in nucleotide synthesis. including gp287 (thymidylate kinase homolog) and gp350 (thymidylate synthase homolog). (**E**), mCherry-gp105 (red), the RecA homolog gp237-GFP (green), and DAPI-stained DNA (blue), demonstrating localization of gp237 and DNA inside the gp105 shell. (**F**) Time-lapse imaging (in seconds) showing rotation of the compartment and its contents. As indicated by arrowheads, the shell and gp237 rotate together (in this cell, in a counterclockwise direction), suggesting that the entire structure and its contents rotate. See also movie S5. (**G**) gp237 moves from the host cell cytoplasm to the compartment during phage infection in this 30-min time lapse (m, minutes). The dashed circle indicates the border of the cell. (**H**) Heat map of GFP intensity of gp237 in the host cell as corresponding to the fluorescent micrographs reveals that gp237 moves into and accumulates in the gp105 shell. (See also movie S4.) Scale bars in (D) to (F) and (H), 0.5 μm. A.U., arbitrary units.

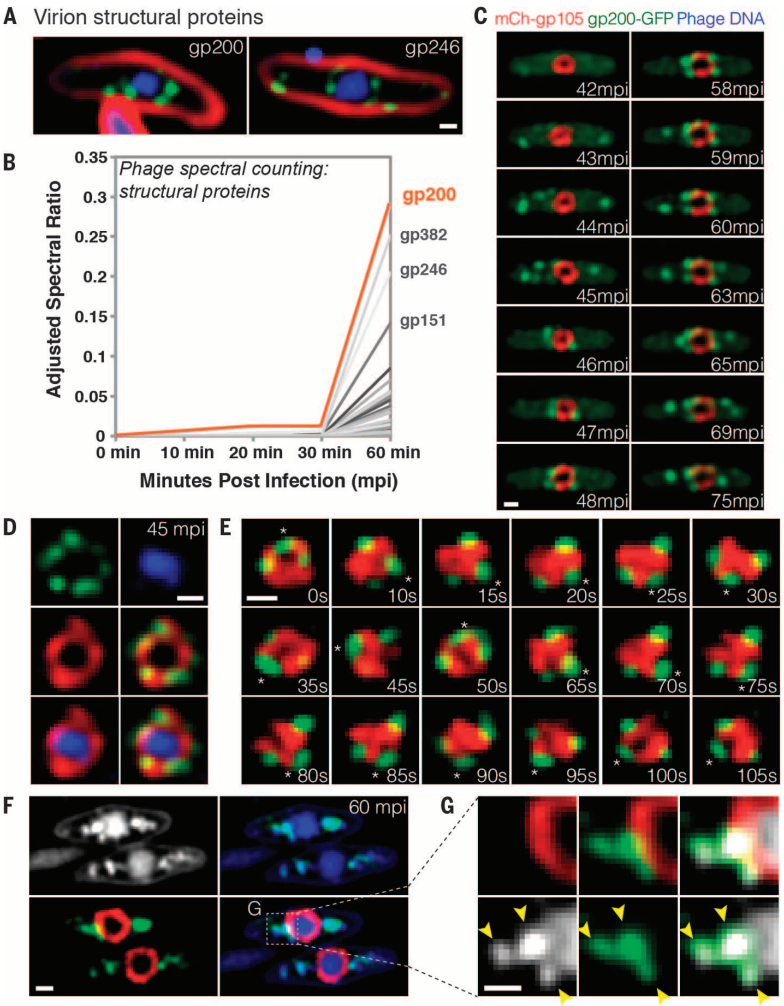

Fig. 3. Capsids migrate to the surface of the phage compartment for DNA encapsidation. (**A**) Localization of the predicted phage structural proteins gp200 (major capsid protein) and gp246 (internal head protein). The proteins were fused to GFP (green), membranes were stained with FM 4-64 (red), and DNA was stained with DAPI (blue) at 60 mpi. (**B**) Mass spectrometry results showing spectral counting of predicted phage structural proteins in infected host cells until 60 mpi; gp200 (orange line) is the most abundant structural protein. (**C**) Time-lapse microscopy of mCherry-gp105 (red) and the predicted capsid protein gp200-GFP (green), showing that gp200-GFP was initially diffuse (at 42 mpi) and assembled foci on the cell periphery (at 43 to 45 mpi) that move to the gp105 shell (at 45 to 46 mpi), remain attached for 12 min, and then are released from the shell (at 59 to 75 mpi). Foci translocate to the gp105 shell within 1 to 2 min. See also movie S6. (**D**) Static images showing gp200-GFP (green) on the surface of the mCherry-gp105 shell (red), with DNA (blue) inside, at 45 mpi. (**E**) Time lapse showing that gp200-GFP foci rotate together with mCherry-gp105 throughout this 105-s experiment. The position of a single capsid (asterisk) was tracked for the duration of the time lapse. See movie S7. (**F** and **G**) Static images of infected cells at 60 mpi to show colocalization of gp200-GFP (green) and phage DNA (blue or white) outside the mCherry-gp105 shell (red). The region indicated by the dashed box in (F) is magnified in (G) to more clearly show the colocalization of DNA (white) within the gp200 foci (green). Arrowheads indicate the colocalization. Scale bars in (A) and (C) to (G), 0.5 μm.

a single unit (Fig. 3E), undergoing eight successive revolutions in the example shown in movie S7, suggesting that the capsids were tightly docked to the surface. Later, capsids appeared to detach from the phage compartment and migrate away from it (Fig. 3C, 59 to 75 mpi). After 60 min, capsids were costained with 4′,6-diamidino-2-phenylindole (DAPI) (Fig. 3, F and G), showing that DNA packaging occurred while docked at the surface of the phage compartment.

We used cryo-electron tomography (CET) of cryo-focused ion beam (FIB)–milled phage-infected cells to visualize the phage compartment and various steps in phage assembly at high resolution and in a near-native state (*10*–*12*). In samples collected at 60 mpi, we observed a central compartment containing a sharply defined but irregularly shaped border (Fig. 4, A and B, and movie S8). The compartment border had an appearance distinct from the cytoplasmic membrane, supporting its composition as a proteinaceous shell with gp105 as a key component. Three-dimensional reconstructions showed a largely continuous envelope with a thickness of ~5 nm forming an apparently enclosed structure. Our fluorescence data indicate that this structure excludes soluble GFP, suggesting that it forms a barrier to protein diffusion (fig. S5). Ribosomes were clearly visible in the cytoplasm but were excluded from the compartment, in agreement with our fluorescence microscopy studies (Fig. 4, A and B). Partially constructed capsids were observed at the bacterial inner membrane (Fig. 4C) where assembly occurs. Capsids containing various amounts of DNA were docked on the surface of the intracellular phage compartment (Fig. 4, B, E, and F) and often a connecting collar was visualized (Fig. 4F, arrow), as well as capsids that appeared to be empty, indicating that this is the site of DNA packaging. Filled capsids and fully assembled phage particles (Fig. 4, B and G) containing tails were observed in the cytoplasm away from the phage compartment. Overall, the CET data were fully consistent with our fluorescence microscopy results and demonstrate that the phage compartment is surrounded by a shell that appears to be contiguous.

Here we describe a nucleus-like structure formed by a virus during infection of bacteria and its role in the phage life cycle (fig. S11). The compartment initially assembles near the cell pole surrounding phage DNA after injection, potentially forming a protective enclosure that shields it from host defense systems. The compartment grows in size as DNA replication proceeds and is centrally positioned by the PhuZ spindle. Previously we showed that phage DNA is centered by PhuZ polymers, but it was unclear how PhuZ filaments might connect to the replicating DNA molecules (*4*–*6*). Our results suggest that the nucleus-like compartment described

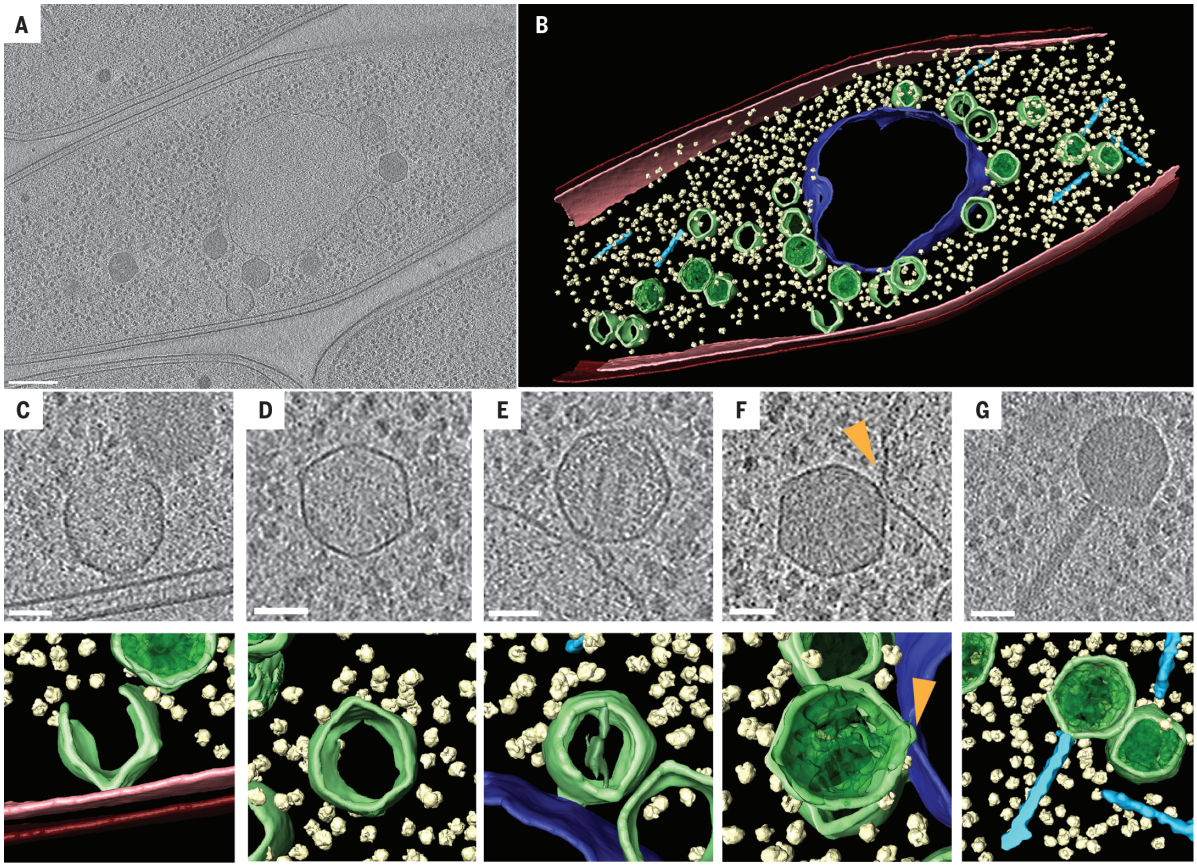

Fig. 4. Cryo-electron tomography of the phage compartment during 201ϕ2-1 infection in *P. chlororaphis*. (**A**) Slice through a tomogram of a cryo-focused ion beam–thinned phage-infected cell at 60 mpi. Assembled capsids are docked to an apparently contiguous shell during the process of DNA encapsidation, which produces the darker, filled capsids. Scale bar, 200 nm. (**B**) Segmentation of the tomogram in (A), showing extracted structures, including the shell (purple), capsids (green), cytoplasmic membrane (pink), outer membrane (red), phage tails (light blue), and ribosomes (yellow). (**C** to **G**) Tomographic slices (top) and segmentation images (bottom) of (C) an assembling phage capsid, (D) an empty capsid, (E and F) two capsids docked at the compartment with (E) less or (F) more DNA, and (G) an assembled phage. Scale bars in (C) to (G), 50 nm. The arrowhead in (F) indicates a connecting collar between the capsid and the compartment shell.

here provides a structure encapsulating the DNA that is pushed by PhuZ filaments. Because phage mRNA transcripts likely originate from inside the compartment, we infer that they must be transported out of the compartment to the cytoplasm to be translated by the ribosomes. Some of the newly expressed proteins, such as those involved in DNA replication and transcription, translocate back into the compartment. How molecules are able to pass in and out of the phage compartment remains unclear. Later during infection, capsids assemble on the cytoplasmic membrane and migrate to the surface of the compartment, where they dock for DNA packaging. After the capsids are filled with DNA, they are released from the surface and coassemble with tails located in the cytoplasm to create mature particles. These results show that phages have evolved a complicated pathway of reproduction in which a bipolar tubulin-based spindle, together with a nucleus-like structure, spatially and temporally organizes DNA replication, transcription, translation, and phage particle assembly. It will be interesting to determine whether this phage-assembly pathway is found in other phages that encode tubulin homologs.

REFERENCES AND NOTES

1. J. Durzyńska, A. Goździcka-Józefiak, *Virol. J.* **12**, 169 (2015).
2. P. Serwer *et al.*, *Virology* **329**, 412–424 (2004).
3. J. A. Thomas *et al.*, *Virology* **376**, 330–338 (2008).
4. J. A. Kraemer *et al.*, *Cell* **149**, 1488–1499 (2012).
5. M. L. Erb *et al.*, *eLife* **3**, e03197 (2014).
6. E. A. Zehr *et al.*, *Structure* **22**, 539–548 (2014).
7. M. Guttman *et al.*, *Proteomics* **9**, 5016–5028 (2009).
8. A. L. McCormack *et al.*, *Anal. Chem.* **69**, 767–776 (1997).
9. A. C. Paoletti *et al.*, *Proc. Natl. Acad. Sci. U.S.A.* **103**, 18928–18933 (2006).
10. E. Villa, M. Schaffer, J. M. Plitzko, W. Baumeister, *Curr. Opin. Struct. Biol.* **23**, 771–777 (2013).
11. S. Q. Zheng, E. Palovcak, J.-P. Armache, Y. Cheng, D. A. Agard, http://biorxiv.org/content/early/2016/07/04/061960 (2016).
12. C. M. Oikonomou, G. J. Jensen, *Nat. Rev. Microbiol.* **14**, 205–220 (2016).

ACKNOWLEDGMENTS

This research was supported by NIH grants GM031627 (D.A.A.), GM104556 (J.P. and D.A.A.), R01-GM57045 (K.P.), and 1DP2GM123494-01 (E.V.) and by the HHMI (D.A.A.). We acknowledge the use of the UCSD Cryo-Electron Microscopy Facility, which is partially supported by NIH grants to T. S. Baker and a gift from the Agouron Institute to UCSD.

SUPPLEMENTARY MATERIALS

www.sciencemag.org/content/355/6321/194/suppl/DC1
Materials and Methods
Figs. S1 to S11
Tables S1 to S3
References (*13*–*20*)
Movies S1 to S8

13 October 2016; accepted 15 December 2016
10.1126/science.aal2130

www.sciencemag.org/content/355/6321/194/suppl/DC1

Supplementary Materials for

Assembly of a nucleus-like structure during viral replication in bacteria

Vorrapon Chaikeeratisak, Katrina Nguyen, Kanika Khanna, Axel F. Brilot, Marcella L. Erb, Joanna K. C. Coker, Anastasia Vavilina, Gerald L. Newton, Robert Buschauer, Kit Pogliano, Elizabeth Villa, David A. Agard, Joe Pogliano*

*Corresponding author. Email: jpogliano@ucsd.edu

Published 13 January 2017, *Science* **355**, 194 (2017)
DOI: 10.1126/science.aal2130

This PDF file includes:

Other Supplementary Material for this manuscript includes the following:
(available at www.sciencemag.org/content/355/6321/194/suppl/DC1)

Materials and Methods

General Methods.

Pseudomonas chlororaphis strain 200-B was grown on Hard Agar (HA) containing 10 g Bacto-Tryptone, 5 g NaCl, and 10 g agar in 1L ddH2O *(2)* and incubated at 30°C. Lysates of 201φ2-1 were made by infecting saturated bacterial culture with 10 µl of high titer lysate, then incubating for 15 minutes at room temperature. 5 ml of HA top agar (0.35%) was added to the infected cultures, then the top agar mixture was poured over a HA plate. The plates were incubated at 30°C overnight. The following day, the plates that formed web lysis were flooded with 5 ml of phage buffer and incubated at room temperature for 6 hours. The phage lysates were then aspirated, clarified by centrifugation at 15,000 rpm for 10 minutes, and stored at 4°C with 0.01% chloroform.

Plasmid and Strain Constructions

All strains were constructed with a pHERD30T *(13)* vector backbone. The phage genes were directly amplified from high-titer lysates of 201φ2-1 with PCR. The plasmids containing phage genes were generated with isothermal assembly followed by direct transformation into *E. coli* DH5A plated on LB supplemented with gentamycin sulfate (final concentration 15 µg/mL). Once the constructs were confirmed with sequencing, they were electroporated into *P. chlororaphis* strain 200-B *(14)*. *P. chlororaphis* strains are grown on HA supplemented with gentamycin sulfate for a final concentration of 25 µg/mL. See Table S3 for list of plasmids and strains.

Fixed cell and live cell fluorescence microscopy.

P. chlororaphis cells were inoculated on 1.2% agarose pads containing 25% Luria Broth, 15 mg/ml gentamycin sulfate, 2 mg/ml FM 4-64, and 1 mg/ml DAPI. Each agarose pad was supplemented with various arabinose concentrations: 0, 0.010%, 0.025%, 0.050%, 0.10%, 0.2%, 0.4%, or 1.0%, to induce expression. The slides were then incubated in a humid chamber at 30°C for 3 hours prior to fluorescent microscopy. To begin the phage infection, 5 µl of high-titer lysate (10^{10} pfu/ml) was added to the agarose pads, and then the cells were further incubated to allow the phage infection occurs. At desired time point after phage infection, a coverslip was put on the slide and microscopy was then initiated. For fixation method, the infected cells were fixed as previously described *(4)*.

The DeltaVision Spectris Deconvolution microscope (Applied Precision, Issaquah, WA, USA) was used to visualize the cells. For static images, the cells were imaged for at least 8 stacks from the focal plane with 0.15 µm increments in the Z-axis and, for time-lapse imaging, the cells were imaged from a single stack at the focal plane for desired length of time with selected intervals with Ultimate Focusing mode. Microscopic images were further processed by the deconvolution algorithm in DeltaVision SoftWoRx Image Analysis Program. Image analysis and processing were performed in Fiji.

Fluorescence Recovery after Photobleaching (FRAP).

Samples were prepared as indicated for fluorescence microscopy. At 45 minutes post infection, GFP-gp105 was photobleached using a laser (QLM module, API) for 0.05 seconds at 100% power and then followed with time-lapse imaging.

Phage Spectral Counting.

P. chlororaphis 200-B cells in mid-log phase were spread onto Hard Agar plates *(2)* and incubated for 3-5 hours at 30°C. 15 µl of 201φ2-1 lysate were gently spread over this nascent lawn and then the plates were returned to 30°C. At the designated time points, cells were scraped off the plate using liquid Hard Agar media, spun down, and the wet pellets weighed, frozen, and stored.

Sample preparation: infected cell preparations were concentrated to >1 x 10^{11} cells/ml using a Speed Vac for in solution protein digestion. RapiGest SF reagent (Waters Corp.) was added to the 0.1 ml lysate sample to a final concentration of 0.1% and samples were boiled for 5 minutes. TCEP (Tris (2-carboxyethyl) phosphine) was added to 1 mM (final concentration) and the samples were incubated at 37°C for 30 minutes. Subsequently, the samples were carboxymethylated with 0.5 mg/ml of iodoacetamide for 30 minutes at 37°C followed by neutralization with 2 mM TCEP (final concentration). Proteins samples prepared as above were digested with Promega sequencing grade modified trypsin (trypsin:protein ratio - 1:50) overnight at 37°C. RapiGest was degraded and removed by treating the samples with 250 mM HCl at 37°C for 1 hours followed by centrifugation at 15,800 xg for 30 min at 4°C. The soluble fraction was then added to a new tube and the peptides were extracted and desalted using a 1 ml SepPak C18 solid phase extraction columns (Waters) *(7)*.

LC-MS/MS analysis.

Trypsin-digested peptides were analyzed by high pressure liquid chromatography (HPLC) coupled with tandem mass spectroscopy (LC-MS/MS) using nano-spray ionization *(8)*. The nanospray ionization experiments were performed using an ABSCIEX TripleTOF 5600 mass spectrometer. Finally, the collected data were analyzed using MASCOT® (Matrix Sciences) and Protein Pilot 4.0 (ABSCIEX) for peptide identifications. The LC MS/MS analysis was performed in the UCSD Biomolecular and proteomics Mass Spectrometry Facility by Majid Ghassemian, Facility Director.

Spectral Counting: For 201φ2-1 peptides, spectral counting was performed on the native mass spec results *(9)*. Spectral counting relies on the correlation between the number of times a peptide from a particular protein strikes the detector and the relative abundance in the sample. An adjusted spectral ratio was calculated for these proteins by counting the number of 95% confidence peptides that struck the detector, divided by the total amino acid length of the protein. This adjusts for the fact that longer proteins generate more peptides that will strike the detector more often solely because of length and not abundance. Only phage proteins with an adjusted spectral ratio of 0.05 or higher were included for analysis. Spectral ratios were also normalized to the total number of peptides detected in each time point to permit comparison of ratios over the course of an infection.

Tomography Sample Preparation and Data Acquisition.

Samples were prepared as indicated for fluorescence microscopy. At 60 minutes post infection, cells were scraped off from the surface of the pad using ¼ LB media. 7 µl of cells were deposited on holey carbon coated 200 mesh copper grids (Quantifoil). Excess media was removed by manually blotting from the side of the grid opposite to the cells using Whatman No. 1 filter paper such that cells form a monolayer on the surface of the grid. Cells were then plunge-frozen in ethane/propane mixture using a custom-built vitrification device.

Grids were then mounted into Modified FEI Autogrids^{TM} to ensure their mechanical stability during subsequent transfer steps. Then, these mounted grids were transferred into a dual-beam (cryo-FIB/SEM) microscope (Scios, FEI) equipped with a cryogenic stage. Thin sections, or lamellae, were prepared as previously described in Villa *et al*., 2013 (see protocol for lamella preparation, not wedges). Each lamella was ~150-200 μm^2 and ~150-200 nm thick, and contained regions of 10-15 cells *(10)*.

Tilt-series were collected from typically -65° to +65° with 1.5° or 2° tilt increments using SerialEM *(15,16)* in a 300-keV Tecnai G2 Polara microscope (FEI) equipped with post-column Quantum Energy Filter (Gatan) and a K2 Summit 4k x 4k direct detector camera (Gatan). Images were recorded at a nominal magnification of 34,000 with a pixel size of 0.61 nm. The dose rate was set to 10-12 e/physical pixel at the camera level. Frame exposure was set to 0.1 seconds, with a total exposure in a frame set to determined by an algorithm targeting an average count number. The total dose in a tomogram was typically ~100e/A^2. The defocus values ranged from -5 to -6 µm.

Movie frames were aligned using MotionCorr2 *(11)* and the defocus was estimated using CTFTILT *(17)* CTF correction and tomogram reconstruction was used with IMOD *(15)*. For visualization purposes, membranes were first segmented automatically using TomoSegMemTV *(18)* an open-source software based on tensor voting. This was followed by segmentation with Amira software (FEI Visualization Sciences Group).

Subtomograms containing ribosomes were picked using EMAN *(19)* and subsequently averaged, classified, and placed in their location in the original tomogram using Dynamo *(20)*.

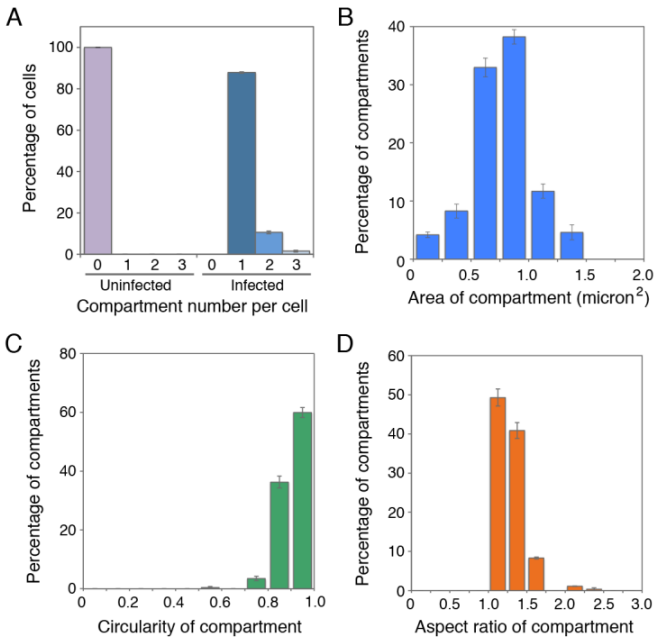

Fig. S1. Quantification of Compartment Formation in *P. chlororaphis*. A. Microscopy was performed on *P. chlororaphis* cells induced with 0.2% arabinose for expression of GFP-gp105. In 100% of uninfected cells (n=1387), fluorescence was diffuse and no structure was seen to form in the cell. In approximately 87% of cells infected with 201φ2-1, one compartment was seen to form while in around 13% of cells, two or more compartments were observed. 264 infected cells were counted overall. **B-D.** The size and shape of the compartment in the infected cell was determined, as reported as area (square microns), circularity and aspect ratio, respectively. The infected cells were induced with 0.2% arabinose, and 286 compartments were measured at 60 mpi. **B.** On average, the majority of compartments (~71%) were between 0.5 and 1.0 micron^2. **C.** In order to determine the circularity of the compartment in infected cells, we used the "analyze particle" filtering function in Fiji with the formula (4*π*area/perimeter^2) where 1.0 defines a perfect circle. About 60% of compartments were observed to form a perfect circle. **D.** In order to determine the aspect ratio of the compartment in infected cells, we used the "analyze particle" filtering function in Fiji with the formula (major_axis/minor_axis). We found that about 50% of compartments had an aspect ratio near 1.0, with the vast majority of compartments (about 98.5%) displaying an aspect ratio between 1.0 and 1.75. Data are mean +/- SEM.

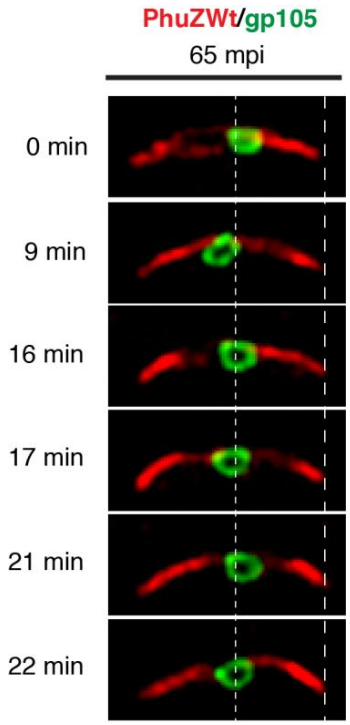

Fig. S2.

Oscillation of the phage nucleus around midcell over the course of 22 minutes. Cells were grown on an agarose pad at 30°C for 3 hours and the fusion proteins (GFP-gp105 and mCherry-PhuZ) were induced with arabinose before phage infection. After 65 minutes of infection (65 mpi), the gp105 shell (green) reaches midcell with the PhuZ spindle (red) at both poles of the cell. The shell oscillates around the middle of the cell suggesting that the opposing filaments of the spindle continue to exert pushing forces.

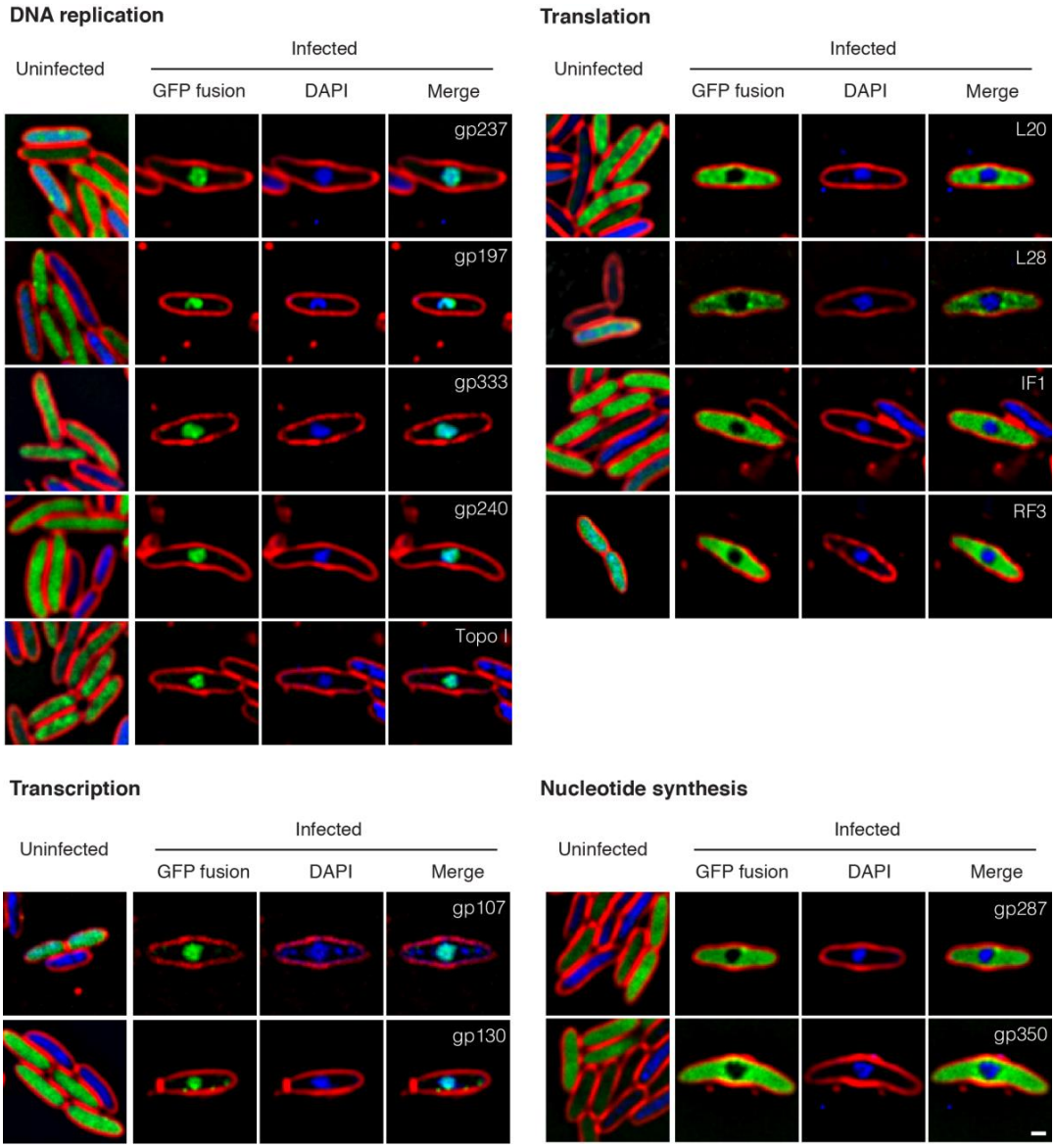

Fig. S3

Localization profiling of phage and host proteins involved in DNA replication, transcription, protein translation and nucleotide synthesis. Cells were grown on an agarose pad at 30°C for 3 hours and GFP fusion proteins were induced with arabinose before phage infection. Membranes are stained with FM 4-64 (red) and DNA with DAPI (blue). After infection, phage proteins (green) involved in DNA replication including DNA helicase (gp197), DNA ligase (gp333), RNase H (gp240), RecA-like or UvsX protein (gp237), and transcription including two homologues of the β' subunits of RNA polymerase (gp107, gp130) co-localize with phage DNA (blue) inside the nucleus as does host-encoded DNA topoisomerase I (Topo I). Phage proteins predicted to be involved in nucleotide synthesis including gp287 (thymidylate monokinase homologue) and gp350

(thymidylate synthase homologue) and the host proteins involved in protein translation (ribosomal protein L20, ribosomal protein L28, translation initiation factor 1 or IF1, and peptide chain release factor 3 or RF3) (green) do not co-localize with phage DNA (blue) indicating that they are excluded from the phage compartment. Thus, protein translation as well as nucleotide synthesis occur outside the phage nucleus. Scale bar, 0.5 μm.

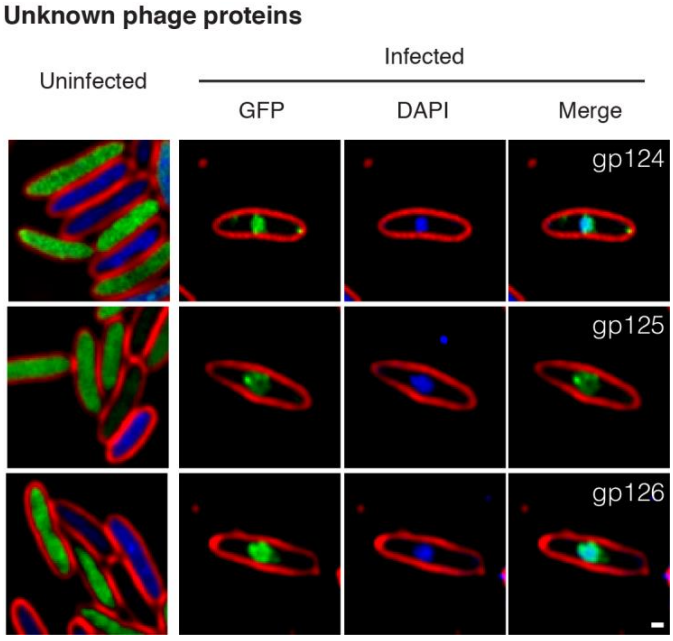

Fig. S4

Localization profiling of unknown phage proteins that are nucleoid-associated. Cells were grown on an agarose pad at 30°C for 3 hours and the GFP fusions to the unknown phage protein were induced with 0.2% arabinose before phage infection. Membranes are stained with FM 4-64 (red) and DNA with DAPI (blue). In uninfected cells, the unknown proteins (gp124, gp125 and gp126) show diffuse cytoplasmic localization. During infection at ~60 mpi, these unknown proteins (green) co-localize with phage DNA (blue). Scale bar, 0.5 μm.

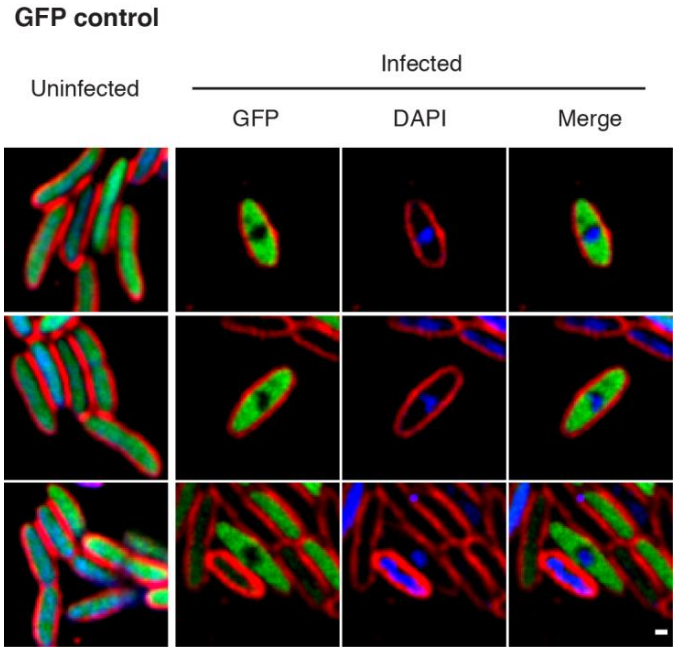

Fig. S5

Localization of GFP in phage infected cells. Three examples each of uninfected and infected cells. Membranes are stained with FM 4-64 (red) and DNA with DAPI (blue). Cells were grown on a pad at 30°C for 3 hours and GFP was induced for expression with 0.5% arabinose prior to phage addition. GFP was excluded from the phage nucleus during infection while in uninfected cells, GFP remained uniformly diffuse throughout the cytoplasm. Scale bar, 0.5 μm.

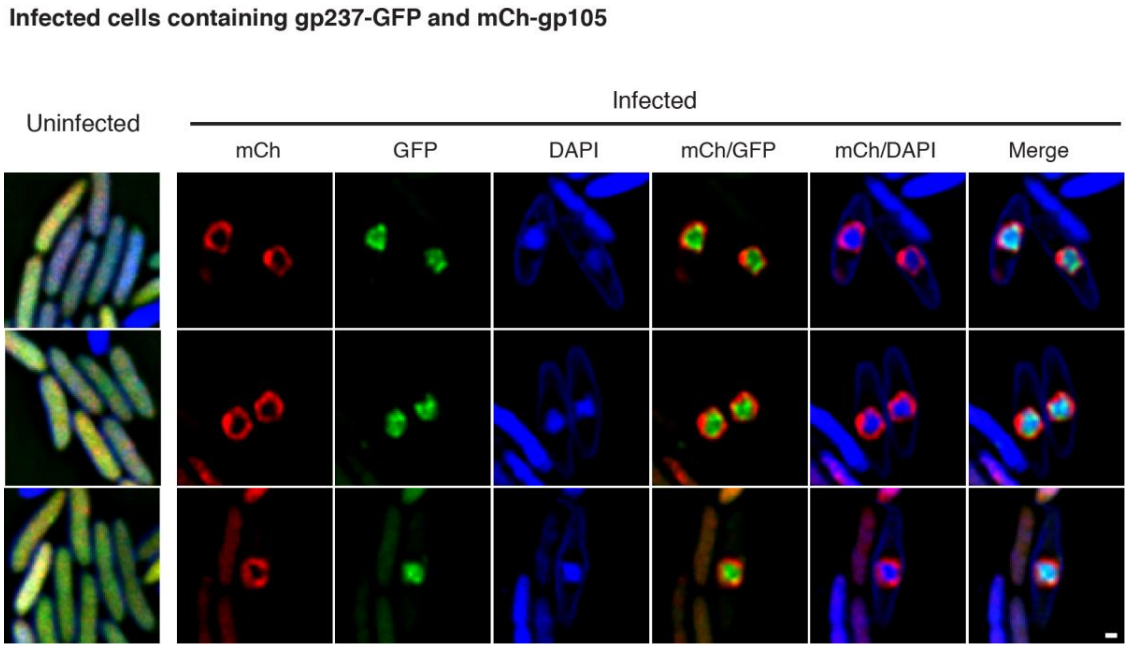

Fig. S6

Fluorescent images showing localization of mCherry-gp105 (red), the RecA homologue gp237-GFP (green), and DAPI stained DNA (blue) in phage infected cells. Three examples of uninfected and infected cells are shown. The cells were grown on an agarose pad at 30°C for 3 hours. The expression of GFP and mCherry fusion protein is induced by 0.25% arabinose. In uninfected cells, mCherry-gp105 (red) and gp237-GFP (green) are uniformly dispersed. At 60 mpi, gp105 (red) assembles into a shell containing gp237 (green) and phage DNA (blue) inside, which is positioned at the middle of infected cells. Thus, gp237 co-localizes with the phage DNA inside the gp105 shell. Scale bar, 0.5 μm.

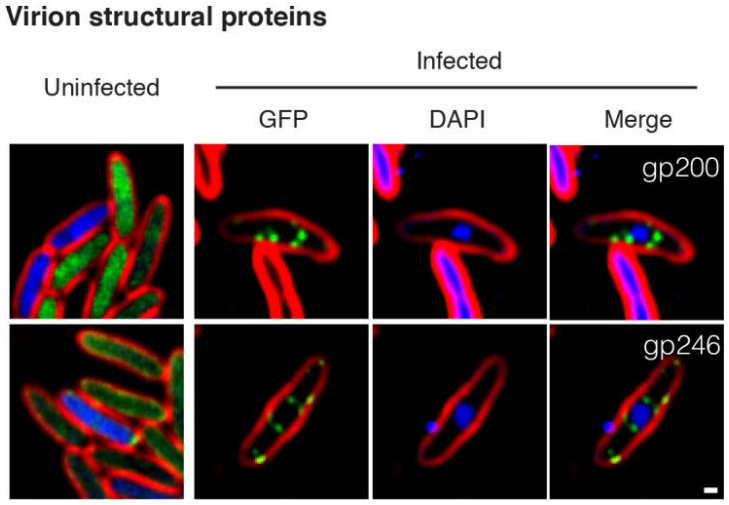

Fig. S7

Localization profiling of the major capsid protein (gp200) and internal head protein (gp246). Cells were grown on an agarose pad at 30°C for 3 hours and GFP fusion protein was expressed by 0.2% arabinose induction prior to phage addition. Membranes are stained with FM 4-64 (red) and DNA with DAPI (blue). During phage infection, the major capsid protein (gp200) and the internal head protein (gp246) both assemble many foci (green) that accumulate and surround the phage DNA (blue) at midcell. No foci are observed in the uninfected cells. Scale bar, 0.5 μm.

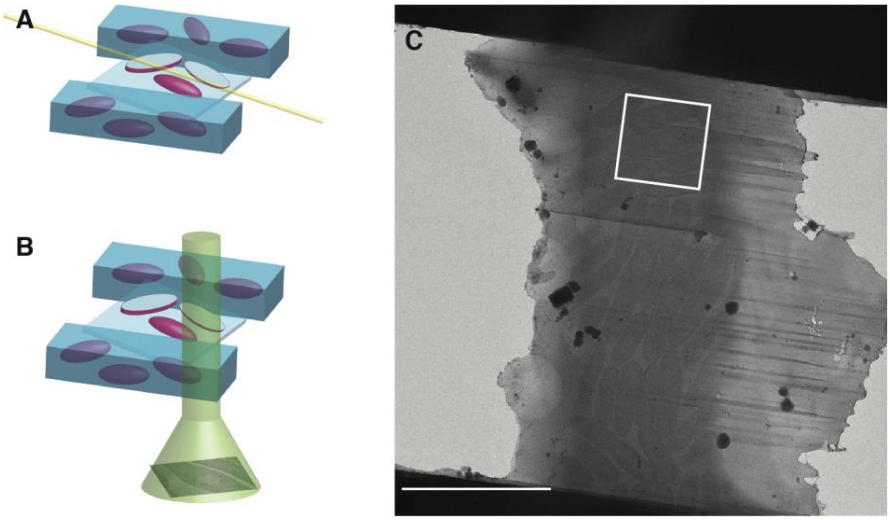

Fig. S8

Workflow for sample preparation and data collection for cryo-electron tomography (CET) of bacterial samples. A. After vitrification, monolayers of bacterial cells are micromachined at cryogenic temperature using a focused ion beam incident at shallow angles (depicted in yellow). The milling leaves windows or lamellae that are thin enough to be electron transparent in TEM. **B.** The thinned samples are used for CET. **C.** FIB-milled lamella of phage-infected cells at 60 mpi. The area where the tomogram in Figure 4 was acquired is marked with a white square; other infected and uninfected cells are present in the lamella. Scale bar: 5 um.

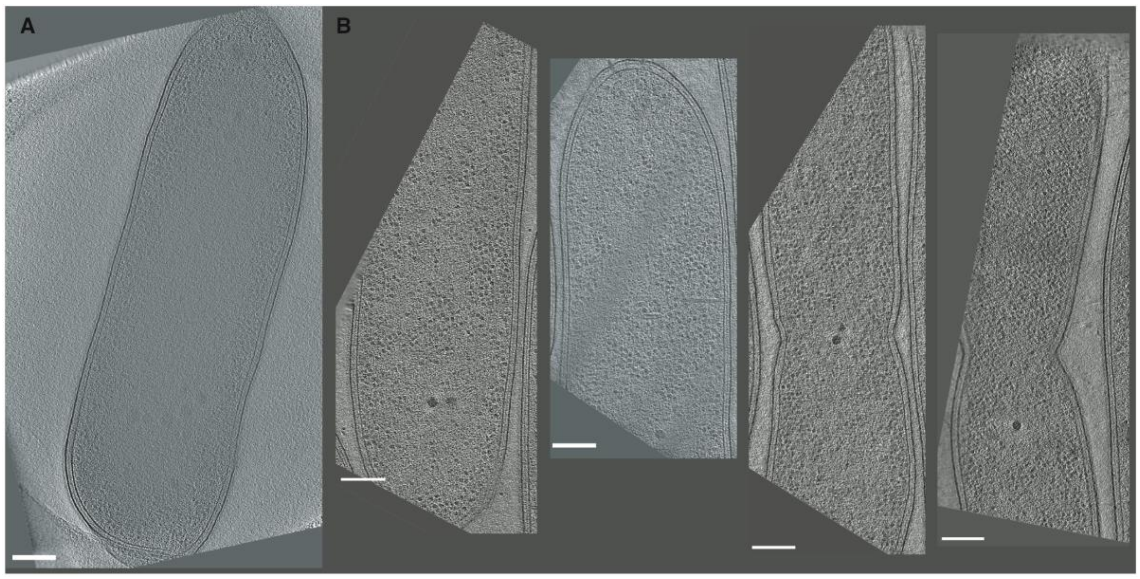

Fig. S9

Tomograms of *P. chlororaphis* cells. A. Uninfected cells were deposited on EM grids and plunge frozen. Tomograms were acquired without FIB milling. Due to the thickness of the cell, the resolution of this tomogram is considerably lower, but it is evident that no nuclear structure exists. **B.** Cells showing no evidence of phage infection from the same experiment shown in Fig. 4 and Figure S8. Ribosomes, carboxysomes, and various cell surface structures are visible. Regions devoid of ribosomes correspond to the cell nucleoid. There is no evidence of infection related structures in these cells. Scale bars: 200 nm.

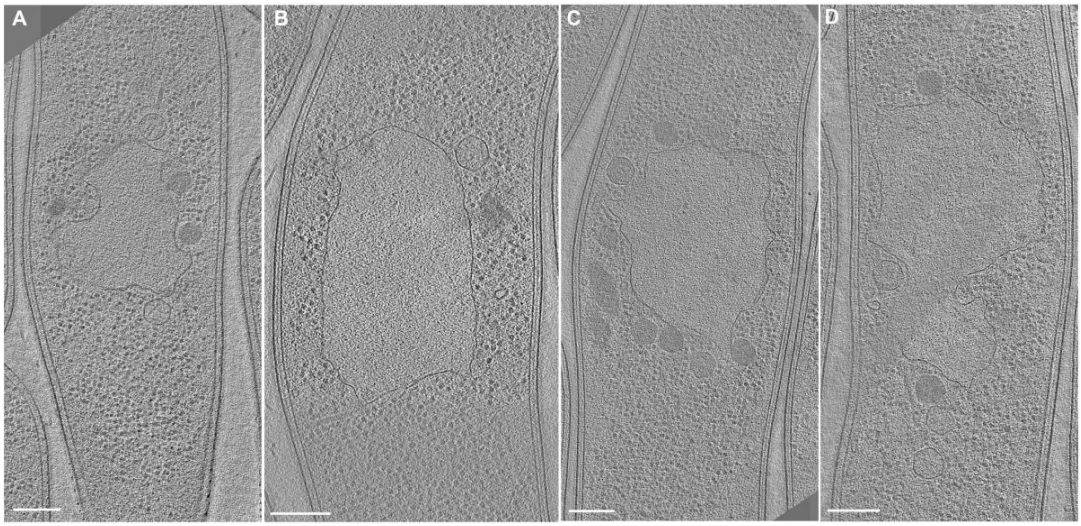

Fig. S10
Tomograms of *P. chlororaphis* infected cells. A-D. Slices through additional tomograms of phage-infected cells at 60 mpi from the same experiment as shown in Fig. 4 depicting irregular shapes of the phage compartment. The dataset for this study included 16 tomograms of phage-infected cells from 8 FIB lamella preparations.

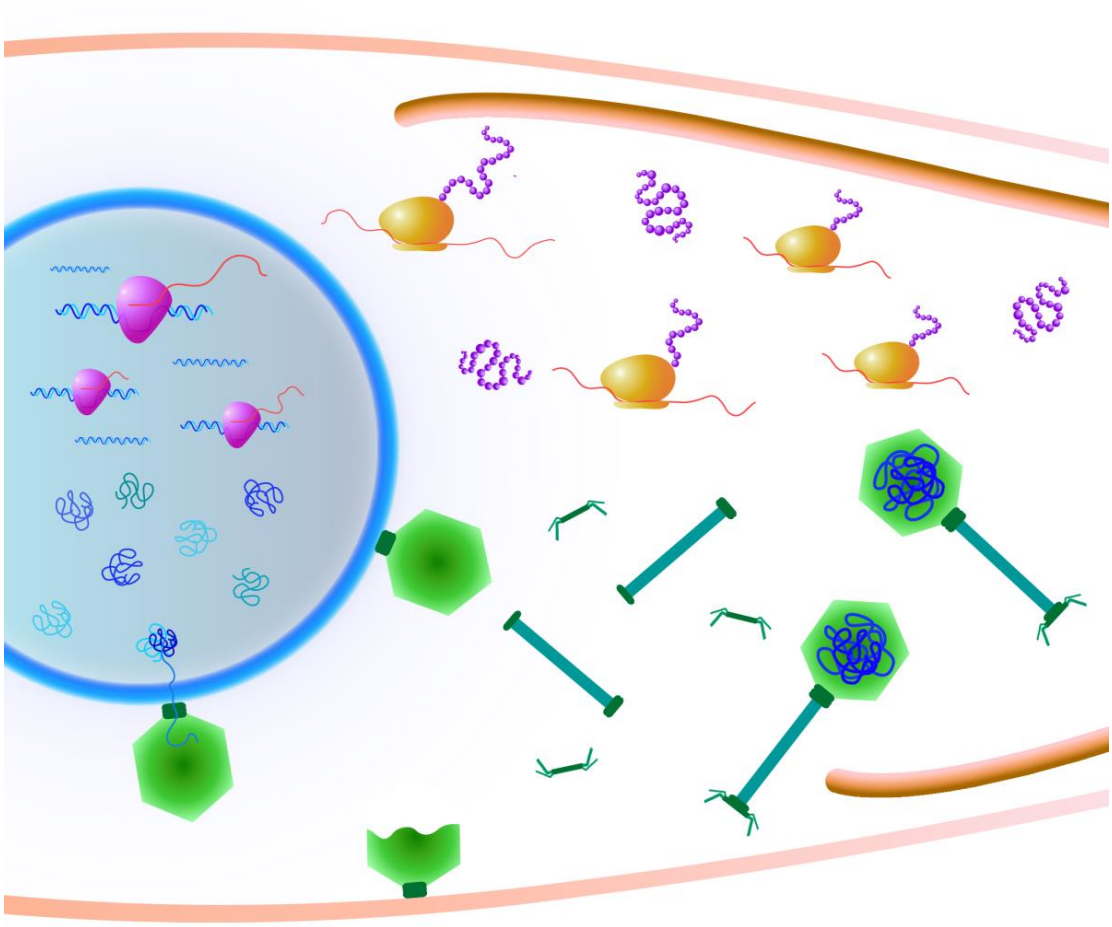

Fig. S11

Cartoon showing the partitioning of DNA replication and transcription inside the phage nucleus, with translation, phage assembly and metabolic processes such as nucleotide biosynthesis in the cytoplasm. Capsid assembly occurs on the cytoplasmic membrane and empty capsids move to the surface of the phage compartment, where they attach for DNA encapsidation. The filled phage capsids detach from the compartment and assembly is completed in the cytoplasm.

Table S1.

Normalized spectral ratio of phage 201φ2-1 proteins present in the infected *Pseudomonas chlororaphis* cells at various time point after infection

Table S1. Normalized spectral ratio of phage 201φ2-1 proteins present in the infected *Pseudomonas Chlororaphis* cells at various time point after infection

non-virion proteins

Accession number	Gene (gp no.)	Amino-acid residues	Identical protein	Normalized spectral ratio				
				0 mpi	10 mpi	20 mpi	30 mpi	60 mpi
gi|189490618	***gp003***	183	dihydrofolate reductase	0	0	0	0	0.005547212
gi|189490177	***gp017***	95	hypothetical	0	0	0	0	0.021371365
gi|189490178	***gp018***	91	hypothetical	0	0	0	0	0.022310766
gi|189490186	***gp026***	90	hypothetical	0	0	0.014192947	0.044444444	0.033837995
gi|189490193	***gp034***	228	hypothetical	0	0	0	0	0.111309194
gi|189490196	***gp037***	100	hypothetical	0	0	0	0.01	0
gi|189490218	***gp059***	315	PhuZ	0	0	0	0.015873016	0.077343989
gi|189490222	***gp063***	69	hypothetical	0	0	0	0	0.014712172
gi|189490231	***gp072***	213	hypothetical	0	0	0	0.009389671	0.052425063
gi|189490240	***gp081***	134	hypothetical	0	0	0	0	0.015151341
gi|189490247	***gp088***	594	hypothetical	0	0	0.002150446	0.006734007	0.020507876
gi|189490252	***gp093***	121	hypothetical	0	0	0	0	0.033558342
gi|189490253	***gp094***	116	hypothetical	0	0	0	0	0.008751206
gi|189490257	***gp098***	363	hypothetical	0	0	0	0	0.002796529
gi|189490261	***gp102***	101	hypothetical	0	0	0	0	0.030152669
gi|189490263	***gp105***	631	hypothetical	0	0	0.050608764	0.18066561	0.424717782
gi|189490264	***gp106***	188	hypothetical	0	0	0	0.010638298	0.03239808
gi|189490266	***gp108***	142	hypothetical	0	0	0	0	0.007148872
gi|189490275	***gp117***	139	hypothetical	0	0	0	0	0.036515822
gi|189490277	***gp119***	168	hypothetical	0	0	0	0	0.114807483
gi|189490278	***gp120***	201	hypothetical	0	0	0	0	0.035353129
gi|189490281	***gp123***	247	Glycine-rich protein	0	0	0	0.056680162	0.271251944
gi|189490282	***gp124***	527	hypothetical	0	0	0	0	0.003852523
gi|189490283	***gp125***	557	hypothetical	0	0	0	0.012567325	0.036450264
gi|189490284	***gp126***	441	hypothetical	0	0	0	0.006802721	0.034528566
gi|189490287	***gp129***	703	RNA polymerase beta subunit	0	0	0	0.001422475	0.002888022
gi|189490288	***gp130***	659	RNA polymerase beta' subunit	0	0	0.001938339	0.001517451	0.030033723
gi|189490293	***gp136***	527	hypothetical	0	0	0	0.001897533	0.077050463
gi|189490294	***gp137***	157	hypothetical	0	0	0	0.006369427	0.116385461
gi|189490297	***gp140***	467	hypothetical (containing Rnase E domain)	0	0	0	0	0.121729832
gi|189490316	***gp160***	290	hypothetical	0	0	0	0	0.014001929
gi|189490327	***gp171***	90	hypothetical	0	0	0	0.011111111	0
gi|189490331	***gp175***	317	hypothetical	0	0	0	0.003154574	0
gi|189490332	***gp176***	69	hypothetical	0	0	0	0	0.029424344
gi|189490334	***gp178***	117	hypothetical	0	0	0	0	0.026029227
gi|189490343	***gp187***	166	hypothetical (conatining Metallophosphatase domain)	0	0	0	0.007142857	0.007250999
gi|189490345	***gp189***	117	hypothetical	0	0	0.021835302	0.008547009	0.017352818
gi|189490353	***gp197***	510	DnaB helicase	0	0	0	0	0.021895173
gi|189490359	***gp204***	696	hypothetical	0	0	0.00367059	0.020114943	0.032087754
gi|189490360	***gp205***	109	hypothetical	0	0	0.011718947	0.036697248	0.111758516
gi|189490361	***gp206***	145	hypothetical	0	0	0	0	0.014001929
gi|189490376	***gp221***	201	hypothetical	0	0	0	0	0.055554917
gi|189490387	***gp232***	160	hypothetical	0	0	0	0	0.012689248
gi|189490389	***gp234***	108	hypothetical	0	0	0	0	0.028198329
gi|189490392	***gp237***	487	hypothetical uvsX	0	0	0	0.002053388	0.035436093
gi|189490395	***gp240***	486	putative RnhA (Rnase HI family)	0	0	0	0	0.008355061
gi|189490409	***gp255***	175	hypothetical	0	0	0	0	0.029003996
gi|189490412	***gp258***	178	hypothetical	0	0	0	0	0.005703033

Accession number	Gene (gp no.)	Amino-acid residues	Identical protein	Normalized spectral ratio				
				0 mpi	10 mpi	20 mpi	30 mpi	60 mpi
gi|189490414	***gp260***	297	hypothetical	0	0	0	0	0.003417979
gi|189490425	***gp271***	629	hypothetical	0	0	0	0	0.016138948
gi|189490427	***gp273/274***	1500	putative RNA polymerase beta subunit	0	0	0	0	0.006090839
gi|189490428	***gp275***	550	hypothetical RNA polymerase beta' subunit	0	0	0	0	0.001845709
gi|189490431	***gp278***	162	hypothetical	0	0	0	0.00617284	0.062662954
gi|189490432	***gp279***	174	hypothetical	0	0	0	0.051724138	0.175024112
gi|189490433	***gp280***	199	hypothetical	0	0	0	0	0.066315669
gi|189490435	***gp282***	406	hypothetical	0	0	0	0.022167488	0.030004134
gi|189490436	***gp283***	136	hypothetical	0	0	0	0.044117647	0.134356745
gi|189490439	***gp287***	357	thymidylate kinase	0	0	0	0.016806723	0.093836457
gi|189490441	***gp289***	121	hypothetical	0	0	0	0.016528926	0.041947928
gi|189490445	***gp293***	125	hypothetical	0	0	0	0.016	0
gi|189490448	***gp296***	143	hypothetical exonuclease	0	0	0	0	0.00709888
gi|189490449	***gp297***	223	hypothetical	0	0	0	0	0.009104393
gi|189490452	***gp300***	710	putative SNF2 domain helicase	0	0	0	0	0.004289323
gi|189490463	***gp311***	304	hypothetical	0	0	0.004201859	0.006578947	0
gi|189490464	***gp312***	183	hypothetical	0	0	0	0.021857923	0.033283274
gi|189490470	***gp319***	270	putative Thg1 (tRNA-His guanylyltransferase)	0	0	0	0.007407407	0.018798886
gi|189490474	***gp323***	124	hypothetical	0	0	0	0	0.008186612
gi|189490479	***gp328***	205	hypothetical	0	0	0	0.024390244	0.014855705
gi|189490481	***gp330***	139	hypothetical	0	0	0	0	0.051122151
gi|189490486	***gp335***	343	hypothetical	0	0	0	0	0.008878774
gi|189490492	***gp341***	271	hypothetical	0	0	0	0.003690037	0.067426263
gi|189490501	***gp349***	132	hypothetical	0	0	0	0	0.015380907
gi|189490502	***gp350***	457	putative thymidylate synthase	0	0	0	0.008752735	0.028877064
gi|189490507	***gp355***	468	putative RNA ligase	0	0	0	0.004273504	0.023860125
gi|189490515	***gp364***	140	hypothetical	0	0	0	0	0.021752997
gi|189490517	***gp366***	205	hypothetical	0	0	0	0	0.009903803
gi|189490520	***gp369***	118	hypothetical	0	0	0	0.008474576	0.01720576
gi|189490521	***gp370***	90	hypothetical	0	0	0	0.011111111	0
gi|189490523	***gp372***	123	hypothetical	0	0	0	0	0.024759509
gi|189490524	***gp373***	199	hypothetical (containing N-Acyltransferase superfamily)	0	0	0	0	0.005101205
gi|189490528	***gp377***	104	hypothetical	0	0	0	0	0.03904384
gi|189490530	***gp379***	118	hypothetical	0	0	0	0	0.01720576
gi|189490532	***gp381***	160	hypothetical	0	0	0	0	0.006344624
gi|189490546	***gp396***	159	hypothetical	0	0	0.008033743	0.006289308	0.006384527
gi|189490569	***gp419***	294	hypothetical	0	0	0	0.003401361	0
gi|189490570	***gp420***	272	hypothetical	0	0	0	0.003676471	0.011196395
gi|189490582	***gp433***	83	hypothetical	0	0	0	0	0.012230601
gi|189490596	***gp447***	206	hypothetical	0	0	0	0.004854369	0.01478359
gi|189490597	***gp448***	192	hypothetical	0	0	0	0	0.021148747
gi|189490603	***gp454***	281	hypothetical	0	0	0	0	0.025288181
gi|189490606	***gp457***	386	hypothetical ribonucleotide reductase beta subunit (NrdB)	0	0	0	0	0.028928856
gi|189490607	***gp458***	141	hypothetical	0	0	0	0	0.02159872
gi|189490609	***gp460***	132	hypothetical	0	0	0.029031027	0.022727273	0
gi|189490614	***gp465***	164	hypothetical	0	0	0	0.006097561	0.012379754
gi|189490615	***gp466***	69	hypothetical	0	0	0	0	0.058848687
gi|189490616	***gp467***	764	hypothetical ribonucleotide reductase alpha subunit (NrdA)	0	0	0	0.001308901	0.074408157

virion proteins

Accession number	Gene (gp no.)	Amino-acid residues	Identical protein	Normalized spectral ratio				
				0 mpi	10 mpi	20 mpi	30 mpi	60 mpi
gi|189490187	***gp027***	553	virion structural protein	0	0	0	0	0.016521263
gi|189490189	***gp029***	311	virion structural protein	0	0	0	0	0.048961729
gi|189490190	***gp030***	700	Tail sheath	0	0	0	0	0.037705194
gi|189490191	***gp032***	291	Major virion structural protein (Tail tube)	0	0	0	0	0.006976906
gi|189490208	***gp049***	115	virion structural protein	0	0	0	0	0.035309212
gi|189490302	***gp146***	145	virion structural protein	0	0	0	0	0.070009645
gi|189490304	***gp148***	414	virion structural protein	0	0	0	0	0.012260143
gi|189490305	***gp149***	974	virion structural protein	0	0	0	0	0.00521119
gi|189490307	***gp151***	400	virion structural protein	0	0	0	0.0025	0.142119579
gi|189490308	***gp152***	297	virion structural protein	0	0	0	0	0.085449482
gi|189490309	***gp153***	177	virion structural protein	0	0	0	0	0.005735253
gi|189490311	***gp155***	608	virion structural protein (Internal head)	0	0	0	0	0.056767689
gi|189490312	***gp156***	387	virion structural protein (Internal head)	0	0	0	0	0.018361703
gi|189490313	***gp157***	489	virion structural protein (Internal head)	0	0	0	0	0.006227852
gi|189490315	***gp159***	922	virion structural protein (RNA recongition motif)	0	0	0	0	0.05174791
gi|189490349	***gp193***	381	virion structural protein	0	0	0	0	0.045294954
gi|189490354	***gp198***	180	virion structural protein	0	0	0	0	0.011279332
gi|189490355	***gp200***	746	Major capsid protein	0	0.005369169	0.011986	0.012064343	0.291206338
gi|189490367	***gp212***	290	virion structural protein	0	0	0	0	0.003500482
gi|189490368	***gp213***	723	virion structural protein	0	0	0	0	0.001404066
gi|189490369	***gp214***	917	virion structural protein	0	0	0	0	0.001107023
gi|189490371	***gp216***	738	virion structural protein	0	0	0	0	0.015130811
gi|189490372	***gp217***	107	virion structural protein	0	0	0	0	0.018974577
gi|189490374	***gp219***	458	virion structural protein	0	0	0	0	0.004432925
gi|189490379	***gp224***	298	virion structural protein	0	0	0	0	0.034065096
gi|189490385	***gp230***	1480	virion structural protein (containing collagen triple helix repeat)	0	0.000902117	0.002589254	0	0.054186519
gi|189490388	***gp233***	224	virion structural protein	0	0	0	0	0.004531874
gi|189490393	***gp238***	316	virion structural protein	0	0	0	0	0.003212468
gi|189490397	***gp243***	449	virion structural protein	0	0	0	0	0.029391577
gi|189490400	***gp246***	613	virion structural protein (Internal head)	0	0	0.004167586	0.006525285	0.205346397
gi|189490401	***gp247***	397	virion structural protein (Internal head)	0	0	0	0	0.020456219
gi|189490422	***gp268***	280	virion structural protein	0	0	0	0	0.014501998
gi|189490533	***gp382***	117	virion structural protein	0	0	0	0	0.251615861
gi|189490604	***gp455***	768	virion structural protein (containing Helix-turn-helix XRE family like protein)	0	0	0	0	0.005287187

Table S2.
Native Peptides-Single 90 minute run on ABI 5600. Searched with *Pseudomonas fluorescens* + Phage 201φ2-1

Table S2. Native Peptides-Single 90 min run on ABI 5600. Searched with *Pseudomonas fluorescens* + Phage 201φ2-1

Sample	Spectra	% Identified	Total peptides	Total Proteins	Phage Peptides	Phage Proteins
Uninfected	18,310	83	3322	564	0	0
10 min	16,130	81	2,963	525	2	2
20 min	16,685	80	3,097	559	28	13
30 min	21,689	82	3,956	647	98	49
60 min	21,103	82	3,897	658	410	123

Table S3.

List of plasmids and strains used in the study

Table S3. List of plasmids and strains used in the study

Construct	*Plasmid*	*Strain*
GFP-gp105	pJC001	JC002
GFP-gp105-mCh-PhuZ	pVC060	VC343
GFP-gp105-mCh-PhuZD190A	pVC061	VC345
gp237-GFP	pVC008	VC127
gp197-GFP	pVC022	VC189
gp333-GFP	pKN025	KN067
gp240-GFP	pVC023	VC190
PC-Topo I-GFP	pVC068	VC367
gp124-GFP	pVC026	VC196
gp125-GFP	pVC005	VC122
gp126-GFP	pVC006	VC123
gp107-GFP	pKN023	KN063
gp130-GFP	pVC073	VC391
PC-50s-L20-GFP	pVC069	VC369
PC-50s-L28-GFP	pKN026	KN073
PC-IF1-GFP	pVC072	VC385
PC-Prf3-GFP	pKN030	KN081
gp287-GFP	pVC009	VC129
gp350-GFP	pVC010	VC131
gp237-GFP-mCh-gp105	pVC067	VC358
gp200-GFP	pVC007	VC125
gp246-GFP	pVC012	VC135
gp200-GFP-mCh-gp105	pVC058	VC327

References and Notes

1. J. Durzyńska, A. Goździcka-Józefiak, Viruses and cells intertwined since the dawn of evolution. *Virol*. *J*. **12**, 169 (2015). doi:10.1186/s12985-015-0400-7 Medline

2. P. Serwer, S. J. Hayes, S. Zaman, K. Lieman, M. Rolando, S. C. Hardies, Improved isolation of undersampled bacteriophages: Finding of distant terminase genes. *Virology* **329**, 412–424 (2004). doi:10.1016/j.virol.2004.08.021 Medline

3. J. A. Thomas, M. R. Rolando, C. A. Carroll, P. S. Shen, D. M. Belnap, S. T. Weintraub, P. Serwer, S. C. Hardies, Characterization of *Pseudomonas chlororaphis* myovirus 201φ2-1 via genomic sequencing, mass spectrometry, and electron microscopy. *Virology* **376**, 330–338 (2008). doi:10.1016/j.virol.2008.04.004 Medline

4. J. A. Kraemer, M. L. Erb, C. A. Waddling, E. A. Montabana, E. A. Zehr, H. Wang, K. Nguyen, D. S. L. Pham, D. A. Agard, J. Pogliano, A phage tubulin assembles dynamic filaments by an atypical mechanism to center viral DNA within the host cell. *Cell* **149**, 1488–1499 (2012). doi:10.1016/j.cell.2012.04.034 Medline

5. M. L. Erb, J. A. Kraemer, J. K. C. Coker, V. Chaikeeratisak, P. Nonejuie, D. A. Agard, J. Pogliano, A bacteriophage tubulin harnesses dynamic instability to center DNA in infected cells. *eLife* **3**, e03197 (2014). doi:10.7554/eLife.03197 Medline

6. E. A. Zehr, J. A. Kraemer, M. L. Erb, J. K. C. Coker, E. A. Montabana, J. Pogliano, D. A. Agard, The structure and assembly mechanism of a novel three-stranded tubulin filament that centers phage DNA. *Structure* **22**, 539–548 (2014). doi:10.1016/j.str.2014.02.006 Medline

7. M. Guttman, G. N. Betts, H. Barnes, M. Ghassemian, P. van der Geer, E. A. Komives, Interactions of the NPXY microdomains of the low density lipoprotein receptor-related protein 1. *Proteomics* **9**, 5016–5028 (2009). doi:10.1002/pmic.200900457 Medline

8. A. L. McCormack, D. M. Schieltz, B. Goode, S. Yang, G. Barnes, D. Drubin, J. R. Yates III, Direct analysis and identification of proteins in mixtures by LC/MS/MS and database searching at the low-femtomole level. *Anal*. *Chem*. **69**, 767–776 (1997). doi:10.1021/ac960799q Medline

9. A. C. Paoletti, T. J. Parmely, C. Tomomori-Sato, S. Sato, D. Zhu, R. C. Conaway, J. W. Conaway, L. Florens, M. P. Washburn, Quantitative proteomic analysis of distinct mammalian Mediator complexes using normalized spectral abundance factors. *Proc*. *Natl*. *Acad*. *Sci*. *U*.*S*.*A*. **103**, 18928–18933 (2006). doi:10.1073/pnas.0606379103 Medline

10. E. Villa, M. Schaffer, J. M. Plitzko, W. Baumeister, Opening windows into the cell: Focused-ion-beam milling for cryo-electron tomography. *Curr*. *Opin*. *Struct*. *Biol*. **23**, 771–777 (2013). doi:10.1016/j.sbi.2013.08.006 Medline

11. S. Q. Zheng, E. Palovcak, J.-P. Armache, Y. Cheng, D. A. Agard, http://biorxiv.org/content/early/2016/07/04/061960 (2016).

12. C. M. Oikonomou, G. J. Jensen, A new view into prokaryotic cell biology from electron cryotomography. *Nat*. *Rev*. *Microbiol*. **14**, 205–220 (2016). doi:10.1038/nrmicro.2016.7 Medline

13. D. Qiu, F. H. Damron, T. Mima, H. P. Schweizer, H. D. Yu, P_{BAD}-based shuttle vectors for functional analysis of toxic and highly regulated genes in *Pseudomonas* and *Burkholderia* spp. and other bacteria. *Appl*. *Environ*. *Microbiol*. **74**, 7422–7426 (2008). doi:10.1128/AEM.01369-08 Medline

14. G. T. Howard, R. I. Mackie, I. K. O. Cann, S. Ohene-Adjei, K. S. Aboudehen, B. G. Duos, G. W. Childers, Effect of insertional mutations in the *pueA* and *pueB* genes encoding two polyurethanases in *Pseudomonas chlororaphis* contained within a gene cluster. *J*. *Appl*. *Microbiol*. **103**, 2074–2083 (2007). doi:10.1111/j.1365-2672.2007.03447.x Medline

15. D. N. Mastronarde, Dual-axis tomography: An approach with alignment methods that preserve resolution. *J*. *Struct*. *Biol*. **120**, 343–352 (1997). doi:10.1006/jsbi.1997.3919 Medline

16. D. N. Mastronarde, Automated electron microscope tomography using robust prediction of specimen movements. *J*. *Struct*. *Biol*. **152**, 36–51 (2005). doi:10.1016/j.jsb.2005.07.007 Medline

17. A. Rohou, N. Grigorieff, CTFFIND4: Fast and accurate defocus estimation from electron micrographs. *J*. *Struct*. *Biol*. **192**, 216–221 (2015). doi:10.1016/j.jsb.2015.08.008 Medline

18. A. Martinez-Sanchez, I. Garcia, S. Asano, V. Lucic, J.-J. Fernandez, Robust membrane detection based on tensor voting for electron tomography. *J*. *Struct*. *Biol*. **186**, 49–61 (2014). doi:10.1016/j.jsb.2014.02.015 Medline

19. J. G. Galaz-Montoya, J. Flanagan, M. F. Schmid, S. J. Ludtke, Single particle tomography in EMAN2. *J*. *Struct*. *Biol*. **190**, 279–290 (2015). doi:10.1016/j.jsb.2015.04.016 Medline

20. D. Castaño-Díez, M. Kudryashev, M. Arheit, H. Stahlberg, *Dynamo*: A flexible, user-friendly development tool for subtomogram averaging of cryo-EM data in high-performance computing environments. *J*. *Struct*. *Biol*. **178**, 139–151 (2012). doi:10.1016/j.jsb.2011.12.017 Medline

Acknowledgements

Chapter 2, in full, is a reprint of the material as it appears in the January 12, 2017 edition of *Science*. Chaikeeratisak, V., Nguyen, K., Khanna, K., Brilot, A.F., Erb, M.L., Coker, J.K., Vavilina, A., Newton, G.L., Buschauer, R., Pogliano, K., Villa, E., Agard, D.A., Pogliano, J. (2017). Assembly of a nucleus-like structure during viral replication in bacteria. *Science 355*, 194-197. The dissertation author was a significant contributor to this paper.

Report

Cell Reports

The Phage Nucleus and Tubulin Spindle Are Conserved among Large *Pseudomonas* Phages

Graphical Abstract

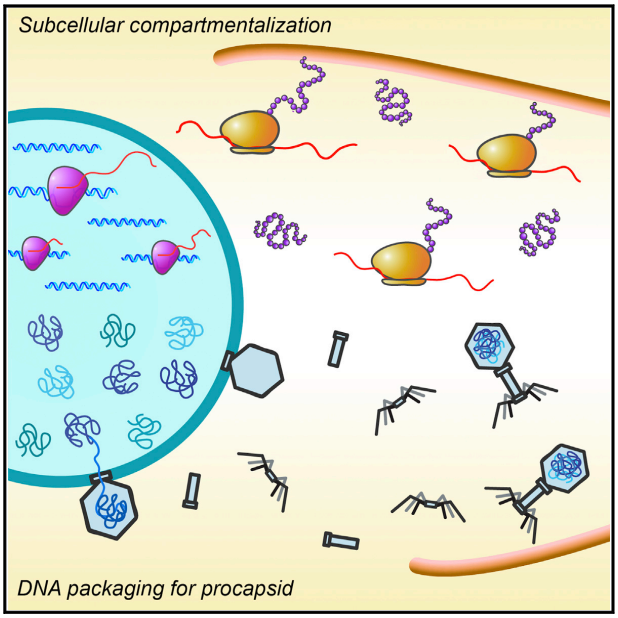

Authors

Vorrapon Chaikeeratisak, Katrina Nguyen, MacKennon E. Egan, Marcella L. Erb, Anastasia Vavilina, Joe Pogliano

Correspondence

jpogliano@ucsd.edu

In Brief

The nucleus and spindle are defining features of eukaryotic cells that separate them from bacteria and archaea. Chaikeeratisak et al. show that a tubulin-based spindle and a nucleus-like structure are conserved among large *Pseudomonas* phages, providing insight into the evolution of these key cell biological structures.

Highlights

- The phage nucleus segregates phage and host bacterial proteins according to function
- The phage nucleus is centered by the PhuZ bipolar tubulin spindle
- The phage nucleus and phage spindle are conserved in large *Pseudomonas* phages

Chaikeeratisak et al., 2017, Cell Reports *20*, 1563–1571
August 15, 2017
http://dx.doi.org/10.1016/j.celrep.2017.07.064

Cell Reports
Report

The Phage Nucleus and Tubulin Spindle Are Conserved among Large *Pseudomonas* Phages

Vorrapon Chaikeeratisak,[1] Katrina Nguyen,[1] MacKennon E. Egan,[1] Marcella L. Erb,[1] Anastasia Vavilina,[1] and Joe Pogliano[1,2,*]
[1]Division of Biological Sciences, University of California, San Diego, La Jolla, CA 92093, USA
[2]Lead Contact
*Correspondence: jpogliano@ucsd.edu
http://dx.doi.org/10.1016/j.celrep.2017.07.064

SUMMARY

We recently demonstrated that the large *Pseudomonas chlororaphis* bacteriophage 201φ2-1 assembles a nucleus-like structure that encloses phage DNA and segregates proteins according to function, with DNA processing proteins inside and metabolic enzymes and ribosomes outside the nucleus. Here, we investigate the replication pathway of the *Pseudomonas aeruginosa* bacteriophages φKZ and φPA3. Bacteriophages φKZ and φPA3 encode a proteinaceous shell that assembles a nucleus-like structure that compartmentalizes proteins and DNA during viral infection. We show that the tubulin-like protein PhuZ encoded by each phage assembles a bipolar spindle that displays dynamic instability and positions the nucleus at midcell. Our results suggest that the phage spindle and nucleus play the same functional role in all three phages, 201φ2-1, φKZ, and φPA3, demonstrating that these key structures are conserved among large *Pseudomonas* phages.

INTRODUCTION

Bacteria generally lack a nucleus, the membrane-bound organelle that separates genetic material from the cytoplasm in eukaryotes. We recently described a nucleus-like structure in bacteria, assembled by phage 201Φ2-1 in *Pseudomonas chlororaphis* cells during infection (Chaikeeratisak et al., 2017). This "phage nucleus" is bound by a proteinaceous barrier composed of gp105 that encloses viral DNA and separates cellular functions. Like the eukaryotic equivalent, DNA replication and transcription occur inside the phage nucleus, while translation and metabolic enzymes are localized in the cytoplasm. While a membrane-bound structure containing chromosomal DNA has been reported in *Planctomycetes*, it also contains ribosomes, indicating that proteins and DNA are not compartmentalized separately (Boedeker et al., 2017; Fuerst and Sagulenko, 2011; Sagulenko et al., 2017). The subcellular organization observed during phage 201Φ2-1 infection of *Pseudomonas chlororaphis* (*P. chlororaphis*) is unique and prompted us to investigate if it is conserved during replication of other phages.

Positioning of the phage nucleus is controlled by PhuZ, a phage-encoded tubulin which shares only ~18% amino acid sequence identity with the *E. coli* cell division protein FtsZ (Chaikeeratisak et al., 2017; Kraemer et al., 2012). The crystal structure of PhuZ revealed that it contains a conserved tubulin fold with a long C-terminal aspartic acid rich tail (Kraemer et al., 2012). PhuZ assembles a unique three-stranded polymer in which protofilaments twist around each other, and the C-terminal tail plays a key role in making longitudinal contacts with adjacent subunits (Zehr et al., 2014). PhuZ filaments display dynamic instability both *in vitro* and *in vivo* (Erb et al., 2014). During phage infection, PhuZ forms a bipolar spindle composed of dynamically unstable filaments that position phage DNA at midcell (Erb et al., 2014). Mutations in the catalytic domain that eliminate PhuZ GTPase activity disrupt both spindle dynamics and phage nucleus positioning and reduce phage burst size by 50% (Erb et al., 2014; Kraemer et al., 2012). The PhuZ spindle is the only known example of a cytoskeletal structure in bacteria or archaea that shares three key properties with the eukaryotic spindle: dynamic instability, a bipolar array of filaments, and central positioning of DNA. Phage-encoded tubulins like PhuZ may represent a transitional evolutionary step between simplified bacterial filaments, such as FtsZ and *Bacillus* plasmid segregation protein TubZ (Aylett et al., 2010; Chen and Erickson, 2008; Larsen et al., 2007; Montabana and Agard, 2014) and more complicated structures like the eukaryotic spindle. Further insight into PhuZ and its relatives may allow us to dissect the evolutionary relationships between the cytoskeletal proteins of phages, bacteria, and eukaryotes.

Here, we investigate *Pseudomonas aeruginosa* phages ΦPA3 (Monson et al., 2011) and ΦKZ (Mesyanzhinov et al., 2002), which encode homologs of PhuZ. Like $PhuZ_{201}$, both $PhuZ_{\Phi PA3}$ and $PhuZ_{\Phi KZ}$ assemble filaments *in vitro* (Aylett et al., 2013; Zehr et al., 2014). The conservation of certain critical interactions in $PhuZ_{\Phi PA3}$, as well as the pattern produced by a 2D class average of segments of filaments suggest that $PhuZ_{\Phi PA3}$ also forms a three-stranded polymer like that of $PhuZ_{201}$ (Zehr et al., 2014). $PhuZ_{\Phi KZ}$ has a tubulin fold and assembles filaments and protofilaments similar to those of $PhuZ_{201}$ (Aylett et al., 2013). It was previously proposed that despite the high level of conservation seen in the tertiary structures of $PhuZ_{\Phi KZ}$ and $PhuZ_{201}$, the divergence of the protein sequence might result in different functional roles of these two proteins (Aylett et al., 2013). Here, we show that assembly of a nucleus-like structure and the biological function of the phage-encoded tubulin are conserved in the reproduction pathways of these three phages.

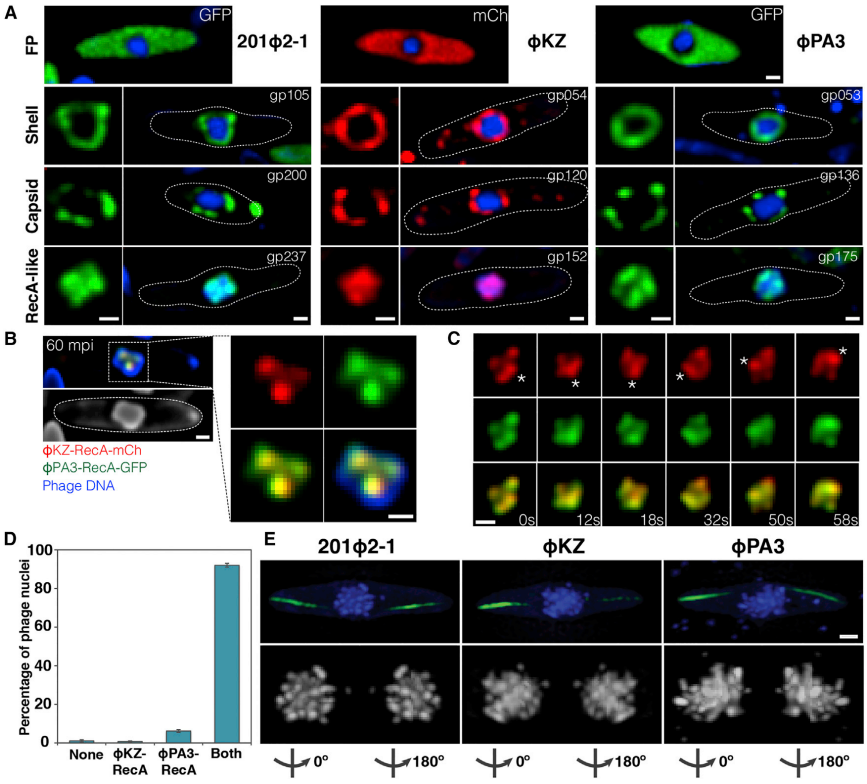

Figure 1. 201Φ2-1, ΦKZ, and ΦPA3 Assemble a Nucleus-like Structure that Compartmentalizes Proteins and DNA during Viral Replication

(A–E) Cells were grown on an agarose pad, and the fusion proteins were induced with arabinose at the indicated concentrations. *P. chlororaphis* was infected with 201Φ2-1 and *P. aeruginosa* with phages ΦKZ or ΦPA3 and imaged at approximately 60 mpi (A, B, and D) or 90 mpi (C and E). Phage DNA is stained with DAPI (blue). These proteins do not assemble in uninfected cells. All scale bars represent 0.5 μm.

(A) Top row: fluorescence micrographs of infected *P. chlororaphis* and infected *P. aeruginosa* cells expressing fluorescent proteins (GFP, green) or (mCherry, red) alone from the arabinose promoter. Fluorescence micrographs of infected *P. chlororaphis* and infected *P. aeruginosa* cells expressing fluorescent protein fusions to the conserved nuclear shell proteins gp105 of 201Φ2-1 (0.2% arabinose), gp054 of ΦKZ (0.025% arabinose), and gp053 of ΦPA3 (0.025% arabinose) are shown (second row). In rows two through four, the square panel on the left is an enlarged image of fluorescent proteins shown within cells whose border is indicated by a dotted line. Fluorescence micrographs of infected *P. chlororaphis* and infected *P. aeruginosa* cells expressing fluorescent protein fusions to the major capsid proteins gp200 of 201Φ2-1 (0.2% arabinose), gp120 of ΦKZ (0.05% arabinose), and gp136 of ΦPA3 (0.05% arabinose) are shown (third row). Fluorescence micrographs of infected *P. chlororaphis* and infected *P. aeruginosa* cells expressing fluorescent protein fusions to the RecA-like protein gp237 of 201Φ2-1 (0.2% arabinose), gp152 of ΦKZ (0.025% arabinose), and gp175 of ΦPA3 (0.025% arabinose) are shown (fourth row).

(B) Co-localization of RecA-related proteins ΦKZ-gp152-mCherry (red) and ΦPA3-gp175-GFP (green) in the 201Φ2-1 nucleus (stained blue by DAPI or gray) during phage 201Φ2-1 infection. *P. chlororaphis* expressing ΦKZ-gp152-mCherry and ΦPA3-gp175-GFP (0.1% arabinose) was infected with 201Φ2-1 and visualized at 60 mpi. The region indicated by a dashed box is magnified and shown on the right. Scale bar, 0.5 μm.

(C) Time-lapse imaging (s) of ΦKZ-gp152-mCherry (red) and ΦPA3-gp175-GFP (green) in the 201Φ2-1 nucleus showing both RecA-related proteins form foci which move together as the 201Φ2-1 nucleus rotates over the course of 58 s. The position of the focus (asterisk) was tracked for the duration of the time-lapse. Scale bar, 0.5 μm. See also Movie S1.

(D) Graph showing percentage of 201Φ2-1 nuclei of infected *P. chlororaphis* cells containing no proteins inside (none), either ΦKZ-gp152 or ΦPA3-gp175 inside, or both RecA-related proteins inside. Data were collected from the infected cells at 60 mpi from at least three different fields and are represented as mean ± SEM (n = 263).

(E) SIM images of infected *P. chlororaphis* and infected *P. aeruginosa* at 90 mpi showing encapsidated phage clusters localized at midcell as determined by DAPI staining (blue or gray). GFP-PhuZ filaments (green) extend from both cell poles toward the viral nucleus at midcell. 3D-SIM and rotation of the phage nucleus around the y axis show that the nucleus is surrounded with encapsidated phages (degree of rotation is indicated below each subset). Scale bar, 0.5 μm.

See also Figure S1.

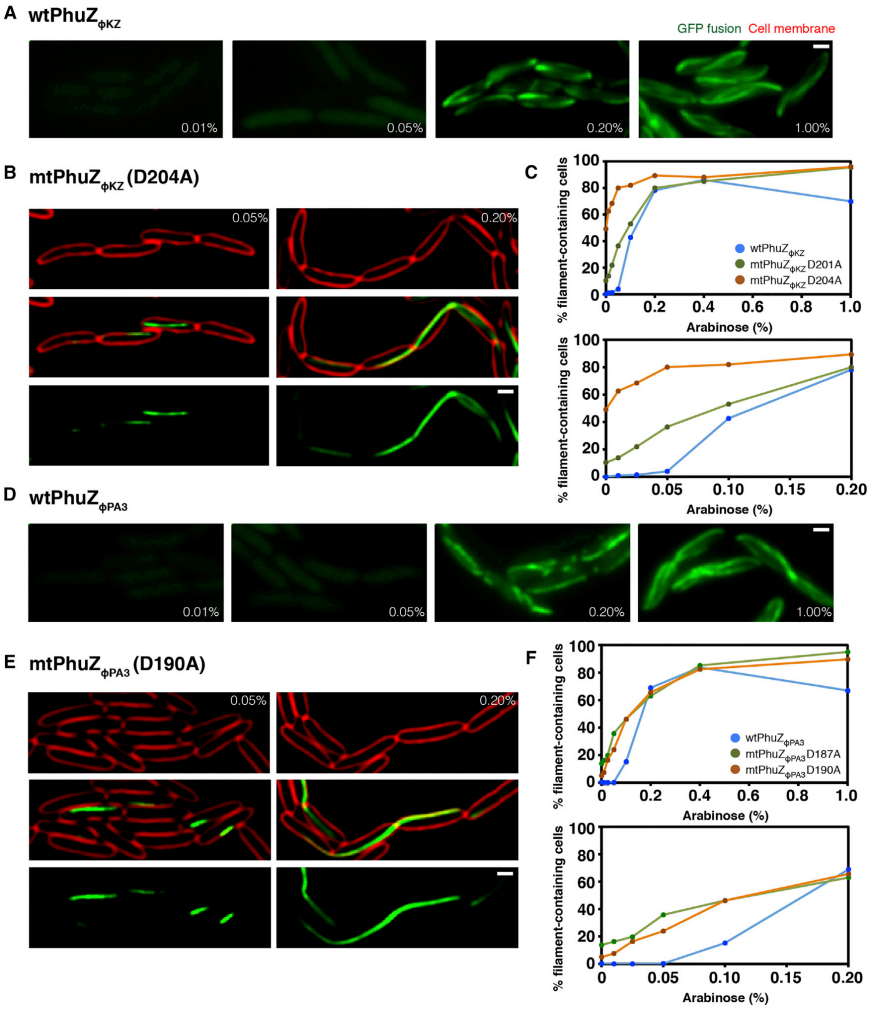

Figure 2. PhuZ Requires a Critical Threshold Concentration to Polymerize in *P. aeruginosa*

Cells were grown on an agarose pad, and the fusion proteins were induced at the indicated arabinose concentrations. Cell membranes were stained with FM4-64 (red). All scale bars represent 1 μm.

(A) Fluorescence images of cells expressing wild-type GFP-PhuZ$_{\phi KZ}$ at the indicated arabinose concentrations.

(B) *P. aeruginosa* cells expressing the GTPase mutant GFP-PhuZ$_{\phi KZ}$D204A at the indicated arabinose concentrations.

(C) Graph showing the percentage of cells containing either wild-type or mutant PhuZ$_{\phi KZ}$ (D201A or D204A) filaments when fusion proteins are expressed at increasing levels of arabinose ranging from 0% to 1%. The graph below replots the same data showing the range of arabinose concentration from 0% to 0.2%. Data represented as mean values were collected from the induced cells at indicated arabinose concentration from at least three different fields with at least 200 cells per field.

(D) Fluorescence images of cells expressing wild-type GFP-PhuZ$_{\phi PA3}$ at the indicated arabinose concentrations.

(E) *P. aeruginosa* cells expressing the GTPase mutant GFP-PhuZ$_{\phi PA3}$D190A at the indicated arabinose concentrations.

(F) Graph showing the percentage of cells containing either wild-type or mutant PhuZ$_{\phi PA3}$ (D187A or D190A) filaments when fusion proteins are expressed at increasing levels of arabinose ranging from 0% to 1%. The graph below replots the same data showing the range of arabinose concentration from 0% to 0.2%. Data represented as mean values were collected from the induced cells at indicated arabinose concentration from at least three different fields with at least 200 cells per field.

See also Figures S2 and S3.

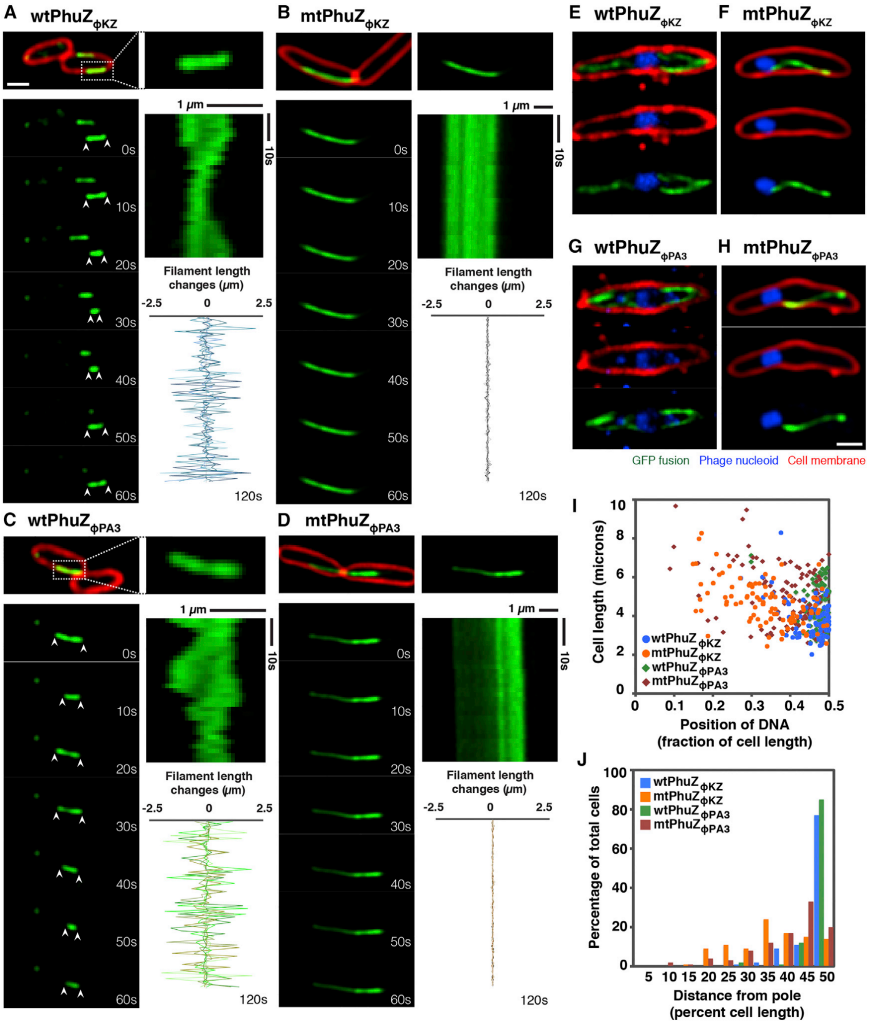

Figure 3. PhuZ$_{\Phi KZ}$ and PhuZ$_{\Phi PA3}$ Show Dynamic Instability and Center the Phage Nucleus in the Cell, While the GTPase Mutants Fail to Position the Nucleus at Midcell

Cells were grown on agarose pads, and the fusion proteins were induced with 0.05% arabinose (below the critical threshold for filament assembly) for infected cells and with 0.1% arabinose (to study the dynamic instability of filaments) for uninfected cells. Cell membranes were stained red by FM4-64 and phage DNA was stained blue by DAPI. All scale bars represent 1 μm.

(A and C) Fluorescence micrographs of uninfected *P. aeruginosa* cells induced at 0.1% arabinose to express wild-type GFP-PhuZ$_{\Phi KZ}$ (A) and wild-type GFP-PhuZ$_{\Phi PA3}$ (C). The filament in the dashed box is magnified and shown on the right. Time-lapse imaging and kymograph for one representative filament for each protein (GFP-PhuZ$_{\Phi KZ}$, A, and GFP-PhuZ$_{\Phi PA3}$, C) and a graph showing length changes for five representative filaments for each protein show that these filaments display dynamic instability.

(B and D) Fluorescence micrographs of uninfected *P. aeruginosa* cells induced at 0.1% arabinose to express mutant GFP-PhuZ$_{\Phi KZ}$ (B) and mutant GFP-PhuZ$_{\Phi PA3}$ (D). Time-lapse imaging and kymograph for one representative filament are shown. The graph shows length changes of five representative mutant filaments.

(E and G) Fluorescence micrographs of ΦKZ-infected (E) and ΦPA3-infected (G) *P. aeruginosa* cells induced at 0.05% arabinose to express wild-type GFP-PhuZ$_{\Phi KZ}$ (E) or wild-type GFP-PhuZ$_{\Phi PA3}$ (G). The dynamic GFP-PhuZ spindle (green) was assembled and phage nucleus (blue) was centered in the infected cell at 60 mpi.

(legend continued on next page)

is approximately linear in *P. aeruginosa* with arabinose concentrations below 0.5% (Figure S3C), and proteins are expressed at uniform levels among cells throughout the population (Figure S3D). These results suggest that both GFP-PhuZ$_{\Phi KZ/\Phi PA3}$ monomers must reach a threshold critical concentration for assembly to occur, as is the case with PhuZ$_{201}$, TubZ, and other tubulins. To confirm the presence of the catalytic T7 loops in the PhuZ homologs, we generated mutations in this motif in which the conserved aspartic acid was replaced by alanine: GFP-PhuZ$_{\Phi KZ}$-D201A or D204A and GFP-PhuZ$_{\Phi PA3}$-D187A or D190A (Figures 2B, 2E, S3E, and S3F). When these mutant proteins were expressed in *P. aeruginosa*, filaments appeared at a comparatively lower arabinose concentration, 0.05%, suggesting that the catalytic point mutant requires a lower concentration for stable filament assembly (Figures 2C and 2F), as we previously observed with PhuZ$_{201}$ catalytic mutants. The mutant proteins formed long polymers that often became trapped in septa during cell division, resulting in extensive chaining of cells (Figures 2B, 2E, S3E, and S3F).

PhuZ$_{\Phi KZ}$ and PhuZ$_{\Phi PA3}$ Polymers Display Dynamic Instability

Dynamic instability is a key property of microtubules that allows them to search space and to center chromosomal DNA. PhuZ$_{201}$ forms filaments that undergo dynamic instability, which is essential for its function of centering the phage nucleus. We therefore set out to determine if PhuZ$_{\Phi KZ}$ and PhuZ$_{\Phi PA3}$ also display dynamic instability *in vivo*. When we expressed GFP-PhuZ$_{\Phi KZ}$ and GFP-PhuZ$_{\Phi PA3}$ above the apparent critical threshold concentration for assembly in uninfected *P. aeruginosa* cells, the filaments displayed evidence of dynamic instability, undergoing cycles of polymerization and depolymerization (Figures 3A and 3C). Figures 3A–3D show time-lapse microscopy of individual filaments over the course of 1 min. Quantitation of filament length over time shows that the ends of the wild-type PhuZ$_{\Phi PA3}$ and PhuZ$_{\Phi KZ}$ filaments are dynamically unstable, continuously extending and retracting over a period of 2 min (Figures 3A and 3C, graphs). In contrast, time-lapse microscopy and quantitation of filament length of GFP-PhuZ$_{\Phi KZ}$-D204A and GFP-PhuZ$_{\Phi PA3}$-D187A showed that the mutant filaments remained the same length over the course of 2 min (Figures 3B and 3D, graphs), suggesting that dynamic instability requires GTPase activity, as is the case with PhuZ$_{201}$ and microtubules.

The PhuZ Bipolar Spindle Centers the Phage Nucleus after Infection with Phages ΦKZ and ΦPA3

PhuZ$_{201}$ is involved in the centering of the phage nucleus during infection of *P. chlororaphis*. To determine if PhuZ$_{\Phi KZ}$ and PhuZ$_{\Phi PA3}$ also assemble a bipolar spindle, we expressed GFP-PhuZ$_{\Phi KZ}$ and GFP-PhuZ$_{\Phi PA3}$ from a plasmid in *P. aeruginosa* below the critical threshold for filament assembly with very low levels of arabinose induction. We previously established with phage 201Φ2-1 that expressing a small amount of GFP-tagged PhuZ to visualize the spindle does not significantly interfere with the spindle's ability to display dynamic instability or center the phage nucleus. Based on calculations of the total number of PhuZ monomers in the cell required to form the three-stranded filaments of the bipolar spindle and assuming a critical concentration of assembly of ~2.5 μM based on measurements of PhuZ$_{201}$ (Kraemer et al., 2012), we expect this level of induction to produce less than 20% of the total PhuZ protein in the cell. Western blot analysis (Figure S3G) verified that plasmid-expressed GFP-PhuZ accounted for less than 1/3 of the total PhuZ protein produced at 60 and 90 mpi.

After induction of GFP-PhuZ at this low level (0.05% arabinose), we infected cells with either ΦKZ or ΦPA3 and observed PhuZ filament formation 60 mpi. In uninfected cells, no filaments were observed, but upon phage infection, GFP-PhuZ assembled dynamic filaments that extended from both poles of the cell toward the nucleus at midcell, forming a bipolar spindle-like structure similar to that observed for PhuZ$_{201}$ (Figures 1E, 3E, 3G, S4A, and S4C). The phage nucleus was located within 10% of the cell center in approximately 80% of cells after infection with ΦKZ (n = 100) or ΦPA3 (n = 100) (Figures 3I and 3J). In contrast to wild-type, the catalytic mutants GFP-PhuZ$_{\Phi KZ}$-D204A and GFP-PhuZ$_{\Phi PA3}$-D187A behaved as dominant negatives that co-assembled with the wild-type proteins and formed static polymers that disrupt spindle dynamics and viral DNA positioning. Cells expressing the PhuZ catalytic mutants typically had one long static filament per cell instead of a pair of filaments surrounding the phage nucleus, as seen in wild-type cells (Figures 3F, 3H, S4B, and S4D). In addition, expression of the mutant proteins led to mispositioning of the phage nucleus (Figures 3F and 3H–3J). Less than 20% of cells expressing GFP-PhuZ$_{\Phi KZ}$-D204A (n = 100) or GFP-PhuZ$_{\Phi PA3}$-D187A (n = 100) had a centered phage nucleus (Figures 3I and 3J). These data suggest that a bipolar spindle formed by dynamic PhuZ polymers is responsible for centering the phage nucleus of ΦKZ and ΦPA3 and, therefore, the biological function of PhuZ is conserved in all three phages.

DISCUSSION

We recently described a nucleus-like structure assembled by phage 201Φ2-1 during *P. chlororaphis* infection and its role during the lytic life cycle. The phage reorganizes the bacterial cell,

(F and H) Fluorescence micrographs of ΦKZ-infected (F) and ΦPA3-infected (H) *P. aeruginosa* cells induced at 0.05% arabinose to express mutant GFP-PhuZ$_{\Phi KZ}$ (F) and mutant GFP-PhuZ$_{\Phi PA3}$ (H). The mutant PhuZ proteins (green) assembled a single static filament instead of a bipolar spindle resulting in mispositioning of the phage nucleus (blue) at 60 mpi.

(I) Graph showing the position of the phage nucleus in *P. aeruginosa* cells, expressed as a fraction of cell length. Cells expressed either wild-type GFP-PhuZ$_{\Phi KZ}$ (blue circle), wild-type GFP-PhuZ$_{\Phi PA3}$ (green diamond), GTPase mutant GFP-PhuZ$_{\Phi KZ}$ (orange circle), or GTPase mutant GFP-PhuZ$_{\Phi PA3}$ (red diamond). 100 cells were counted for each group.

(J) Histogram showing position of the phage nucleus in which the data from (I) are replotted as percentage of total cells. Cells expressed either wild-type GFP-PhuZ$_{\Phi KZ}$ (blue), wild-type GFP-PhuZ$_{\Phi PA3}$ (green), GTPase mutant GFP-PhuZ$_{\Phi KZ}$ (orange), or GTPase mutant GFP-PhuZ$_{\Phi PA3}$ (red). 100 cells were counted for each group.

See also Figures S3 and S4.

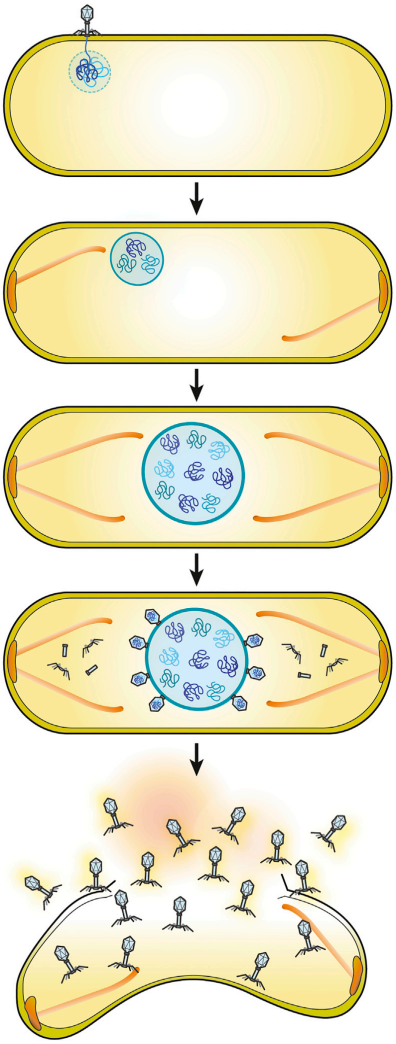

Figure 4. Model of Phage Nucleus Assembly and Its Role in the Viral Life Cycle in Large *Pseudomonas* Phages

As soon as the phage injects DNA into its host, the nuclear shell protein assembles a compartment to protect its genomic DNA from host defenses and to provide a compartment for DNA replication. Dynamically unstable PhuZ filaments set up a spindle with one end anchored at the cell pole, while the other end of the spindle pushes the compartment toward midcell. The spindle might rely upon a yet to be discovered factor that organizes its assembly. As DNA replication proceeds inside the compartment, the nucleus grows in size as it is pushed toward the cell center. Late during infection, capsids dock on the surface of the phage nucleus for DNA encapsidation. The mature phage particles are assembled in the cytoplasm and the host cell lyses.

forming a proteinaceous shell that encloses viral DNA and enzymes involved in DNA replication and transcription, while excluding metabolic enzymes and ribosomes. The tubulin PhuZ assembles a bipolar spindle that plays a key role in positioning the phage nucleus at midcell (Figure 4). Here, we show that two major components of this replication pathway, the phage nucleus and spindle, are conserved in the related phages ΦKZ and ΦPA3. This remarkable level of organization has not been seen in other bacteriophages or in bacterial or archaeal cells.

We now show three examples of bacterial viruses with both a nucleus and a tubulin-based spindle, raising the question of how such a complicated system might benefit phage reproduction. One possibility is that the phage nucleus might provide protection for viral DNA from host defenses, such as restriction enzymes or CRISPR/Cas systems. In addition, the phage nucleus could also protect against the phage's own nucleases, which were previously shown to degrade bacterial chromosomal DNA after infection (Erb et al., 2014). A protective barrier might confer a selective advantage, despite the potential added cost of the system. An enclosed structure containing replicating viral DNA requires phage capsids to dock on the surface for DNA encapsidation. If this compartment were located adjacent to the cell membrane near the cell pole, access to a significant portion of its surface would be sterically hindered. Therefore, the spindle might have subsequently evolved to position the nucleus at midcell to provide greater unobstructed surface area for diffusion of molecules in and out of the phage nucleus and for docking of viral capsids. The discovery that viruses evolved both a spindle and a nucleus is in line with previous hypotheses concerning the role of viruses in the evolution of eukaryotic life (Bell, 2001, 2009; Forterre, 2006; Koonin, 2016; Takemura, 2001; Villarreal and DeFilippis, 2000). In particular, the theory of viral eukaryogenesis suggests, in part, that the eukaryotic nucleus evolved when a poxvirus infected an archaeal cell. We speculate that our data support and expand the model of viral eukaryogenesis and suggest that a virus may have provided the origin for the tubulin-based spindle as well as the first step toward nuclear compartmentalization.

These results also provide insight into the plasticity of tubulin, and its ability to form a bipolar spindle composed of dynamically unstable filaments despite significant divergence in amino acid sequences. While $PhuZ_{ΦKZ}$ and $PhuZ_{ΦPA3}$ share only 31% and 46% sequence identity (respectively) with $PhuZ_{201}$, both formed dynamically unstable bipolar spindles that positioned phage DNA at midcell, and mutations in the catalytic T7 loops of these tubulins resulted in mispositioning of phage DNA. These findings are consistent with those previously outlined for *P. chlororaphis* phage 201Φ2-1 and show that the centering function is conserved among large bacteriophages infecting different *Pseudomonas* species. In comparison with eukaryotic alpha/beta tubulin, which forms 13 stranded microtubules, PhuZ shares less than 11% amino acid identity and assembles three-stranded filaments. Despite the large divergence in sequence, PhuZ filaments still display dynamic instability *in vitro* and *in vivo* similar to eukaryotic microtubules, suggesting that tubulin sequences can undergo extensive variation and evolution, yet retain the ability to assemble filaments with similar dynamic properties.

EXPERIMENTAL PROCEDURES

Strains, Growth Conditions, and Bacteriophage Preparation

P. chlororaphis strain 200-B and *P. aeruginosa* strain PA01 were grown on hard agar (HA) (Serwer et al., 2004) and Luria-Bertani (LB) media, respectively. Lysates of each phage (201Φ2-1, ΦPA3, and ΦKZ) were made by infecting saturated bacterial culture with 10 μL of high-titer lysate, then incubating for 15 min at room temperature. 5 mL of HA or LB top agar (0.35%) was added to the infected cultures, then the top agar mixture was poured over a HA or LB plate. The plates were incubated at 30°C overnight. The following day, the plates that formed web lysis (nearly confluent lysis) were flooded with 5 mL of phage buffer and incubated at room temperature for 6 hr. The phage lysates were then aspirated, clarified by centrifugation at 15,000 rpm for 10 min, and stored at 4°C with 0.01% chloroform.

Plasmid Constructions and Bacterial Transformation

Plasmids, as listed in Table S1, were introduced into *P. chlororaphis* strain 200-B and *P. aeruginosa* strain PA01 by electroporation. All bacterial cultures were grown at 30°C. For additional details, please see Supplemental Experimental Procedures.

Fluorescence Microscopy

Pseudomonas cells were inoculated on 1.2% agarose pads in concavity slides. Each pad was supplemented with desired arabinose concentrations to induce the protein expression, 1 μg/mL FM4-64 for membrane staining, and 1 μg/mL DAPI for DNA staining (Pogliano et al., 1999). The slides were then incubated in a humid chamber at 30°C for 3 hr for *P. chlororaphis* strain 200-B and at 37°C for 2 hr for *P. aeruginosa* strain PA01 prior to fluorescence microscopy.

The DeltaVision Spectris Deconvolution Microscope (Applied Precision, Issaquah, WA, USA) was used to visualize the cells. For static images, the cells were imaged for at least eight stacks from the middle focal plane with 0.15 μm increments in the z axis and, for time-lapse imaging, the cells were imaged from a single stack at the focal plane with the ultimate focusing mode. Microscopic images were further processed by the deconvolution algorithm in the DeltaVision SoftWoRx Image Analysis Program.

Fixed Cell Imaging

Cells were prepared on 1.2% agarose pads as for live-cell imaging. At desired time point, cells were fixed with paraformaldehyde and glutaraldehyde and washed with 1× PBS, as described by Kraemer et al. (2012). Before imaging, the slides were then covered with a coverslip. Data of static images were collected and processed as stated above.

Single-Cell Phage Infection

As described above, *Pseudomonas* cells were grown on 1.2% agarose pads, supplemented with the desired concentration of arabinose to induce fluorescently tagged protein expression to label wild-type proteins from phage, and then incubated at 30°C for 3 hr without a coverslip in a humid chamber. To begin the phage infection, 3 μL of high-titer lysate (10^8 pfu/mL) was added to the cells on agarose pads, and then the cells were further incubated to allow the phage infection to occur. At the desired time point after phage infection, a coverslip was put on the slide and fluorescence microscopy was then initiated. Data of static images and time-lapse imaging were collected and processed as stated above.

3D-SIM Super-Resolution Microscopy

Pseudomonas cells were grown and infected on 1.2% agar pads and then fixed with paraformaldehyde and gluteraldehyde as stated above. Cells were subsequently stained with 1 μg/mL DAPI and then imaged using an Applied Precision/GE OMX V2.2 Microscope. Microscopic raw data were sequentially taken by SI-super-resolution light path to collect 3 μm thickness of samples with 125 nm increments in the z axis with compatible immersion oils (Applied Precision). 3D-SIM images were then rendered by standard OMX SI reconstruction parameters in DeltaVision SoftWoRx Image Analysis Program.

Statistical Analysis

The number of cells analyzed in the experiments or the number of experimental replicates is indicated in the figure legends. All data are shown as mean values or mean ± SEM. Student's t test was performed for unpaired data with unequal variance (a p value less than 0.05 shows a significant difference).

SUPPLEMENTAL INFORMATION

Supplemental Information includes Supplemental Experimental Procedures, four figures, one table, and one movie and can be found with this article online at http://dx.doi.org/10.1016/j.celrep.2017.07.064.

AUTHOR CONTRIBUTIONS

V.C. and K.N. conception and design, acquisition of data, analysis and interpretation of data, and drafting or revising the article; M.E.E., M.L.E., and A.V. acquisition of data; and J.P. conception and design, analysis and interpretation of data, and drafting or revising the article.

ACKNOWLEDGMENTS

This research was supported by NIH grant GM104556 (to J.P.). We acknowledge the use of the UCSD Neuroscience Microscopy Shared Facility, which is financially supported by NINDS grant P30 NS047101.

Received: March 29, 2017
Revised: July 13, 2017
Accepted: July 24, 2017
Published: August 15, 2017

REFERENCES

Aylett, C.H., Wang, Q., Michie, K.A., Amos, L.A., and Löwe, J. (2010). Filament structure of bacterial tubulin homologue TubZ. Proc. Natl. Acad. Sci. USA *107*, 19766–19771.

Aylett, C.H., Izoré, T., Amos, L.A., and Löwe, J. (2013). Structure of the tubulin/FtsZ-like protein TubZ from Pseudomonas bacteriophage ΦKZ. J. Mol. Biol. *425*, 2164–2173.

Bell, P.J. (2001). Viral eukaryogenesis: was the ancestor of the nucleus a complex DNA virus? J. Mol. Evol. *53*, 251–256.

Bell, P.J. (2009). The viral eukaryogenesis hypothesis: a key role for viruses in the emergence of eukaryotes from a prokaryotic world environment. Ann. N Y Acad. Sci. *1178*, 91–105.

Boedeker, C., Schüler, M., Reintjes, G., Jeske, O., van Teeseling, M.C., Jogler, M., Rast, P., Borchert, D., Devos, D.P., Kucklick, M., et al. (2017). Determining the bacterial cell biology of Planctomycetes. Nat. Commun. *8*, 14853.

Chaikeeratisak, V., Nguyen, K., Khanna, K., Brilot, A.F., Erb, M.L., Coker, J.K., Vavilina, A., Newton, G.L., Buschauer, R., Pogliano, K., et al. (2017). Assembly of a nucleus-like structure during viral replication in bacteria. Science *355*, 194–197.

Chen, Y., and Erickson, H.P. (2008). In vitro assembly studies of FtsZ/tubulin-like proteins (TubZ) from Bacillus plasmids: evidence for a capping mechanism. J. Biol. Chem. *283*, 8102–8109.

Erb, M.L., Kraemer, J.A., Coker, J.K., Chaikeeratisak, V., Nonejuie, P., Agard, D.A., and Pogliano, J. (2014). A bacteriophage tubulin harnesses dynamic instability to center DNA in infected cells. eLife *3*, 3.

Forterre, P. (2006). The origin of viruses and their possible roles in major evolutionary transitions. Virus Res. *117*, 5–16.

Fuerst, J.A., and Sagulenko, E. (2011). Beyond the bacterium: planctomycetes challenge our concepts of microbial structure and function. Nat. Rev. Microbiol. *9*, 403–413.

Koonin, E.V. (2016). Viruses and mobile elements as drivers of evolutionary transitions. Philos. Trans. R. Soc. Lond. B Biol. Sci. *371*, 371.

Kraemer, J.A., Erb, M.L., Waddling, C.A., Montabana, E.A., Zehr, E.A., Wang, H., Nguyen, K., Pham, D.S., Agard, D.A., and Pogliano, J. (2012). A phage tubulin assembles dynamic filaments by an atypical mechanism to center viral DNA within the host cell. Cell *149*, 1488–1499.

Larsen, R.A., Cusumano, C., Fujioka, A., Lim-Fong, G., Patterson, P., and Pogliano, J. (2007). Treadmilling of a prokaryotic tubulin-like protein, TubZ, required for plasmid stability in Bacillus thuringiensis. Genes Dev. *21*, 1340–1352.

Mesyanzhinov, V.V., Robben, J., Grymonprez, B., Kostyuchenko, V.A., Bourkaltseva, M.V., Sykilinda, N.N., Krylov, V.N., and Volckaert, G. (2002). The genome of bacteriophage phiKZ of Pseudomonas aeruginosa. J. Mol. Biol. *317*, 1–19.

Monson, R., Foulds, I., Foweraker, J., Welch, M., and Salmond, G.P. (2011). The Pseudomonas aeruginosa generalized transducing phage phiPA3 is a new member of the phiKZ-like group of 'jumbo' phages, and infects model laboratory strains and clinical isolates from cystic fibrosis patients. Microbiology *157*, 859–867.

Montabana, E.A., and Agard, D.A. (2014). Bacterial tubulin TubZ-Bt transitions between a two-stranded intermediate and a four-stranded filament upon GTP hydrolysis. Proc. Natl. Acad. Sci. USA *111*, 3407–3412.

Pogliano, J., Osborne, N., Sharp, M.D., Abanes-De Mello, A., Perez, A., Sun, Y.L., and Pogliano, K. (1999). A vital stain for studying membrane dynamics in bacteria: a novel mechanism controlling septation during Bacillus subtilis sporulation. Mol. Microbiol. *31*, 1149–1159.

Sagulenko, E., Nouwens, A., Webb, R.I., Green, K., Yee, B., Morgan, G., Leis, A., Lee, K.C., Butler, M.K., Chia, N., et al. (2017). Nuclear pore-like structures in a compartmentalized bacterium. PLoS ONE *12*, e0169432.

Serwer, P., Hayes, S.J., Zaman, S., Lieman, K., Rolando, M., and Hardies, S.C. (2004). Improved isolation of undersampled bacteriophages: finding of distant terminase genes. Virology *329*, 412–424.

Takemura, M. (2001). Poxviruses and the origin of the eukaryotic nucleus. J. Mol. Evol. *52*, 419–425.

Villarreal, L.P., and DeFilippis, V.R. (2000). A hypothesis for DNA viruses as the origin of eukaryotic replication proteins. J. Virol. *74*, 7079–7084.

Zehr, E.A., Kraemer, J.A., Erb, M.L., Coker, J.K., Montabana, E.A., Pogliano, J., and Agard, D.A. (2014). The structure and assembly mechanism of a novel three-stranded tubulin filament that centers phage DNA. Structure *22*, 539–548.

Cell Reports, Volume *20*

Supplemental Information

The Phage Nucleus and Tubulin Spindle Are Conserved among Large *Pseudomonas* Phages

Vorrapon Chaikeeratisak, Katrina Nguyen, MacKennon E. Egan, Marcella L. Erb, Anastasia Vavilina, and Joe Pogliano

Figure S1 *[Related to Figure 1]*

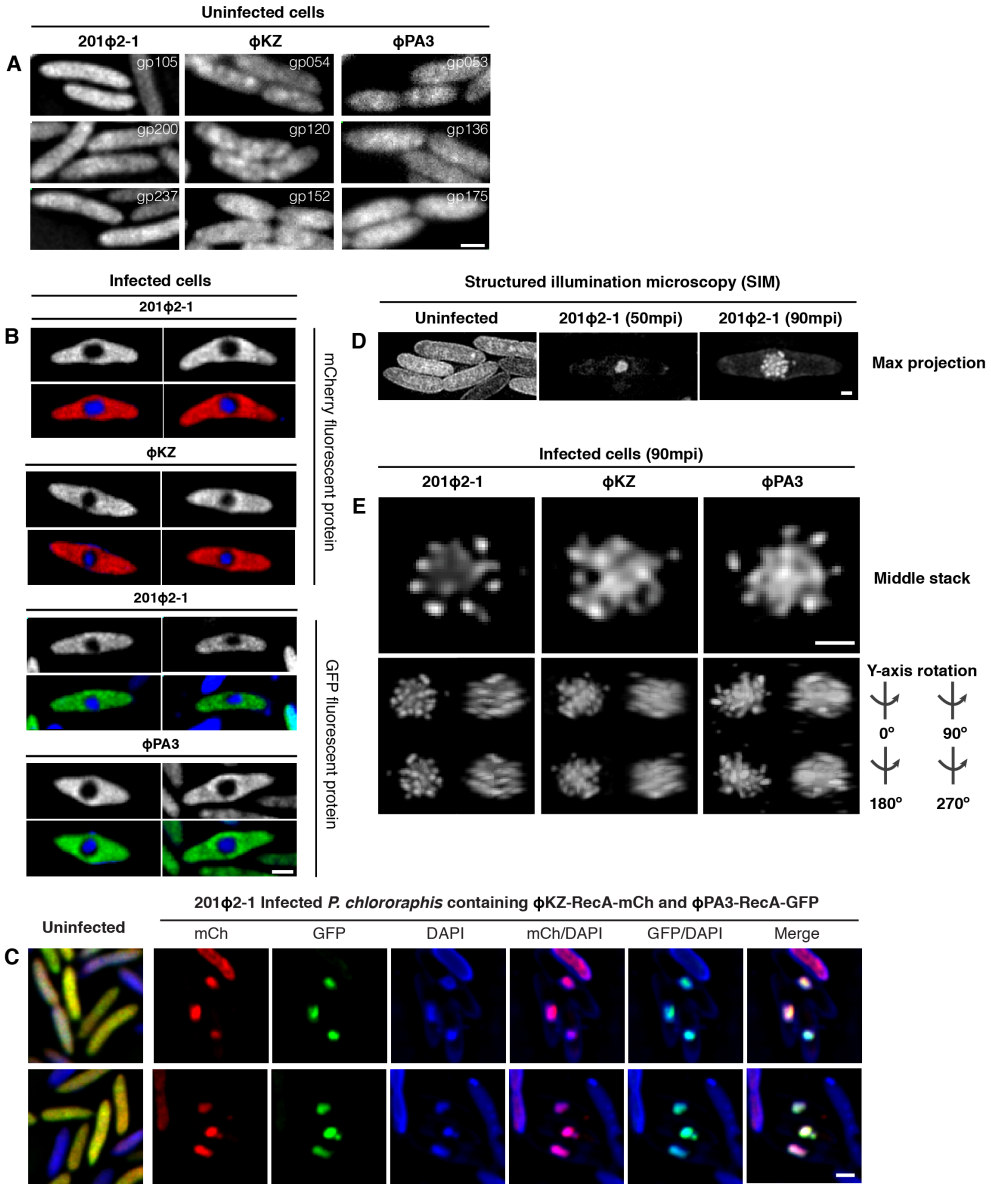

Figure S1: (A) The compartment homologs (gp105 of 201Φ2-1, gp054 of ΦKZ, and gp053 of ΦPA3), major capsid homologs (gp200 of 201Φ2-1, gp120 of ΦKZ, and gp136 of ΦPA3), and RecA-related proteins (gp237 of 201Φ2-1, gp152 of ΦKZ, and gp175 of ΦPA3) do not assemble any specific structure in

the absence of phage infection. The cells were grown on agarose pads and were induced by arabinose to express fluorescent protein fusions. Cover slips were put on right before the microcopy and images were then collected. Scale bar equals 1 micron. Arabinose concentrations are indicated in the related Figure 1. **(B)** The fluorescent proteins (GFP and mCherry) are excluded from the phage nucleus during the phage infection. The cells were grown on agarose pads and were induced by arabinose to express fluorescent proteins. High titer phage lysates were added to infect their corresponding hosts (*P. chlororaphis and P. aeruginosa*). Cover slips were put on the pad before microcopy and images were then collected at 60 mpi. Phage nucleoid is stained blue by DAPI. Scale bar equals 1 micron. Arabinose concentrations are indicated in the related Figure 1. **(C)** Fluorescence images showing co-localization of ΦKZ-gp152-mCherry (red) and ΦPA3-gp175-GFP (green) in the 201Φ2-1 nucleus (stained blue by DAPI). Examples of uninfected cells are shown. The *P. chlororaphis* cells were grown on an agarose pad for 3 hours at 30°C and were induced by 0.1% arabinose. In the absence of infection, ΦKZ-gp152-mCherry (red) and ΦPA3-gp175-GFP (green) are uniformly distributed. Upon infection at 60 mpi, both ΦKZ-gp152-mCherry (Red) and ΦPA3-gp175-GFP (Green) localize together with 201Φ2-1 DNA (blue). Scale bar equals 1 micron. **(D-E)** Structured illumination microscopy (SIM) images showing the maximum projection of cells from uninfected and infected *P. chlororaphis* cells at 50 and 90 mpi. **(E)** SIM images of *P. chlororaphis* and *P. aeruginosa* infected with corresponding phages (201Φ2-1, ΦKZ, and ΦPA3) at 90 mpi. Degree of rotation of the phage nucleus around Y-axis is indicated on the right for each subset. The *Pseudomonas* cells were grown on an agarose pad and the infection was started when the high-titer phage lysates were added. At the indicated time point, the cells were fixed and DNA was stained by DAPI (gray). Scale bar equals 0.5 micron. Related to Figure 1.

Figure S2 *[Related to Figure 2]*

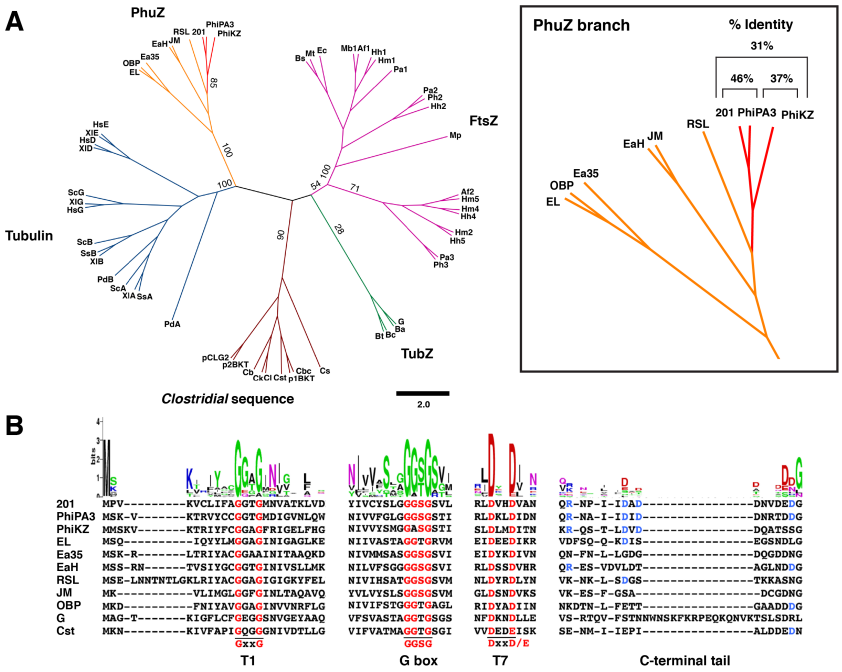

Figure S2: The PhuZ proteins from 201Φ2-1, ΦKZ, and ΦPA3 show relatively high conservation in essential domains. Related to Figure 2.

A) Phylogenetic tree showing the relationships between major families of eukaryotic tubulin and prokaryotic tubulin-like proteins (PhuZ, FtsZ, TubZ, and *Clostridial* proteins). Selected bootstrap values are shown at major points. Amino acid identity of $PhuZ_{201}$, $PhuZ_{\Phi KZ}$ and $PhuZ_{\Phi PA3}$ is shown in the inset.

B) Sequence alignment of conserved tubulin domains across the bacteriophage tubulins showing conserved residues of the T1 loop, signature motif (G box), and the T7 catalytic loop which is involved in GTP hydrolysis. The C-terminal tail shows high divergence among phage tubulins, but arginine and aspartic residues in this domain are most conserved in 201Φ2-1, ΦKZ, and ΦPA3 (shown in blue).

Figure S3 *[Related to Figures 2 and 3]*

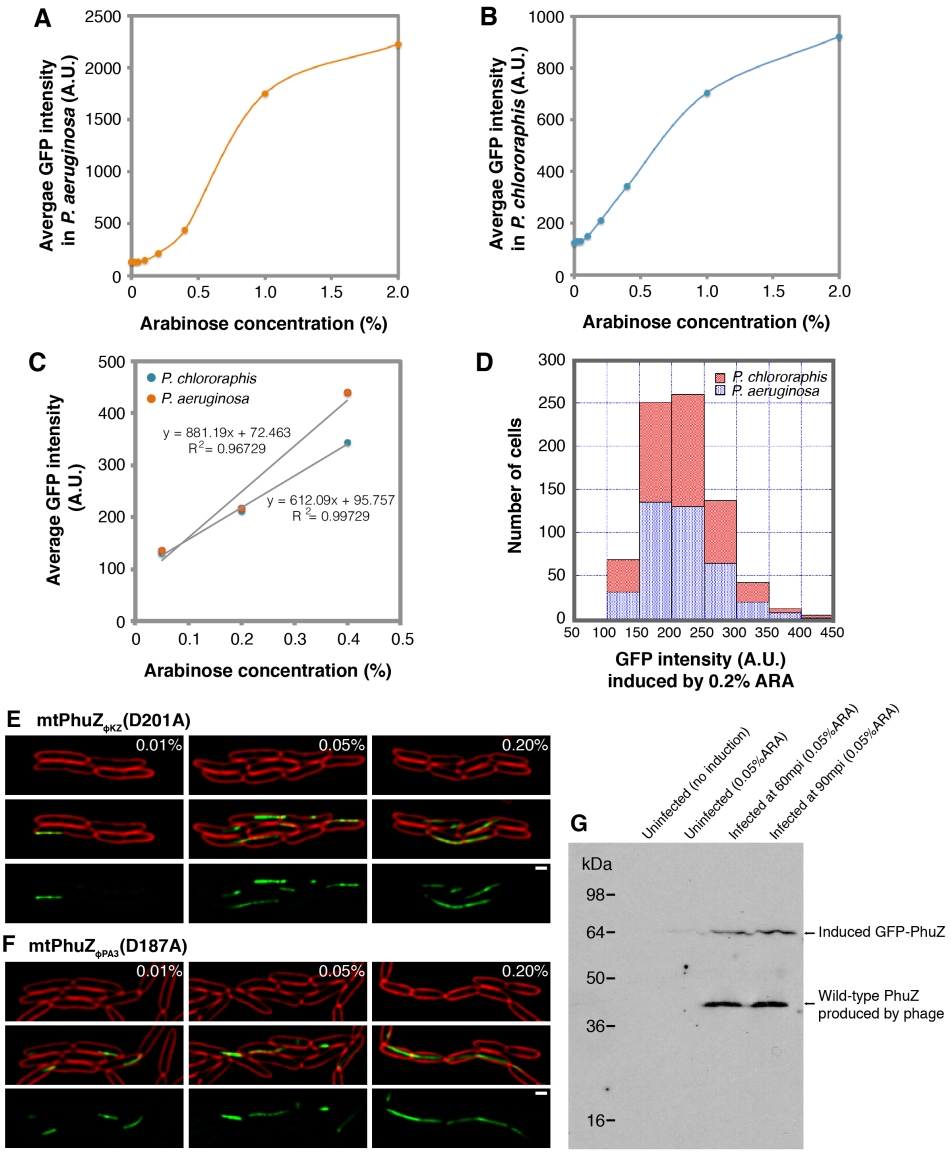

Figure S3: (A-D) Line graphs presenting average intensity of GFP induced at various concentrations of arabinose from the arabinose promoter in pHERD30T in *P. aeruginosa* **(A)** and *P. chlororaphis* **(B)**. The

average intensity of GFP expressed in the *P. aeruginosa* and *P. chlororaphis* cells linearly increased (R^2 close to 0.99) in the range of 0.05% to 0.4% arabinose **(C)**, and the proteins are uniformly expressed throughout the cell population, with less than a 2 fold variation from the mean for 99% of cells in the population **(D)**. Data represented as mean were collected from the induced cells at indicated arabinose concentration from at least 3 different fields with at least 100 cells per field. Related to Figure 2. **(E-F)** Additional fluorescence data on the second GTPase mutant GFP-$PhuZ_{\Phi KZ}$D201A **(E)** and GFP-$PhuZ_{\Phi PA3}$D187A **(F)**. Cells were grown on agarose pads and the fusion proteins were induced at the indicated arabinose concentrations. Cell membranes were stained red by FM 4-64. All scale bars equal 1 micron. Related to Figure 2. **(G)** Western blot analysis of total $PhuZ_{\Phi PA3}$ in *P. aeruginosa* cells. The *P. aeruginosa* cells containing GFP-$PhuZ_{\Phi PA3}$ under an arabinose promoter in pHERD30T were grown on agarose pads in 60 mm-petri dishes supplemented with either 0.2% glucose for the no induction control or 0.05% arabinose for induction and the cells were harvested at 4 hours. For the infected cells, a high-titer lysate of phage ΦPA3 was added to the cells and they were later collected at 60 and 90 mpi. SDS-PAGE and western blotting were carried out and both GFP-PhuZ and untagged PhuZ were detected using anti-$PhuZ_{201}$ antibodies, which cross-react with $PhuZ_{\Phi PA3}$. GFP-$PhuZ_{\Phi PA3}$ induced from a plasmid with 0.05% was expressed at lower levels than the wild-type protein and represents less than 1/3 of the total PhuZ protein produced. GFP-PhuZ expressed from the plasmid was detected at higher levels in cells infected with phage than in uninfected cells. Related to Figure 3.

Figure S4 *[Related to Figure 3]*

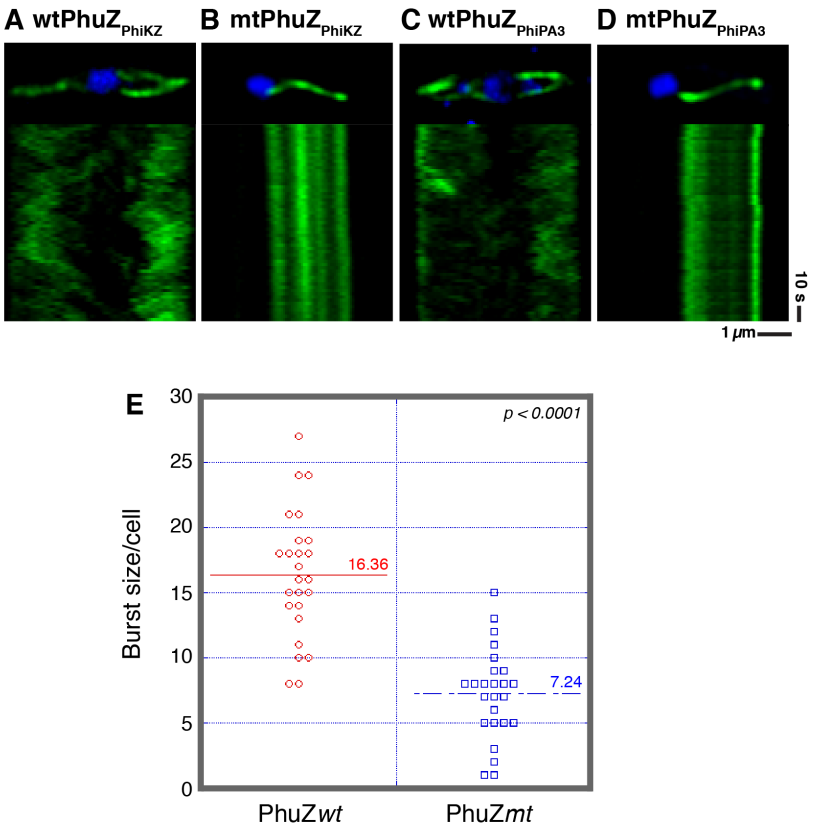

Figure S4: (A-D) Kymographs showing dynamically unstable filaments of wild-type GFP-PhuZ$_{\Phi KZ}$ **(A)** and wild-type GFP-PhuZ$_{\Phi PA3}$ **(C)** and completely static filaments of mutant GFP-PhuZ$_{\Phi KZ}$ **(B)** and mutant GFP-PhuZ$_{\Phi PA3}$ **(D)**. The kymographs from time-lapse microscopy in which images were collected every 2 seconds are plotted showing the GFP fluorescence intensity of the filaments (as imaged in the top row) for a total of 2 minutes. The phage nucleus was stained by DAPI (blue). **(E)** Phage burst size analysis from a single-cell infection assay (Kraemer, *et.al.* 2012). As reported in Kraemer, JA. et al., 2012, the graph shows that the average number of phage particles produced by the cells expressing wild-type PhuZ was 16.36 phage per cell (n=25), which was significantly higher *($p < 0.0001$)* than the average burst size of 7.24 of cells expressing mutant PhuZ (n = 25). Related to Figure 3.

Table S1: List of plasmids and strains used in this study. Related to Experimental procedures

Insert	Backbone	Host	*Plasmid*	*Strain*
GFP-201-PhuZ (gp059)	pHERD30T	PC	pME028	ME041
GFP-ΦKZ-PhuZ (gp039)	pHERD30T	PA01	pVC029	VC072
GFP-ΦPA3-PhuZ (gp028)	pHERD30T	PA01	pME056	ME090
GFP-ΦKZ-PhuZ (gp039) -D201A	pHERD30T	PA01	pVC033	VC242
GFP-ΦKZ-PhuZ (gp039) -D204A	pHERD30T	PA01	pVC034	VC243
GFP-ΦPA3-PhuZ (gp028) -D187A	pHERD30T	PA01	pVC031	VC245
GFP-ΦPA3-PhuZ (gp028) -D190A	pHERD30T	PA01	pVC032	VC247
GFP-201-compartment (gp105)	pHERD30T	PC	pJC001	JC002
mCh-ΦKZ-compartment (gp054)	pHERD30T	PA01	pMAC011	MAC023
GFP-ΦPA3-compartment (gp053)	pHERD30T	PA01	pVC077	VC414
201-major capsid-GFP (gp200)	pHERD30T	PC	pVC007	VC125
ΦKZ-major capsid-mCh (gp120)	pHERD30T	PA01	pMAC039	MAC043
ΦPA3-major capsid-GFP (gp136)	pHERD30T	PA01	pVC087	VC417
201-RecA-GFP (gp237)	pHERD30T	PC	pVC008	VC127
ΦKZ-RecA-mCh (gp152)	pHERD30T	PA01	pMAC016	MAC021
ΦPA3-RecA-GFP (gp175)	pHERD30T	PA01	pVC089	VC421
ΦPA3-RecA-GFP-ΦKZ-RecA-mCh	pHERD30T	PC	pMAC032	MAC036

SUPPLEMENTAL EXPERIMENTAL PROCEDURES

Plasmid Constructions and Bacterial Transformation

The stop codons at the end of the *gfp* were deleted from pME27 (Kraemer et al., 2012) and this new plasmid, pME54, was used to clone in the *phuZ* genes from the two different *P. aeruginosa* phages. ΦKZ *gp39* was amplified from the phage ΦKZ genome and ΦPA3 *gp28* was amplified from the phage ΦPA3 genome. Each PCR products (*gp28* and *gp39*) and pME54 were digested with HindIII and ligated together. The phage genes encoding the compartment protein (*gp105* from 201Φ2-1, *gp054* from ΦKZ, and *gp053* from ΦPA3), major capsid protein (*gp200* from 201Φ2-1, *gp120* from ΦKZ, and *gp136* from ΦPA3), and RecA-like protein (*gp237* from 201Φ2-1, *gp152* from ΦKZ, and *gp175* from ΦPA3) were PCR-amplified from high-titer phage lysates and were constructed into pHERD30T containing either GFP or mCherry fluorescent proteins by Gibson Assembly® (New England Biolabs), as previously described in Chaikeeratisak et al., 2017.

These resulting recombinant plasmids were transformed into *E.coli* DH5A plated on selective media. DNA sequencing was conducted to confirm the correctness of constructs and they were later electroporated into *Pseudomonas* competent cells (*P. chlororaphis* strain 200-B and *P. aeruginosa* strain PA01) to create strains, as listed in Supplemental table 1. All bacterial cultures were grown at 30°C.

Sequence Analysis and Phylogenetic Tree Construction

The PhuZ sequence from bacteriophage 201Φ2-1 (*GenBank: YP_001956784.1*) was used to initiate an iterative blast search against NCBI database. All obtained protein sequences were aligned using TCoffee and ClustalW, and the phylogenetic tree was constructed using Molecular Evolutionary Genetics Analysis (MEGA) version 5.2.2., as described by Tamura, K. et al., 2013. A bootstrap consensus tree of 100 trees is shown in Figure S2A with the selected bootstrap numbers on selected branches. Similar grouping of Phage tubulin/FtsZ (PhuZ) was obtained regardless of the alignment methods used.

The tree includes the following sequences indicated by their initial names with accession numbers: 201 (*GenBank: YP_001956784.1*); ΦPA3 (*GenBank: AEH03455.1*); ΦKZ (*GenBank: NP_803605.1*); EL (*GenBank: YP_418049.1*); Ea35 (*GenBank: YP_009005002.1*); EaH (*GenBank: YP_009010087.1*); RSL (*GenBank: BAQ02539.1*); JM (*GenBank: YP_006383382.1*); OBP (*GenBank: YP_004957954.1*); G (*GenBank: YP_009015441.1*); Ba (*GenBank: NP_052741*); Bc (*GenBank: ZP_00236418*); Bt (*GenBank: CAD30186*); Cs (*GenBank: YP_003936284.1*); Cbc (*GenBank: EDS76598.1*); Cst (*GenBank: YP_398619.1*); Cl (*GenBank: YP_003845715.1*); Ck (*GenBank: YP_001393972.1*); Cb (*GenBank: EDT76720.1*); p1BKT (*GenBank: YP_004385787.1*); p2BKT (*GenBank: YP_004397219.1*); pCLG2 (*GenBank: YP_003034138.1*); Ec (*GenBank: NP_308126*); Bs (*GenBank: NP_389412*); Mt (*GenBank: NP_216666*); Mp (*GenBank: P75464*); Af1 (*GenBank: NP_069371*); Af2 (*GenBank: NP_070043*); Pa1 (*GenBank: Q9V2S0*); Pa2 (*GenBank: Q9UZ61*); Pa3 (*GenBank: NP_126497*); Ph2 (*GenBank: O58491*); Ph3 (*GenBank: O59060*); Mb1 (*GenBank: ZP_00562770*); Hh1 (*GenBank: NP_279457*); Hh2 (*GenBank: NP_279324*); Hh4 (*GenBank: NP_279378*); Hh5 (*GenBank: NP_395771*); Hm1 (*GenBank: YP_135405*); Hm2 (*GenBank: YP_138195*); Hm4 (*GenBank: AAV48016*); Hm5 (*GenBank: YP_137684*); ScA (*GenBank: NP_013625*); ScB (*GenBank: NP_116616*); ScG (*GenBank: NP_013313*); SsA (*GenBank: P02550*); SsB (*GenBank: P02554*); PdA (*GenBank: AAO12155*); PdB (*GenBank: AAO12159*); XlA (*GenBank: P08537*); XlB (*GenBank: AAA49977*); XlD (*GenBank: AAL27450*); XlE (*GenBank: AAN77278*); XlG (*GenBank: AAA49720*); HsD (*GenBank: Q9UJT1*); HsE (*GenBank: Q9UJT0*); HsG (*GenBank: NP_001061*).

Amino acid sequence analysis of FtsZ-like protein sequences of bacteriophage was further performed in order to investigate tubulin-conserved domains; T1 loop, G box, T7 loop and C-terminal domain. The sequence conservation and relative frequency of each amino acid were represented on the top of the sequence alignment in Figure S2B by WebLogo as described by Crooks, GE. et al., 2004.

SUPPLEMENTAL REFERENCES

Tamura, K., Stecher, G., Peterson, D., Filipski, A., and Kumar, S. (2013). MEGA6: Molecular Evolutionary Genetics Analysis Version 6.0. Molecular Biology and Evolution *30*, 2725–2729.
Crooks, G.E., Hon, G., Chandonia, J.-M., and Brenner, S.E. (2004). WebLogo: A Sequence Logo Generator. Genome Research *14*, 1188–1190.

Acknowledgements

Chapter 3, in full, is a reprint of the material as it appears in the August 15, 2017 edition of *Cell Reports*. Chaikeeratisak, V., Nguyen, K., Egan, M., Erb, M.L., Vavilina, A., Pogliano, J (2017). The Phage Nucleus and Tubulin Spindle Are Conserved among Large *Pseudomonas* Phages. *Cell Reports*, Volume 20, Issue 7, 1563 – 1571. The dissertation author was a significant contributor to this paper.

Chapter 4: Viral Capsid Trafficking along Treadmilling Tubulin Filaments in Bacteria

Authors

Vorrapon Chaikeeratisak[1,2], Kanika Khanna[1], Katrina T. Nguyen[1], Joseph Sugie[1], MacKennon E. Egan[1], Marcella L. Erb[1], Anastasia Vavilina[1], Poochit Nonejuie[3], Eliza Nieweglowska[4], Kit Pogliano[1], David A. Agard[4], Elizabeth Villa[1], Joe Pogliano[1*]

Affiliations

[1]Division of Biological Sciences, University of California, San Diego, CA 92093, USA

[2]Department of Biochemistry, Faculty of Science, Chulalongkorn University, Bangkok, 10330, Thailand.

[3]Institute of Molecular Biosciences, Mahidol University, Nakhon Pathom 73170, Thailand.

[4]Department of Biochemistry and Biophysics and the Howard Hughes Medical Institute, University of California, San Francisco, CA 94158 USA

Summary

Cargo trafficking along microtubules is exploited by eukaryotic viruses, but no such examples have been reported in bacteria. Several large *Pseudomonas* phages assemble a dynamic, tubulin based (PhuZ) spindle that centers replicating phage DNA sequestered within a nucleus-like structure. Here we show that capsids assemble on the membrane and then move rapidly along PhuZ filaments toward the phage nucleus for DNA packaging. The spindle rotates the phage nucleus, distributing capsids around its surface. PhuZ filaments treadmill toward the nucleus at a constant rate similar to the rate of capsid movement and the linear velocity of nucleus rotation. Capsids become trapped along mutant static PhuZ filaments that are defective in GTP hydrolysis. Our results suggest a transport and distribution mechanism in which capsids attached to the sides of filaments are trafficked to the nucleus by PhuZ polymerization at the poles, demonstrating that the phage cytoskeleton evolved cargo trafficking capabilities in bacteria.

One Sentence Summary

Upon infection of *Pseudomonas*, capsids of giant bacteriophages traffic from the site of assembly on the host membrane along a treadmilling tubulin-based spindle to reach replicating phage DNA contained within a nucleus-like structure.

Introduction

Microtubules play a key role in intracellular cargo trafficking in eukaryotes. Many viruses exploit microtubule trafficking to translocate from the surface of the plasma cell membrane to the cell interior, such as to the nucleus to initiate viral replication [63-66]. Newly assembled viral particles also traffic along microtubules to reach the surface of the cell for egress [54, 64]. In addition to serving as a conduit for movement of mature particles in and out of cells, microtubules have been shown to be important for other steps of viral replication, including providing transportation for capsids [65, 67] or viral RNA/protein complexes [68] or by contributing to efficient capsid formation [69]. In contrast to eukaryotes, cargo trafficking along tubulin filaments has not been reported in bacteria.

We recently described a family of *Pseudomonas* phages that assemble a bipolar spindle composed of a tubulin-like protein (PhuZ) [31, 41, 61]. PhuZ is expressed by phage 201Φ2-1 early during infection of *P. chlororaphis* where it forms three-stranded filaments [31, 41, 61, 70] that spatially organize viral replication. Like eukaryotic microtubules, PhuZ filaments are polarized, with kinetically distinct plus and minus ends. PhuZ polymers display dynamic instability *in vitro* and *in vivo*, that is, filaments can cease growing at their plus ends, catastrophically depolymerize and then be rescued to start growing again [31, 61]. Notably, a different behavior, treadmilling, in which polymerization at the plus end of the filament is matched by depolymerization at the minus end, has been observed with *in vitro* assembled PhuZ polymers, but it has remained unclear if filaments of the spindle can also treadmill *in vivo.*

The PhuZ spindle plays a key role in phage reproduction by positioning replicating phage DNA in the center of the cell [31, 61]. Phage 201Φ2-1 DNA is encased by a proteinaceous shell composed of gp105, forming a nucleus-like structure, referred to as the phage nucleus, that compartmentalizes proteins according to function [71]. Early during infection, the dynamically unstable filaments of the PhuZ spindle push the nucleus from the cell pole to the midcell where it then oscillates in position [71]. Proteins involved in DNA replication and transcription localize inside the phage nucleus while ribosomes and proteins involved in metabolic processes localize in the cytoplasm on the outside [71]. The nucleus likely provides protection for phage DNA by excluding proteins of the host defense systems (restriction systems, nucleases, and CRISPR-Cas) that target invading phage DNA [62, 71, 72]. The phage spindle and nucleus are conserved among the related large phages ΦPA3 and ΦKZ that replicate in *Pseudomonas aeruginosa* [62, 73].

Curiously, phage capsids assemble on the plasma membrane but must dock on the surface of the phage nucleus in order to package phage DNA [62, 71]. How capsids relocate from the membrane to the surface of the phage nucleus was unclear and potentially explained by three models (Figure 1A): 1) via “random diffusion” through the cell until capsids make contact with the nuclear shell, 2) via “DNA spooling”, in which strands of phage DNA emanating from the phage nucleus are captured by the packaging ATPase at the base of the capsid and the process of spooling DNA into the capsid transports them to the shell surface, or 3) via “capsid trafficking” in which the PhuZ spindle plays a role in transporting capsids to the phage nucleus.

Here we explore the mechanisms underlying capsid movement during phage infection. Using time-lapse microscopy and cryo-electron tomography (CET), we show that capsids move rapidly and directionally along PhuZ filaments but become trapped along mutant PhuZ filaments that are defective in GTP hydrolysis. Photobleaching studies demonstrate that filaments of the spindle treadmill toward the nucleus, providing a simple mechanism by which capsids might be transported.

Results

Capsids move directionally along PhuZ filaments

To investigate models for capsid movement, we used rapid time-lapse imaging of GFP-tagged capsids and followed their movement from the cell membrane to the phage nuclear shell. We first identified the stage of infection during which capsids relocate by using DAPI staining and super resolution fluorescence microscopy to determine approximately when DNA packaging occurs. DAPI staining of *P. chlororaphis* cells infected with phage 201Φ2-1 showed that nuclear staining intensity increased as DNA replicated until 50 minutes post infection (mpi) and that viral particles containing packaged DNA accumulated around the phage nucleus at 60 mpi (Figure 1B and S1). We therefore used time-lapse imaging to study capsid trafficking between 40 and 60 mpi by simultaneously imaging fluorescently labeled capsids (gp200) and shells (gp105). *P. chlororaphis* cells expressing gp200-GFP and mCherry-gp105 were infected with phage 201Φ2-1 and, at approximately 45 mpi when capsid assembly occurs, cells were imaged every 2 seconds for 2 minutes. In Figure 1C, multiple capsids (green foci) were observed to assemble on the cell membrane, where they remained motionless for several seconds

(Movie S1) [71]. Capsids then independently followed a linear trajectory, seemingly traveling on the same intracellular track directly to the phage nucleus where they docked (Figure 1C, Movie S1). Movement was directional and rapid, with capsids traveling over 1 micron in length in less than 30 seconds. These results suggest that capsids move via either model 2 (DNA spooling) or model 3 (capsid trafficking) (Figure 1A). We obtained similar results with phage ΦPA3 infecting *P. aeruginosa.* Rapid time-lapse imaging of GFP-tagged PA3-capsids (gp136) and mCherry-tagged PA3-shell (gp053) showed that the trajectory of the capsids was a straight line moving rapidly toward midcell (Figure S2A, Movie S2).

To determine if the PhuZ spindle is involved in capsid movement, we imaged GFP-tagged capsids with either mCherry-tagged wildtype PhuZ or a PhuZD190A mutant that blocks GTP hydrolysis. We infected *P. chlororaphis* cells expressing gp200 (capsid)-GFP and either wild type mCherry-PhuZ or mutant mCherry-PhuZD190A and visualized capsid assembly and movement in time-lapse microscopy beginning at 45 mpi. Our capsid/PhuZ co-localization experiments demonstrated that as capsids traveled through the cell toward the phage nucleus, they co-localized with PhuZ polymers and appeared to travel on the same path along the PhuZ filaments in both time-lapse (Figure 1D, Movie S3) and still images (Figure 1E, left panel). By 50 mpi, most capsids were docked on the phage nucleus (Figure 1E, right panel). Capsids co-localized with another protein involved in capsid assembly (internal core protein gp246), suggesting that the capsids that dock on the surface of the phage nucleus are fully assembled (Figure 1F).

PhuZ mutants defective in GTP hydrolysis block capsid migration and rotation of the phage nucleus

In *P. chlororaphis* cells expressing the mutant mCherry-PhuZD190A, phage 201Φ2-1 capsids lined the filaments at both 50 mpi and 70 mpi (Figure 2A, arrows). In time-lapse microscopy, the capsids appeared to be immobilized on the sides of the PhuZ filaments (Figure 2C, S4A and Movie S4). Similar results were found for closely related phage ΦPA3 which replicates in *P. aeruginosa* by a similar mechanism [71]. ΦPA3 capsids individually travelled along similar trajectories (Figure S2A, Movie S2) and co-localized with and migrated along wild type PhuZ filaments (Figure S2B, Movie S5). In the presence of catalytically defective PhuZD190A, ΦPA3 capsids became statically attached to filaments (Figure 2B, 2D, S3, S4B, and Movie S6).

DAPI staining was used as a way to assess, independently of GFP fusions, if the expression of the PhuZD190A mutant interfered with capsid trafficking, which is required for DNA packaging at the phage nucleus. As previously reported [62, 71], capsids containing DNA accumulated on the phage nucleus by 60 mpi (Figure 1B). However, in the presence of PhuZD190A, the number of encapsidated phage particles decreased approximately five-fold (from an average of 10.5 to 2.1 particles), suggesting that capsid DNA packaging is delayed (Figure 2G and 2H). Taken together, our results suggest that capsids rely upon the PhuZ spindle to migrate rapidly to the phage nucleus and the GTP hydrolysis mutations in PhuZ trap capsids along static filaments and therefore delay DNA packaging.

To further confirm the difference in capsid positioning between cells expressing the wild type or PhuZD190A mutant at 50 mpi, we quantitated gp200 (capsid)-GFP position from 32 infected cells. We plotted capsid position versus normalized cell length and found that the distribution of capsids is biased toward the midcell near the nucleus in cells expressing wild type PhuZ, with approximately 63% of capsids occurring within 30% of the cell midpoint (Figure 2E and 2F). However, in the presence of the PhuZD190A mutant, the capsids are more evenly distributed throughout the cell (Figure 2E and 2F). The effect of the PhuZD190A catalytic mutation on capsid distribution is consistent with the PhuZ spindle playing a role in capsid migration.

We then used cryo-focused ion beam milling (cryo-FIB) coupled with cryo-electron tomography (cryo-ET) to visualize capsids associated with filaments at high resolution in a near-native state [71]. Since capsids only transiently interacted with filaments as they translocated to the phage nucleus in wild type cells, we performed cryo-FIB-ET on cells expressing PhuZD190A mutants in which capsids appeared to become trapped. In samples of *P. aeruginosa* cells expressing mutant PhuZD190A and infected with phage ΦPA3 for 70 minutes, 18 empty capsids (green) were clustered around PhuZ filaments (light blue) in a ~200 nm slice of the sample (Figure 3A, 3B, and S5A). At this time point, capsids are normally filled with DNA in wildtype cells (Figure S5B), yet these capsids are empty, suggesting that capsids associated with the mutant PhuZ filaments are unable to traffic to the nucleus for DNA packaging, in agreement with fluorescence microscopy data (Figure 2G). Since capsids appear in close proximity (3 to 4 nm) to the filament (Figure 3C-3H), we attempted to identify amino acids that are conserved on the outer surface of

PhuZ filaments that might possibly serve as a point of attachment. Three aspartic acid residues (D235, D259, D263) that are conserved among PhuZ proteins encoded by PA3, PhiKZ, and 201 were mutated to alanine (S13C). One of them, D235A, completely blocked filament assembly (data not shown). The mutants D259A and D263A retained their ability to assemble filaments while the double mutant, D259A-D263A, appeared slightly impaired in filament formation. We examined the ability of capsids to traffic along all three of these mutant filaments using time-lapse microscopy (Figure S13B). We also examined DNA packaging into capsids (a hallmark of successful trafficking) and nucleus rotation in the three mutants (Figure S13A). In each case, capsids were still able to move along the mutant filaments, mature capsids filled with DNA were observed, and the phage nucleus rotated at midcell. Attempts to detect a direct interaction between PhuZ and capsid proteins using yeast two hybrid systems also yielded a negative result (Figure S6).

During phage 201Φ2-1 infection, the phage nucleus is pushed from the cell pole to the cell midpoint where, at approximately 40-45 mpi, it suddenly begins to rotate in position [71] (Figure 4A, S7A and Movie S7). Figure 4A and Movie S7 show an example of a phage nucleus (green) being pushed transversely by the PhuZ spindle (red) and undergoing approximately 2 revolutions within 60 seconds, with an average linear velocity of 43.6 +/-7.6 nm/s (n=10). In contrast, phage nuclei formed in the presence of mutant PhuZD190A are both mispositioned and do not rotate (Figure 4B, S7B and Movie S8). At 45 mpi, 46% (n = 611) of the wild type nuclei underwent rotations in the presence of wild type filaments, while in the presence of the PhuZD190A mutant, less than 6% (n = 286) rotated (Figure 4D). The sudden onset of phage nucleus rotation, which occurs at

approximately the same time as capsid movement begins, suggests a switch in the dynamics of the PhuZ spindle from primarily centering the phage nucleus to rotating it.

Rotation is dependent upon the dynamic GTPase activity of the PhuZ spindle, raising the question of what role rotation might play in phage reproduction. In our time-lapse co-localization experiments, capsids trafficked along the spindle and docked on the rotating shell (Figure 4C and Movie S9). The process of rotation appears to distribute capsids widely around the nuclear shell. We obtained identical results with phage ΦPA3 in *P. aeruginosa*: capsids traveled along PhuZ filaments and docked on the rotating phage nucleus where they then rotated together (Figure S8A, S8B, Movie S10, and S11), showing that this mechanism is conserved among this family of large *Pseudomonas* phages.

GTP-dependent treadmilling of PhuZ filaments is responsible for capsid movement and rotation of the phage nucleus

The mechanism underlying capsid movement along filaments was unclear. In eukaryotic cells, cargo trafficking along microtubules is typically dependent upon motor proteins such as kinesin and dynein that use ATP hydrolysis to drive unidirectional transport. However, phage and bacteria are generally thought to lack such motor proteins. Therefore, we explored the possibility that capsid movement is driven by filament treadmilling. In this model, insertion of new subunits occurs at one end of the filaments located near the cell poles, thereby driving capsids attached to the sides of the filaments toward midcell. To determine if spindle filaments treadmill, we used photobleaching to mark one end of the spindle after approximately 45 to 50 mpi when

capsids are migrating to the nucleus. As shown in Figure 5A and 5B, bleached zones (arrows) near the ends of the spindles moved rapidly toward the nucleus (Movies S12 and S13). The median rate of bleached zone movement through the cell was 51.5 nm/sec (n=40; Figure 5C and 5E), suggesting that filaments treadmill at a constant rate with no evidence of significant pausing even when taking images more frequently (Figure S11) or expanding the length of the cells with antibiotics to increase the distance of travel (Figure 5C). In all cases, regardless of filament length, bleached zones moved at a constant rate toward midcell. When both sides of a bipolar spindle were bleached, the two bleached zones migrated in unison toward the cell center with similar rates, arriving at the nucleus at the same time (Figure 5B, Movie S13). Quantitation of the rate of capsid migration towards the nucleus revealed that they move with a median rate of 50.3 nm/sec (n=10; Figure 5D and 5E), very similar to the rate of treadmilling (51.5 nm/sec, n=40). In the presence of the PhuZD190A mutant, the average rates of filament treadmilling and capsid migration both fall to near zero (Figure 5E, Figure S9, Movie S14). These results suggest that filaments of the spindle require GTP hydrolysis to treadmill and transport capsids toward the nucleus (Figure 5F), providing a potential mechanism for capsid migration driven by net filament growth near the poles and net loss near the nucleus. Nucleus rotation also occurred at a similar rate and was dependent upon PhuZ GTP hydrolysis, suggesting that treadmilling is responsible for both capsid movement and rotation, thereby temporally coupling these two processes.

Discussion

Our results suggest a model in which capsids assemble on the host cell membrane and migrate along filaments of the PhuZ spindle to reach the phage nucleus (Figure 6). Delivering capsids directly to the surface of the shell increases the rate at which these large phage particles dock and begin the process of DNA encapsidation. Rotation of the nucleus by the spindle likely serves to distribute the capsids more evenly around the shell surface maximizing efficient DNA packaging (Figure 6E). These phage genomes are 316KB (phage 201Φ2-1) and 309KB (phage ΦPA3) in size, and therefore occupy substantial space inside the phage nucleus. If two particles docked immediately adjacent to one another, only one might be able to package DNA. Capsid trafficking is driven by GTP dependent PhuZ polymerization and is conserved between phages 201Φ2-1 and ΦPA3, and likely other phages containing PhuZ homologs (Figure S12). PhuZ is conserved in a number of large phage genomes, including those that infect *Vibrio* and *Erwinia* (Figure S12). These results show that phages evolved a mechanism for trafficking cargo using a cytoskeletal element in bacteria.

Our results suggest a simple transport mechanism in which treadmilling filaments are responsible for rapid and directional capsid movement. Newly formed capsids release from the membrane, diffuse a short distance, and attach to the sides of filaments (Figure 6C-F). As new subunits are added to filament ends located at the cell poles, capsids are transported by the polymer to the phage nucleus. Capsids are released from filaments when they reach the depolymerizing ends adjacent to the nucleus, allowing them to dock on the phage nuclear surface (Figure 6E,F). This model is supported by our finding that

PhuZ subunits flux toward the nucleus at a rate almost identical to the rate of capsid movement.

Upon DNA injection and formation of the phage nucleus, spindle assembly begins when PhuZ monomers nucleate to form a hexameric structure to which additional monomers are added [41]. The filaments of the PhuZ spindle use dynamic instability to position and maintain the phage nucleus at midcell (Figure 6A,B) (Erb et. al., 2014; Kraemer et. al., 2012). We previously demonstrated that PhuZ filaments are intrinsically polar, with the plus end of the filament exhibiting rapid growth and dynamic instability *in vitro*. *In vivo* the minus end of the filament is localized to the cell pole and the dynamically unstable plus end is oriented toward midcell (Figure 6A,B). Later during phage replication, the behavior of the spindle changes from positioning the nucleus at midcell (Figure 6A,B) to rotating it in position concomitant with the transport of capsids (Figure 6C,D), suggesting developmental regulation of spindle dynamics. PhuZ filaments flux towards the phage nucleus, suggesting that, given the previous demonstration of polarity, the minus ends located at the cell poles are capable of constant growth. While filament minus ends can also grow, albeit at a higher critical concentration than the plus ends, what is unexpected here is that minus end growth and plus end dynamic instability would exist simultaneously. While the cellular concentration of PhuZ monomers are unknown, proteomics experiments show that the total amount of PhuZ protein increases as infection progresses (Figure S10), which could lead to altered filament dynamics over time. In isolated microtubules the higher tubulin concentrations needed for minus end growth would lead to rapid plus end growth and less frequent catastrophic collapse, although

both can occur simultaneously [74]. However, the *in vivo* situation here is far more complex, leading to several plausible explanations: 1) the effective concentration of PhuZ could be higher at the poles than the midcell; 2) resistance imposed by centering the nucleus could accelerate depolymerization at the midcell; 3) bundling of the filaments towards the poles could stabilize the minus ends and enhance the effective on-rate. Previous work suggested that there is a phage-encoded mechanism for anchoring PhuZ filaments at the poles [61] and this could facilitate adding new subunits, much as the microtubule associated protein XMAP215 does [75, 76]. *In vivo*, PhuZ filaments are clearly bundled along much of their length but splay near the midcell, becoming much harder to visualize [61]. *In vitro* studies have shown that non-dynamic PhuZ filaments are much more likely to bundle than their dynamic counterparts [31, 41, 61]. Thus, either the statistics of having many available minus ends, or a structure altered by bundling could also accelerate minus end addition. Given that the functions of the spindle change over time, it's not suprising that spindle behavior and dynamics are complex.

Microtubules also display different behaviors depending upon the specific cell type, buffer conditions or accessory factors. While minus ends grow at a slower rate and higher threshold concentration than the plus ends, the specific conditions can affect the two ends in different ways. This variability in conditions leads to the observation of dynamic instability [77-79] at both ends of a microtubule and treadmilling-like behavior [80-86]. In fact, microtubules have been observed to treadmill in both the minus to plus and plus to minus directions *in vitro* [82]. Similarly, our results show that PhuZ filaments are capable of displaying two distinct behaviors coupled to the spindle's biological functions: dynamic

instability, which is essential for centering the phage nucleus, and treadmilling, which is necessary for transporting phage capsids and rotating the nucleus. These two types of behaviors are consistent with our prior studies, further illuminate the central role of the PhuZ cytoskeleton in phage reproduction and highlight the plasticity of tubulins in assembling unique polymers tailored to performing specific cellular activities.

The nature of the proposed interaction between capsids and PhuZ polymers is unclear. In principle, capsids might associate with the sides of PhuZ filaments directly or indirectly via another protein. Precedence for capsids directly interacting with microtubules has been reported for several eukaryotic viruses. For example, the Hepatitis C virus interacts with tubulins, affects microtubule dynamics, and has been proposed to move through the cytoplasm by associating with dynamic microtubules [87]. Our results suggest a common solution to viral transport that occurs in evolutionarily divergent domains of life.

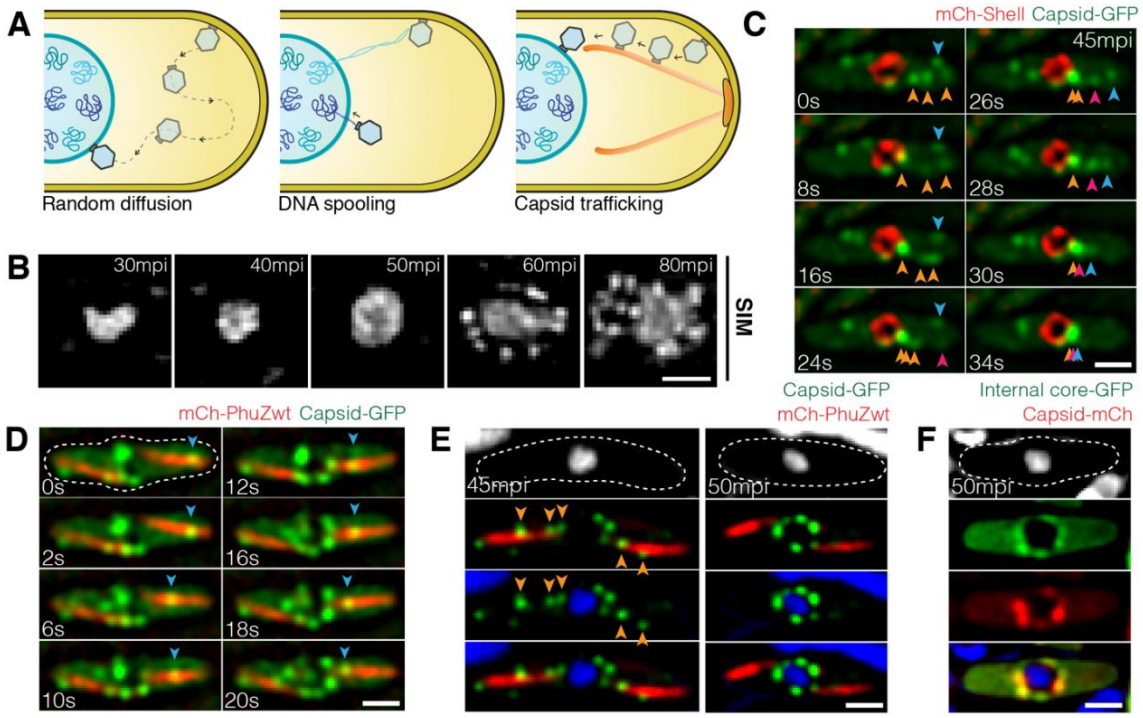

Figure 4.1: Phage capsids traffic along PhuZ filaments to the phage nucleus for DNA encapsidation by 60 minutes post infection (mpi). (A) Three possible models of capsid trajectory toward the phage nucleus. **(B)** 3D-SIM images showing appearance of the phage nucleus at various developmental stages of infected *P. chlororaphis* cells. The phage nucleus shows uniform staining in the first 50 min of infection. At 60 mpi, bright puncta appear surrounding the phage nucleus. Scale bars, 0.5 micron. **(C)** Rapid time-lapse imaging of GFP-tagged capsid (gp200; green) and mCherry-tagged shell (gp105; red) in *P. chlororaphis* infected with phage 201Φ2-1 over a 34 second interval. Capsids (green) assemble near the cell membrane and immediately after detachment they independently migrate along the same, straight line trajectory towards the phage shell (red). Arrows indicate individual capsids. **(D)** Rapid time-lapse imaging of GFP-tagged capsids (gp200; green) and mCherry-tagged wildtype PhuZ (gp059; red) during an interval of 20 seconds in phage 201Φ2-1 infected *P. chlororaphis* cells. Blue arrow indicates a capsid traveling along the PhuZ spindle from the cell pole to phage nucleus. **(E)** Still images of phage 201Φ2-1 infected *P. chlororaphis* cells expressing GFP-tagged capsid (gp200; green) and mCherry-tagged wildtype PhuZ (gp059; red) at 45 and 50 mpi. **(F)** Still images of phage 201Φ2-1 infected *P. chlororaphis* cells expressing GFP-tagged internal core protein (gp246; green) and mCherry-tagged capsid (gp200; red) at 50 mpi. Dashed lines indicate cell borders. Scale bars in c-f, 1 micron.

Figure 4.2: Phage capsids are trapped along mutant PhuZ spindles in both phage 201Φ2-1 and phage ΦPA3 resulting in reduced encapsidation. (A) Fluorescence images of *P. chlororaphis* expressing GFP-tagged 201-capsid (gp200; green) and catalytically defective mCherry-tagged 201-PhuZD190A (gp059; red) infected with phage 201Φ2-1 at 50 and 70 mpi. **(B)** Fluorescence images of *P. aeruginosa* expressing mCherry-tagged PA3-capsid (gp136; false color, green) and catalytically defective GFP-tagged PA3-PhuZD190A (gp028; false color, red) infected with phage ΦPA3 at 75 mpi. **(C)** Time-lapse imaging of *P. chlororaphis* expressing GFP-tagged 201-capsid (gp200; green) with mCherry-tagged 201-PhuZD190A (gp059; red) over an interval of 88 seconds **(D)** Time-lapse imaging of *P. aeruginosa* expressing mCherry-tagged PA3-capsid (gp136; false color, green) with GFP-tagged PA3-PhuZD190A (gp028; false color, red) over an interval of 299 seconds. **(E)** Distribution of GFP-tagged 201-capsids (gp200) in *P. chlororaphis* cells expressing either wild-type (left panel) or mutant (right panel) PhuZD190A infected with phage 201Φ2-1 at 50 mpi. Average Z-projection images (n=32) of GFP intensity are shown on the top panel and distribution plots of GFP intensity of individuals (n=32) are present on the bottom panel. **(F)** Graph showing percentage of detected GFP-tagged capsids in phage 201Φ2-1 infected *P. chlororaphis* cells expressing either wild-type (green) or mutant PhuZD190A (hatched bar) versus the fraction of cell length from the midcell to the cell pole. **(G)** 3D-SIM images of encapsidated phage particles in phage 201Φ2-1 infected *P. chlororaphis* cells expressing either wild-type (top panel) or mutant PhuZD190A at various time points (bottom panel). Arrows indicate positions of the phage nuclei. **(H)** Box plot showing the number of encapsidated phage particles counted in phage 201Φ2-1 infected *P. chlororaphis* cells expressing either wild-type (top plot) or mutant (bottom plot) PhuZ at 80 mpi. Asterisks indicate the average number of the encapsidated particles counted per strain. Dashed lines indicate the border of the cells. Scale bars, 1 micron.

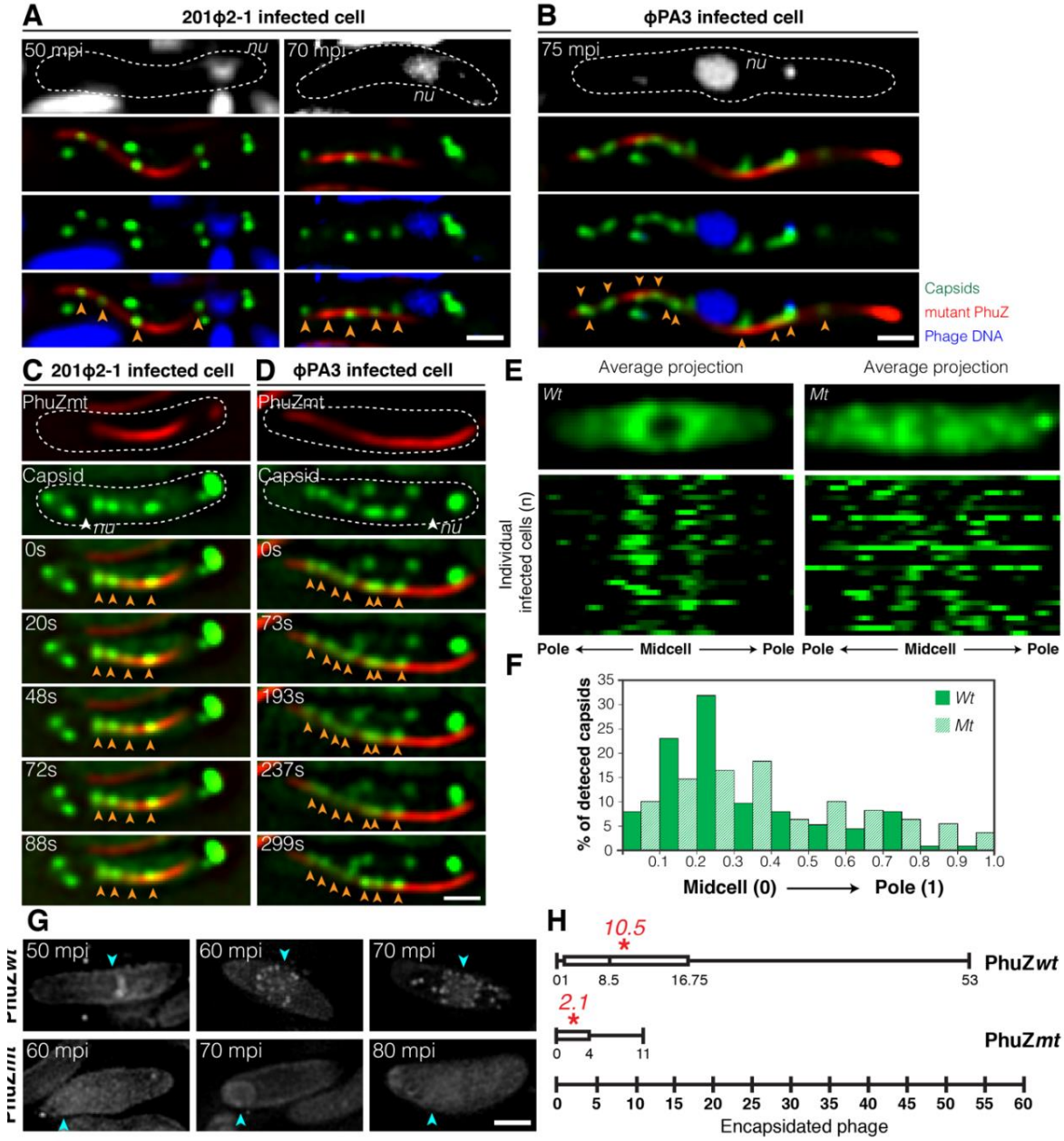
A
201ϕ2-1 infected cell
50 mpi
70 mpi
nu
B
ϕPA3 infected cell
75 mpi
Capsids
mutant PhuZ
Phage DNA
C 201ϕ2-1 infected cell
D ϕPA3 infected cell
PhuZmt
Capsid
0s
20s
48s
72s
88s
73s
193s
237s
299s
E
Average projection
Wt
Mt
Individual infected cells (n)
Pole ← Midcell → Pole
F
% of deteced capsids
Midcell (0) → Pole (1)
G
PhuZwt
PhuZmt
50 mpi
60 mpi
70 mpi
80 mpi
H
10.5
2.1
PhuZwt
PhuZmt
Encapsidated phage

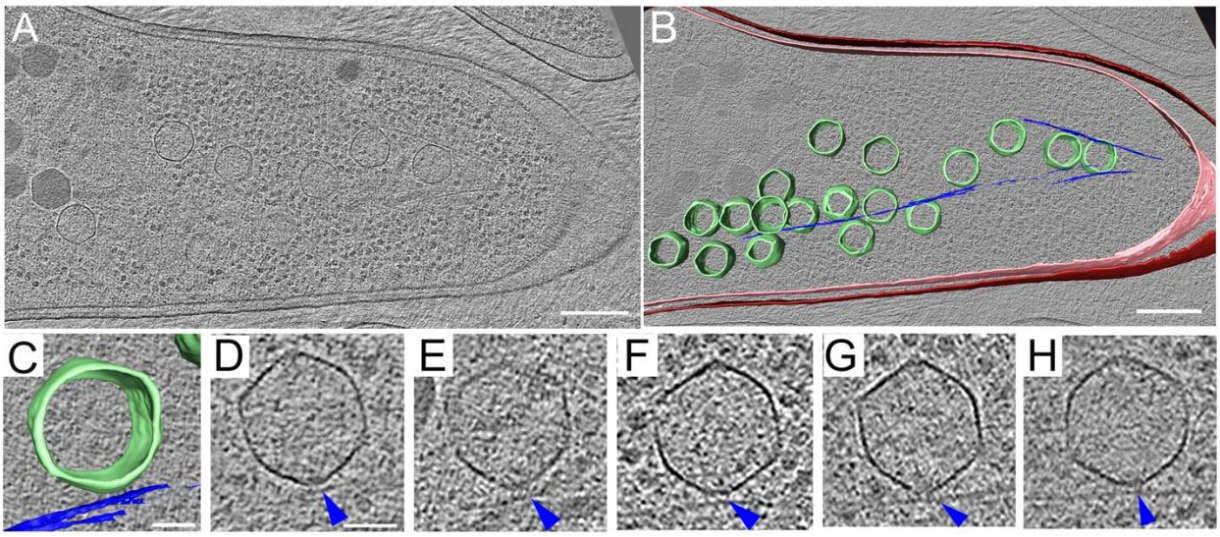

Figure 4.3: Cryo-electron tomography revealing capsids trapped along mutant PhuZ filaments during phage ΦPA3 infection in *P. aeruginosa* at 70 mpi. (A) A slice through a tomogram of a cryo-focused ion beam–thinned phage-infected cell at 70 mpi. Scale bar, 200 nm. **(B)** Annotation of the tomogram in **(A)** showing extracted structures, including capsids (green), cytoplasmic membrane (pink), outer membrane (red) and mutant PhuZD190A spindles (blue). Scale bar, 200 nm. **(C-D)** Zoomed-in view **(C)** of one of the capsids stuck on the mutant filament from the tomogram shown in **(A)** and its corresponding tomogram slice **(D).** Scale bar, 50 nm. **(E-H)** Slices of tomograms of capsids trapped along the mutant filaments from tomograms of other phage-infected cells taken for this study, with blue arrow pointing towards the mutant spindle.

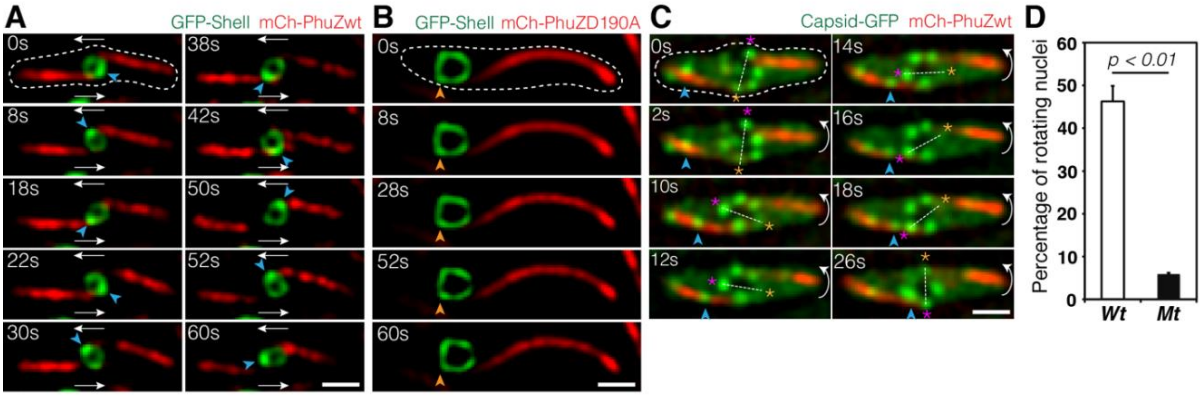

Figure 4.4: Rotation of the phage nucleus exerted by PhuZ spindle distribute phage capsids around the nucleus. (A-B) Rapid time-lapse imaging of phage 201Φ2-1 infected *P. chlororaphis* expressing GFP-tagged shell (gp105) with either mCherry-tagged wild-type PhuZ (gp059) **(A)** or mCherry-tagged mutant PhuZD190A (gp059) **(B)** during 60 second intervals. In the presence of wild-type filaments, the shell (green) rotates counter-clockwise when the PhuZ filaments push the shell transversely; the shell successfully rotates twice within 42 seconds. The mutant PhuZD190A is unable to catalyze GTP hydrolysis and appears static, resulting in a mispositioned and motionless shell within the infected cell. **(C)** Rapid time-lapse microscopy of phage 201Φ2-1 infected *P. chlororaphis* expressing GFP-tagged capsid (gp200) and mCherry-tagged wild-type PhuZ (gp059) in a 26 second interval. A capsid (arrow) travels along the filament from cell pole toward the phage nucleus which rotates counter-clockwise. The capsid docks on the surface of the nucleus at 26 seconds. Dashed lines indicate cell borders. Scale bars, 1 micron. **(D)** Graph showing the percentage of rotating nuclei in *P. chlororaphis* infected cells in the presence of either wild-type PhuZ (*wt*) or mutant PhuZD190A (*mt*). The graph shows that the number of rotating nuclei in the presence of wild-type PhuZ (46.2%) is significantly higher (*p value < 0.01*) than that in the presence of mutant PhuZD190A (5.9%). Data were collected from infected cells at 50 mpi from at least three different fields and are represented as mean ± standard error (n; wt = 611 and mt = 286).

Figure 4.5: PhuZ filaments treadmill unidirectionally toward the nucleus at a constant rate. (A) A single photobleaching event at the cell pole (arrow) moves toward the phage nucleus. **(B)** A double photobleaching event shows that bleach spots made at both cell poles (arrows) flux down the filaments toward the phage nucleus. Scale bars, 1 micron. **(C)** Graph showing rates of bleach spot movement (distance in microns versus time in seconds) in wildtype ΦPA3-PhuZ filaments, mutant ΦPA3-PhuZD190A filaments, and wildtype ΦPA3-PhuZ filaments treated with the antibiotic ticarcillin to produce elongated cells. **(D)** Graph showing rates of capsid movement (distance in microns versus time in seconds) when co-expressed with either wildtype ΦPA3-PhuZ or the mutant ΦPA3-PhuZD190A. **(E)** Box and whisker plots showing average speeds of movement of bleach spots on wild type PA3 PhuZ filaments (WT filament), on wild type PA3 PhuZ filaments in ticaricillin treated cells (Ticaricillin-treated filament), or on mutant PA3 PhuZD190A filaments (MT filament). Average speed of capsid movement in cells with wild PA3 PhuZ filaments (WT capsid) or mutant PA3 PhuZD190A filaments (MT capsid). **(F)** Model of PhuZ filament treadmilling, indicating addition of new subunits causes the bleached subunits (grey) to flux toward the nucleus.

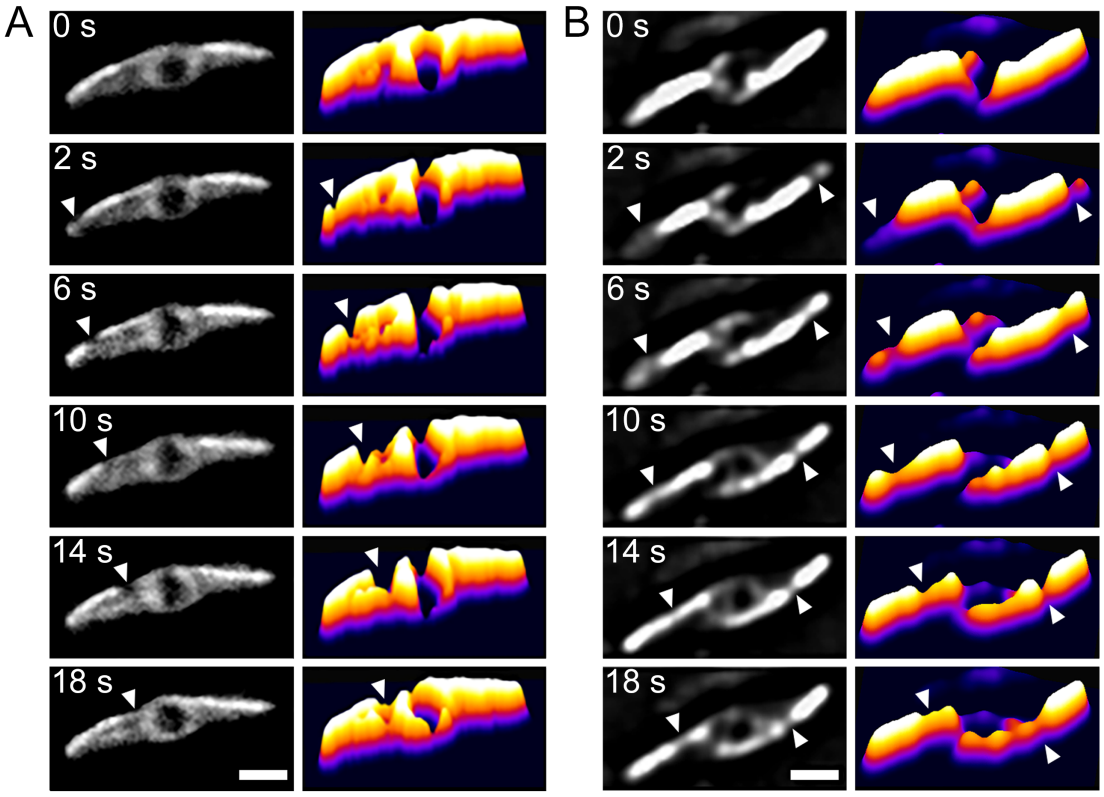
A
0 s
2 s
6 s
10 s
14 s
18 s
B
0 s
2 s
6 s
10 s
14 s
18 s

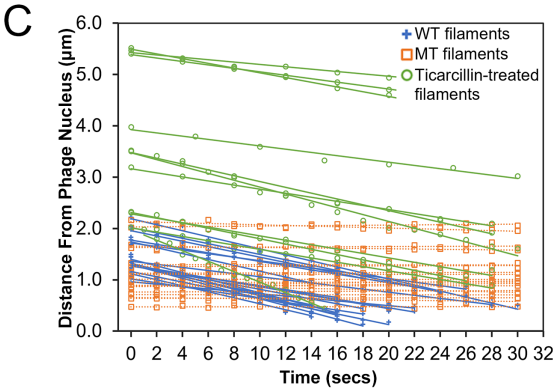
C
WT filaments
MT filaments
Ticarcillin-treated filaments
Distance From Phage Nucleus (µm)
Time (secs)

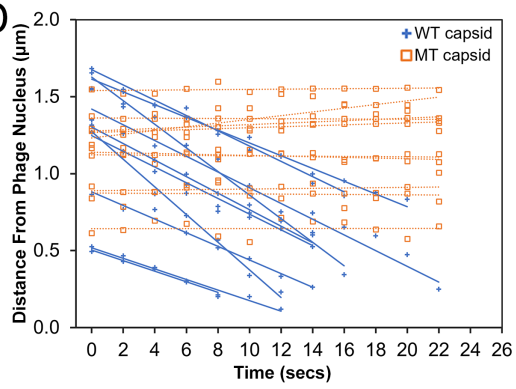
D
WT capsid
MT capsid
Distance From Phage Nucleus (µm)
Time (secs)

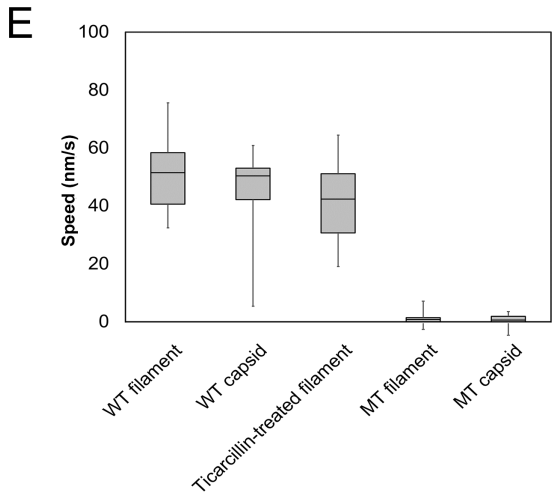
E
Speed (nm/s)
WT filament
WT capsid
Ticarcillin-treated filament
MT filament
MT capsid

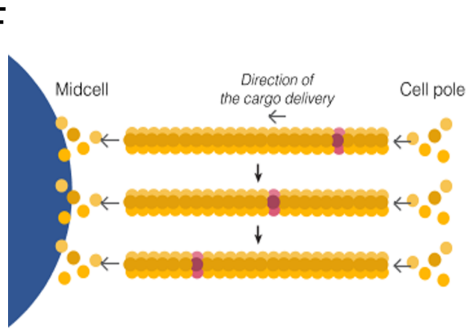
F
Midcell
Direction of the cargo delivery
Cell pole

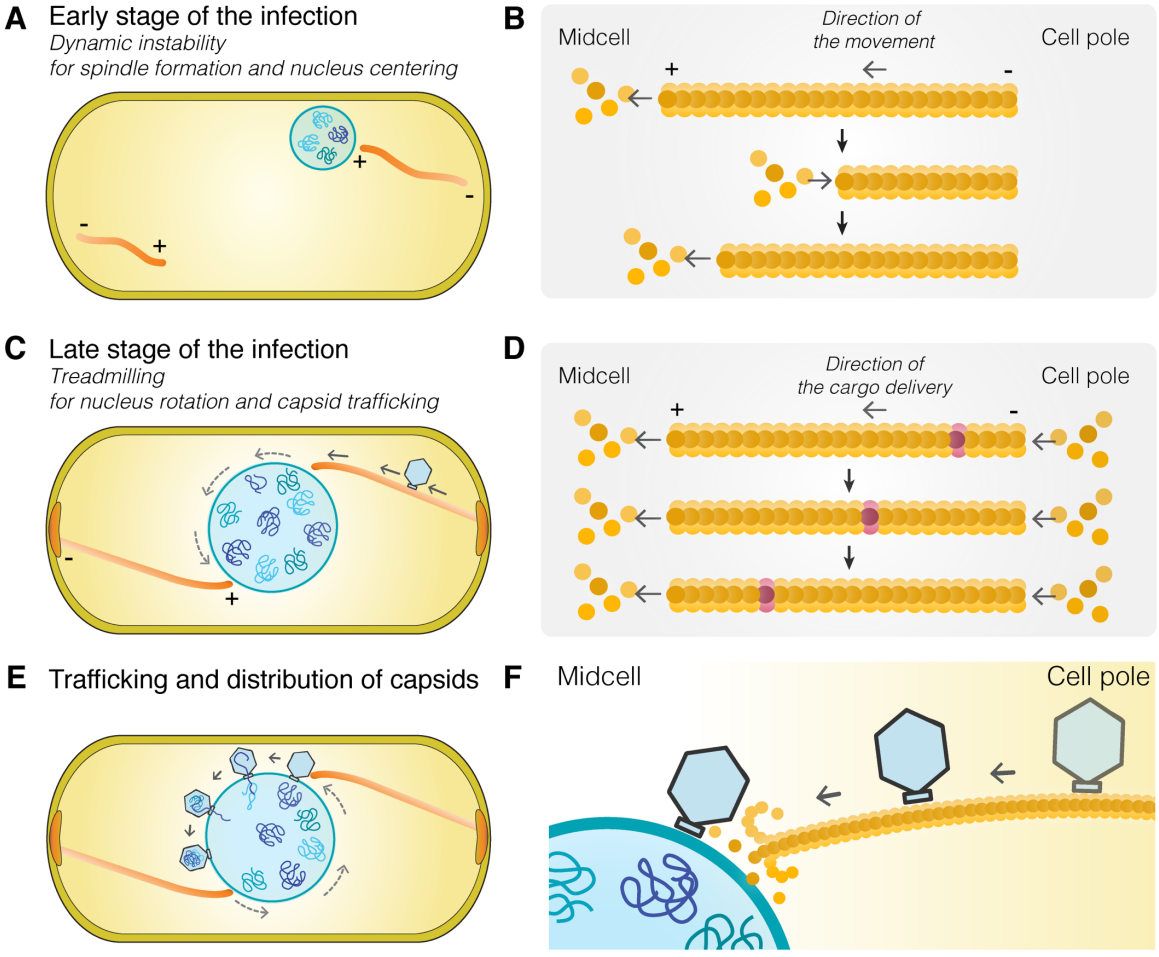

Figure 4.6: Model of capsid trafficking and the role of nucleus rotation in distributing capsids around the phage nucleus. The spindle's functions are complex and change as phage development proceeds. **(A)** At the onset of infection, dynamically unstable filaments assemble with minus ends anchored at the cell poles and plus ends oriented toward midcell push the growing phage nucleus to the cell midpoint where it oscillates in position. **(B)** Model of dynamically unstable filaments showing cycles of polymerization, depolymerization, and recovery at the plus end of the polymer. **(C)** Later in infection, the function of the spindle switches from centering the nucleus to rotating it in position and transporting capsids to the phage nucleus for DNA packaging. Treadmilling provides the driving force and temporally couples both processes. **(D)** Model of treadmilling filaments showing addition of new subunits at the minus end near the cell pole drives photobleached subunits (purple) toward midcell. **(E)** Rotation of the phage nucleus serves to distribute capsids evenly around its surface. **(F)** Capsids are delivered to the surface of the phage nucleus for DNA packaging.

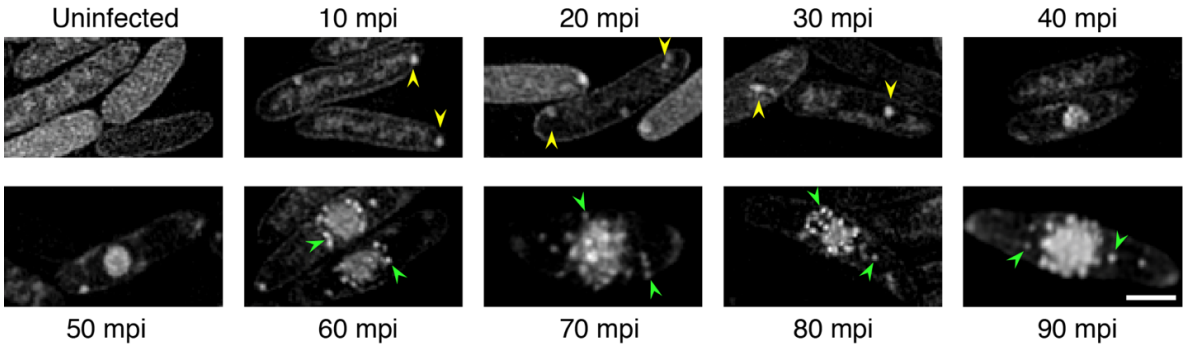

Figure S4.1: SIM images of uninfected and phage 201-infected *P. chlororaphis* at various time points to determine the development of the phage nucleus. *P. chlororaphis* cells were grown at 30°C for 3 hr and infected with high-titer phage 201 on an agarose pad and DNA was stained by DAPI (gray). At desired time points, the cells were fixed and visualized by SIM. Yellow arrows indicate the phage nucleus and green arrows indicate encapsidated phage particles that appear after 60 mpi. Scale bars, 1 micron.

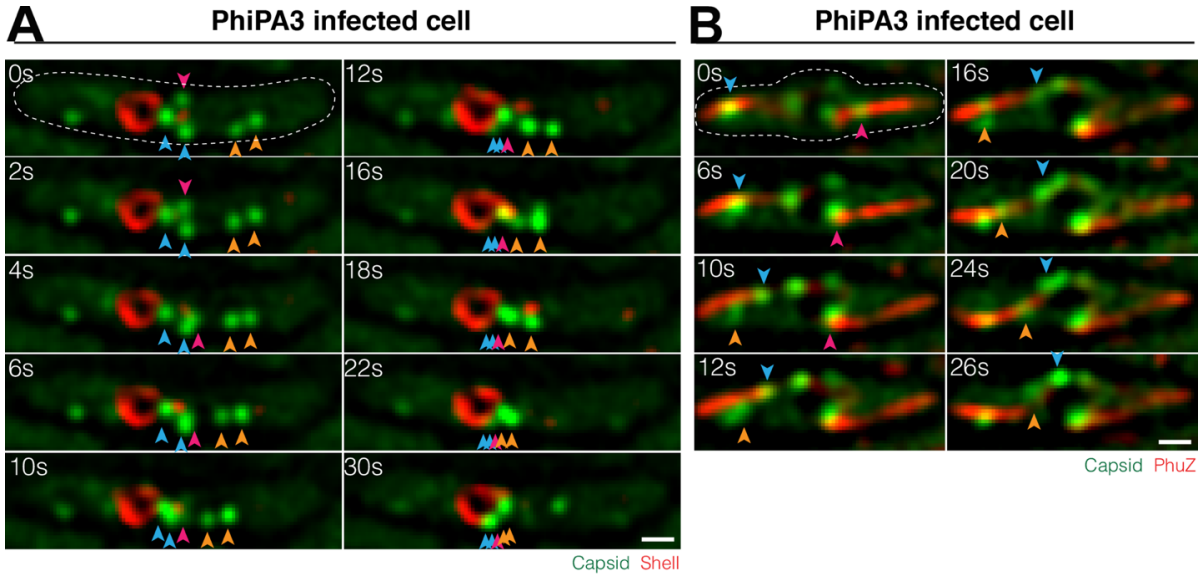

Figure S4.2: Phage PA3 capsids travel toward the nucleus located at midcell by moving along filaments of the PhuZ spindle. a, Rapid time-lapse imaging of GFP-tagged PA3-capsid; gp136 (green) and mCherry-tagged PA3-shell; gp053 (red) in *P. aeruginosa* infected with phage PA3 throughout an interval of 30 seconds. The trajectory of the capsid appears as a straight line toward midcell. Arrows indicate individual capsids. **b,** Rapid time-lapse imaging of mCherry-tagged PA3-capsid; gp136 (green) and GFP-tagged PA3-PhuZ (gp028; red) infected with phage PA3 during an interval of 26 seconds. The capsids (arrows) traffic along PhuZ filaments to the surface of the phage nucleus. Dashed lines indicate cell borders. Scale bars,1 micron.

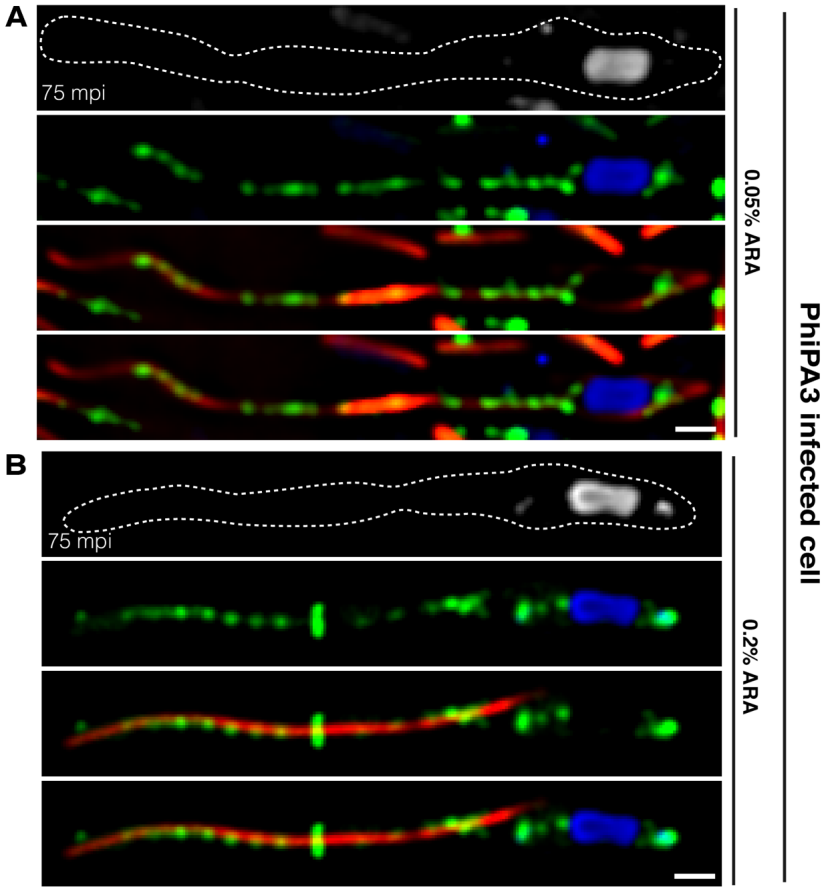

Figure S4.3: Phage PA3 capsids accumulate along mutant PA3-PhuZD190A spindles during infection at 75 mpi. a, b, Still images of *P. aeruginosa* expressing mCherry-tagged PA3-capsid; gp136 (false colored green) and GFP-tagged PA3-mutant PhuZD190A (gp028; false colored red) induced at 0.05% (**a**) and 0.2% arabinose (**b**). Static filaments caused mispositioning of the nucleus during infection. Capsids were trapped along filaments and phage encapsidated particles were rarely seen. Dashed lines indicate cell borders. Scale bars, 1 micron.

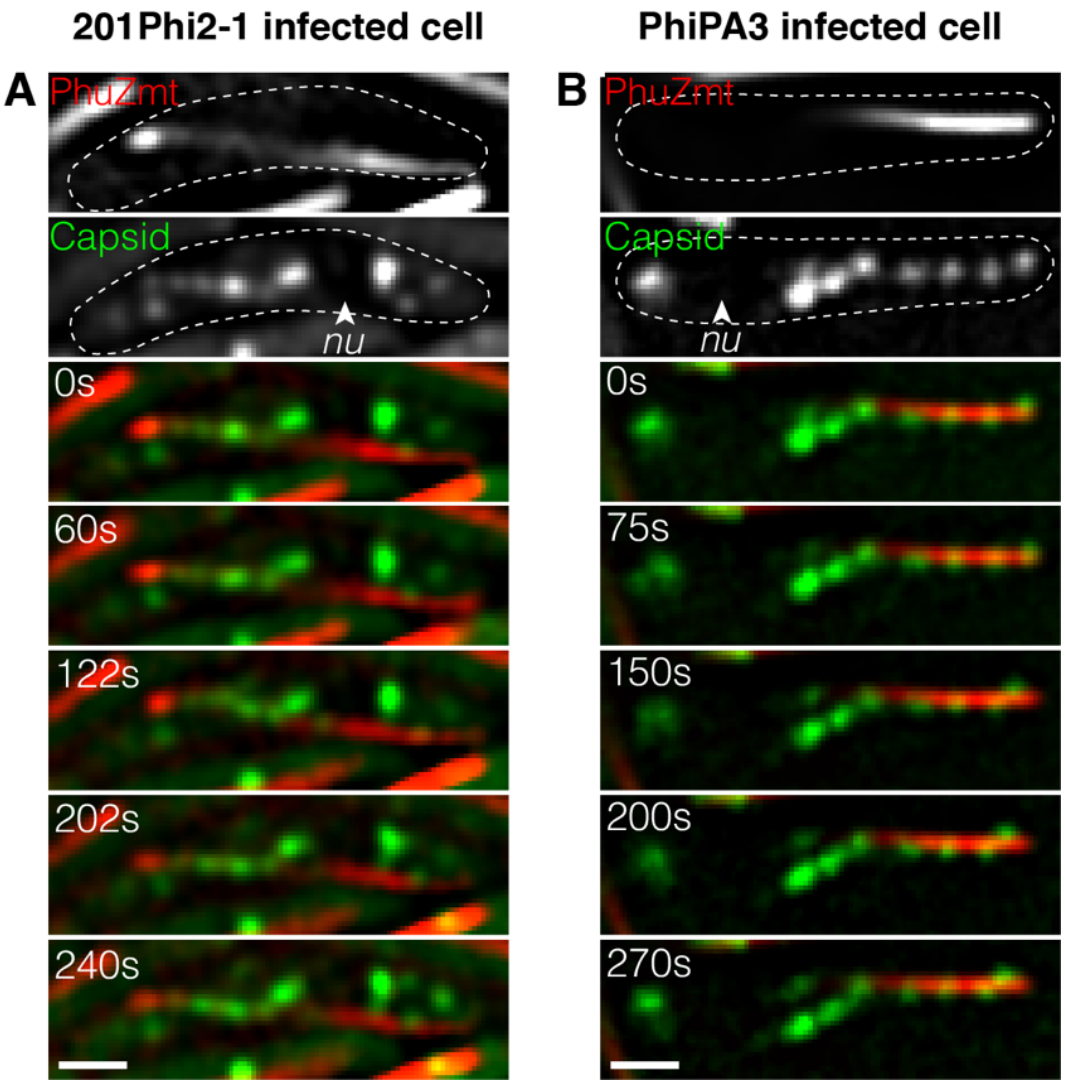

Figure S4.4: Phage capsid trafficking is dependent on the ability of PhuZ to hydrolyze GTP in both phage 201 and PA3. a, b, Time-lapse imaging of *P. chlororaphis* expressing GFP-tagged 201-capsid (gp200) and mCherry-tagged 201-mutant PhuZD190 (gp059) over 240 seconds (**a**) and *P. aeruginosa* expressing mCherry-tagged PA3-capsid (gp136; green) and GFP-tagged PA3-mutant PhuZD190A (gp028; red) over 270 seconds (**b**). The capsids localized to static filaments and appeared motionless throughout the time observed suggesting that capsid trafficking is dependent on treadmilling of PhuZ filaments. Dashed lines indicate cell borders. Scale bars, 1 micron.

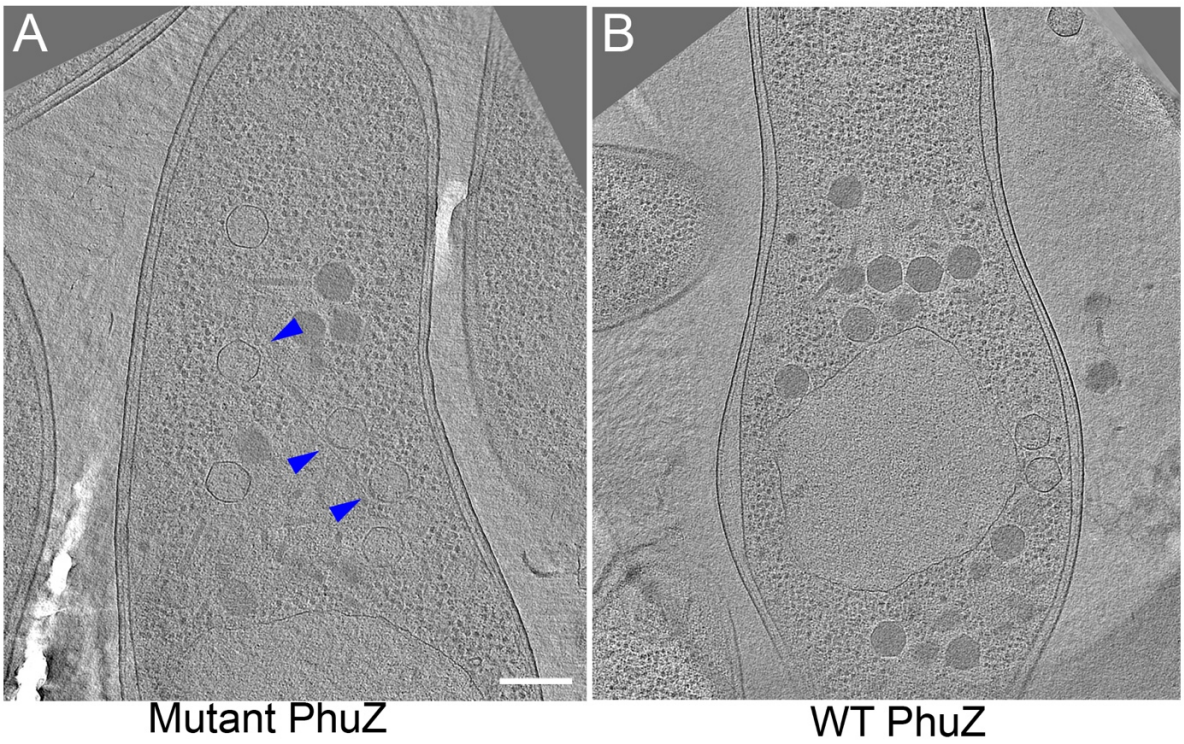

Figure S4.5: Cryo-electron tomography depicting strains with mutant PhuZD190A and WT PhuZ expressed during phage PA3 infection in *P. aeruginosa.* a, Slice through a tomogram of a cryo-focused ion beam–thinned phage-infected cell with mutant PhuZD190A at 70 mpi with capsids trapped on filaments (blue arrows) highlighted and empty capsids indicating delayed DNA packaging. Scale bar, 200 nm. **b**, Slice through a tomogram of a phage-infected cell expressing wild type PhuZ at 70 mpi with normal encapsidation. At this time point in the wild-type cell, capsids in the cytoplasm are filled with DNA.

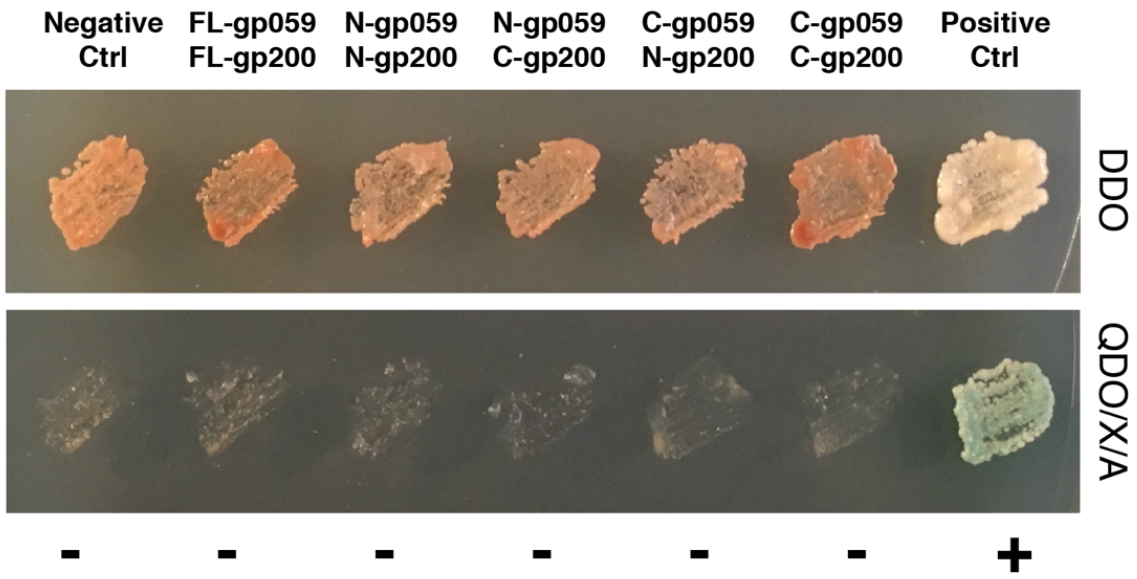

Figure S4.6: Interaction assay between phage 201 PhuZ (gp059) and phage 201 capsid (gp200) using Yeast Two-hybrid assay. The yeast strains containing either full-length (FL), N-terminus, and C-terminus of PhuZ (gp059) protein was mated with the yeast strains containing either FL, N-terminus, and C-terminus of capsid (gp200) protein. The mated cultures were plated on selective agar plates DDO to select the presence of plasmids and on high stringency plate QDO/X/A to investigate the positive interaction. None of them except the positive control grew on the high stringency plate QDO/X/A indicating that PhuZ protein does not directly interact with capsid protein in this assay.

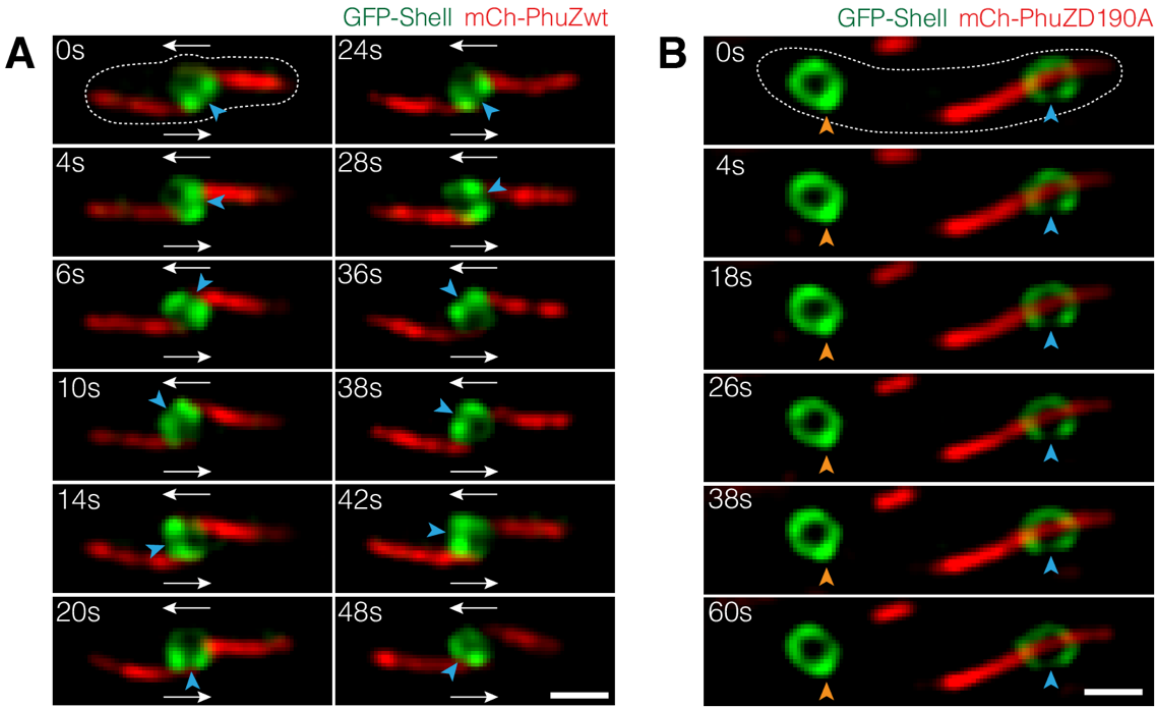

Figure S4.7: Additional time-lapse imaging of rotating nucleus in the phage 201-infected *P. chlororaphis* expressing either mCherry-tagged wild-type PhuZ (a) or mutant PhuZD190A (b). In the presence of wild-type filaments, the shell (green) successfully rotates two revolutions in the counter-clockwise direction within 48 seconds when the PhuZ filaments push the shell transversely (**a**). Shells appear static in the presence of the mutant PhuZD190A filament (**b**). Dashed lines indicate cell borders. Scale bars, 1 micron.

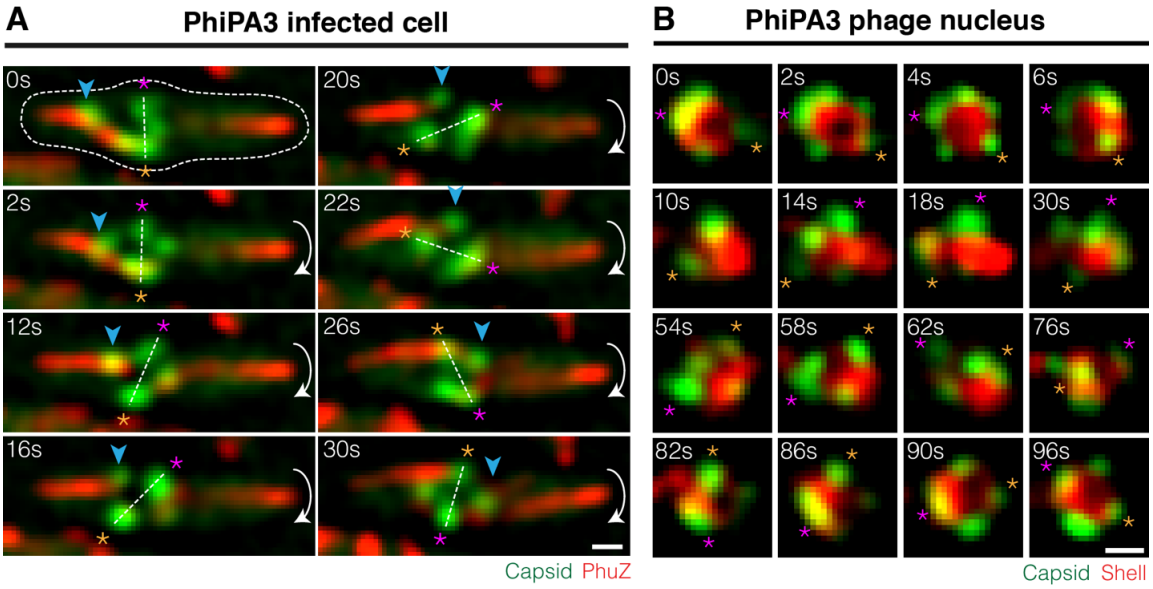

Figure S4.8: PA3 capsids traffic along filaments, dock on the surface of the phage nucleus while rotating, and move with the nucleus as a singular structure. a, Time-lapse microscopy of phage PA3-infected *P. aeruginosa* expressing mCherry-tagged PA3-capsid (gp136; green) and GFP-tagged PA3-PhuZ (gp028; red) over a 30 second interval. A capsid (arrow) travels along the filament from cell pole toward the phage nucleus while rotating clockwise. Once the capsid arrives at the nucleus, it docks on the nuclear surface at 20 seconds and then rotates with the nucleus as a single structure from 22 to 30 seconds. Dashed lines indicate cell borders. Scale bars, 1 micron. **b**, Time-lapse microscopy of the rotating phage PA3 nucleus in *P. aeruginosa* expressing GFP-tagged capsid (gp136; green) and mCherry-tagged shell (gp053; red) during a 96 second interval. The capsids dock tightly on the nuclear surface and rotate with the structure as a single unit. Asterisks were used to track a single capsid for the duration of the time-lapse. Scale bars, 0.5 micron.

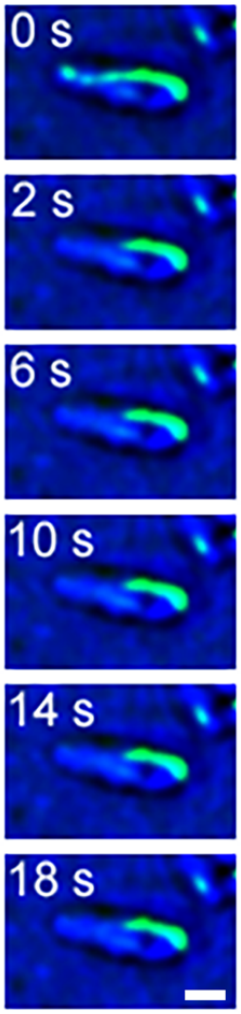

Figure S4.9: The mutant PhuZD190A polymer, deficient in GTP hydrolysis, fails to treadmill. A single photobleaching event of the mutant PA3PhuZD190A shows no movement over time (s) of the mark toward the phage nucleus. Scale Bar, 1 micron

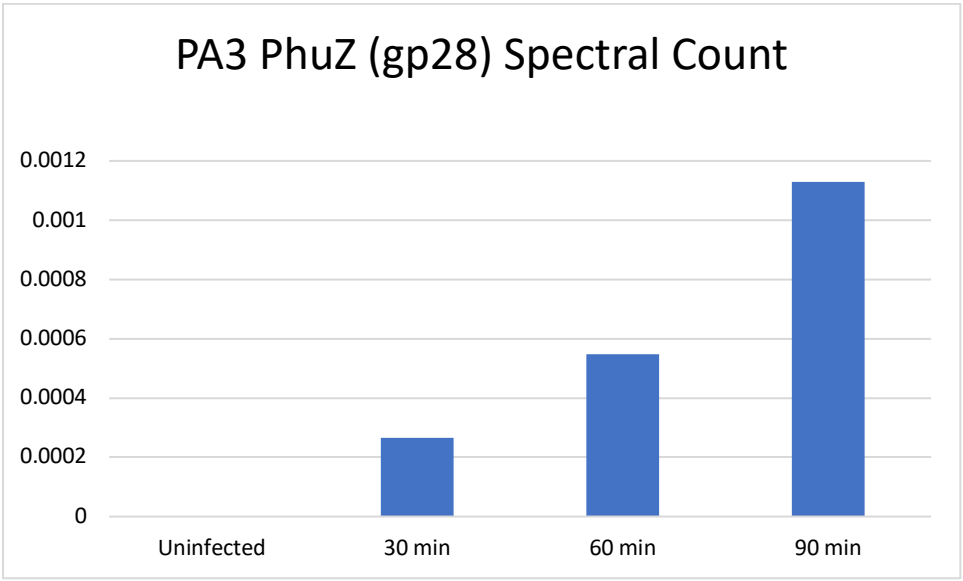

Figure S4.10: Spectral count of proteomics performed on PA3-infected *P. aeruginosa* cells. The concentration of PhuZ increases as infection progresses.

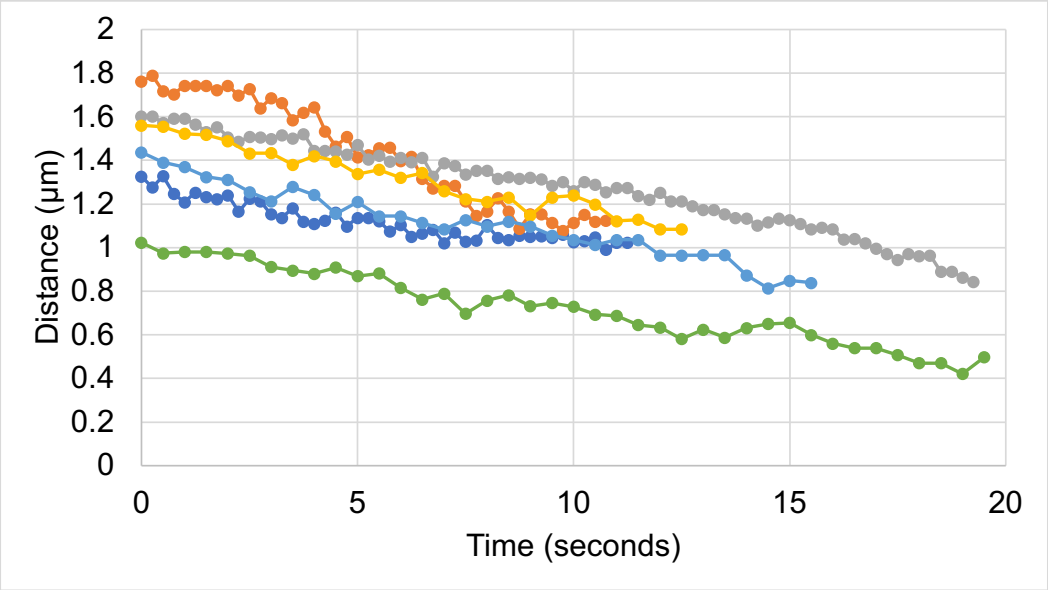

Figure S4.11: Graph showing rates of bleach spot movement (distance versus time) in wildtype ΦPA3-PhuZ filaments and mutant ΦPA3-PhuZD190A filaments, after treatment with ticarcillin and at shorter time intervals.

Figure S4.12: Phylogenetic tree of PhuZ homologs in relation to other tubulin families. The PhuZ branch is shown in green. These sequences include PhuZ homologs from *Pseudomonas aeruginosa* phages PhiPA3 (PA3), PhiKZ (KZ), KTN4, EL, SL2; *Pseudomonas chlororaphis* phage 201phi2-1 (201.0); *Pseudomonas fluorescens* SBW25 phages Phabio, Noxifer, OBP; *Ralstonia* phages RSF1, RSL2; Halocynthia phage JM-2012; *Erwinia amylovora* phages PhiEaH1 and Ea35-70; *Bacillus megaterium* phage G; *Vibrio* phage Aphrodite1, and *Gammaproteobacteria* bacterium TMED104. Bacterial tubulin TubZ is shown in red with sequences from *B. thuringiensis* pBtoxis orf156 (Bt), *B. anthracis* pXO1 orf45 (Ba), *B. cereus* pBc218 orf139 (Bc). FtsZ in bacteria, archaea, and plants are in yellow. These include proteins from *Natrinema ejinorense* (N. ejinorense), *Natronoarchaeum philippinense* (N.philippinense), *Salinigranum rubrum* (S. rubrum), *Haloferax volcanii* (H. volcanii), *Haloarcula hispanica* (Hh1), *Haloarcula marismortuxi* (Hm1), *Methanococcoides burtonii* (Mb1), *Archaeoglobus fulgidus* (Af1), *Pyrococcus abyssi* (Pa1). Plant FtsZ proteins come from chloroplastic *Citrus clementina,* Arabidopsis thaliana, chloroplastic *Arabidopsis lyrata* subsp. Lyrate, and *Marchantia polymorphia*. The FtsZ branch also includes *Mycobacterium tuberculosis* H37Rv (Mt), *Bacillus subtilis* (Bs), *Escheria coli* (Ec), Halobacterium sp. NRC-1(Hh2), *Pyrococcus horikoshii* (Ph2), *Pyrococcus abyssi* (pa2). Clostridial tubulins from phage and bacteria are shown in purple and include CAC3459 *Clostridium acetobutylicum* ATCC824 (CA), CBY3413 *C. butyricum* 5521 (Cb), CKL0570 *C. kluyveri* DSM555 (Ck), Clocel4294 *C. cellulovorans* 743B (Cl), pCLG2A0045 *C. botulinum* str.1873 (pCL2), CBCA1765 *C. botulinum* C str. (Cbc), and Cst189 *C. botulinum* phage C-st (Cst). Tubulins are shown in blue. Both bacterial tubulins BtubA and BtubB proteins are encoded in the genomes of P*rosthecobacter debontii, Prosthecobacter vaneervenii, Prosthecobacter dejonge,* and *Prosthecobacter fusiformis*. Eukaryotic tubulins include the following proteins: *Homo sapiens* epsilon chain (Hse), *Xenopus laevis* epsilon (Xle), *Homo sapiens* delta chain (HsD), *Xenopus laevis* delta (XID), *Saccharomyces cerevisiae* gamma (ScG), *Homo sapiens* gamma 1 (HsG), *Sus scrofa* tubulin beta (SsB), *Xenopus laevis* tubulin beta-4 chain (XIB), *Saccharomyces cerevisiae* beta chain (ScB), *Xenopus laevis* alpha (XIA), *Sus scrofa* alpha (SsA), *Saccharomyces cerevisiae* alpha (ScA).

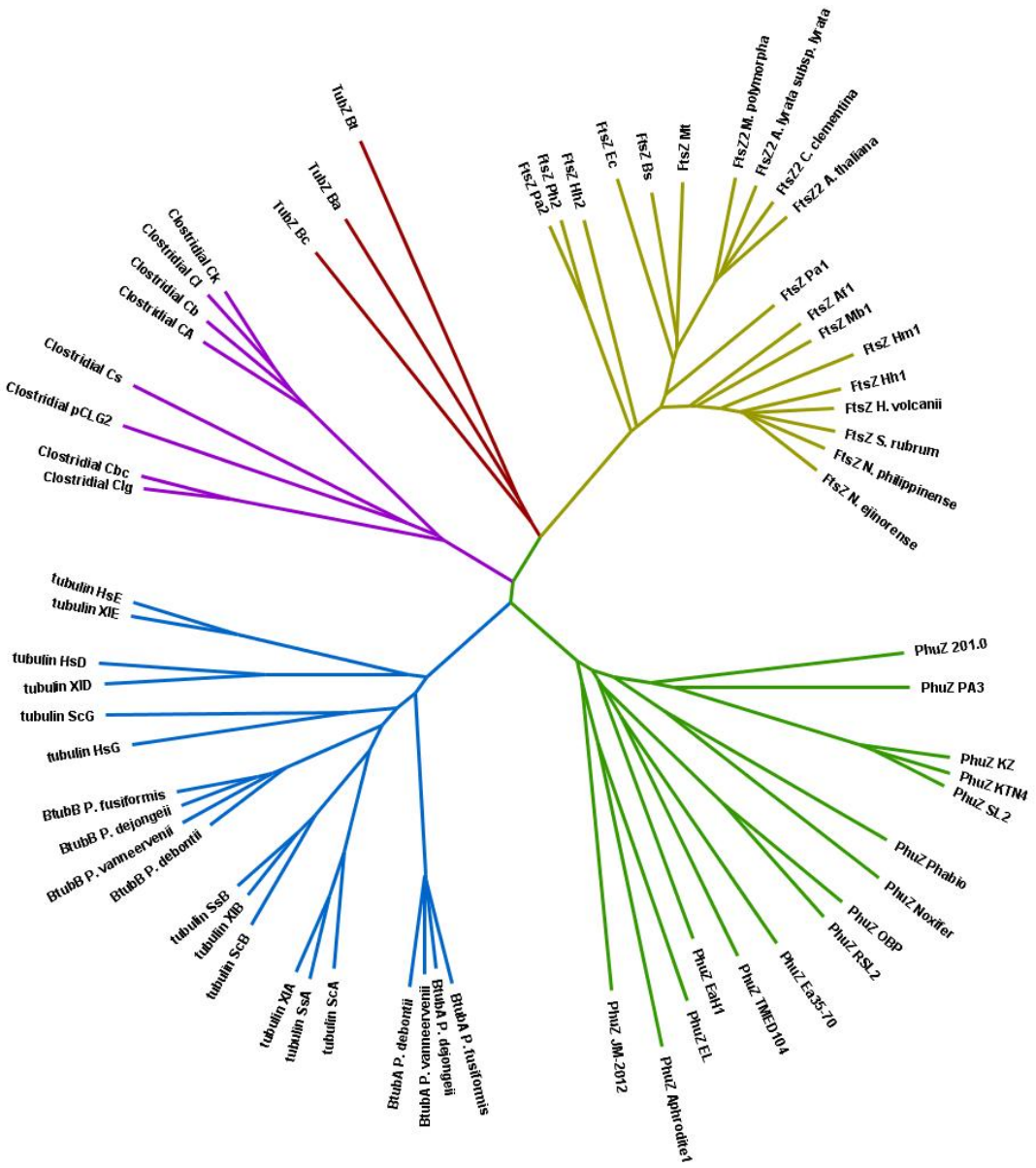
TubZ Bt
TubZ Ba
TubZ Bc
Clostridial Ck
Clostridial Cf
Clostridial Cb
Clostridial CA
Clostridial Cs
Clostridial pCLG2
Clostridial Cbc
Clostridial Clg
FtsZ Pa2
FtsZ Ph2
FtsZ Hh2
FtsZ Ec
FtsZ Bs
FtsZ Mt
FtsZ2 M. polymorpha
FtsZ2 A. lyrata subsp. lyrata
FtsZ2 C. clementina
FtsZ2 A. thaliana
FtsZ Pa1
FtsZ Af1
FtsZ Mb1
FtsZ Hm1
FtsZ Hh1
FtsZ H. volcanii
FtsZ S. rubrum
FtsZ N. philippinense
FtsZ N. ejinorense
tubulin HsE
tubulin XIE
tubulin HsD
tubulin XID
tubulin ScG
tubulin HsG
BtubB P. fusiformis
BtubB P. dejongeii
BtubB P. vanneervenii
BtubB P. debontii
tubulin SsB
tubulin XIB
tubulin ScB
tubulin XIA
tubulin SsA
tubulin ScA
BtubA P. debontii
BtubA P. vanneervenii
BtubA P. dejongeii
BtubA P. fusiformis
PhuZ 201.0
PhuZ PA3
PhuZ KZ
PhuZ KTN4
PhuZ SL2
PhuZ Phabio
PhuZ Noxifer
PhuZ OBP
PhuZ RSL2
PhuZ Ea35-70
PhuZ TMED104
PhuZ EaH1
PhuZ EL
PhuZ Aphrodite1
PhuZ JM-2012

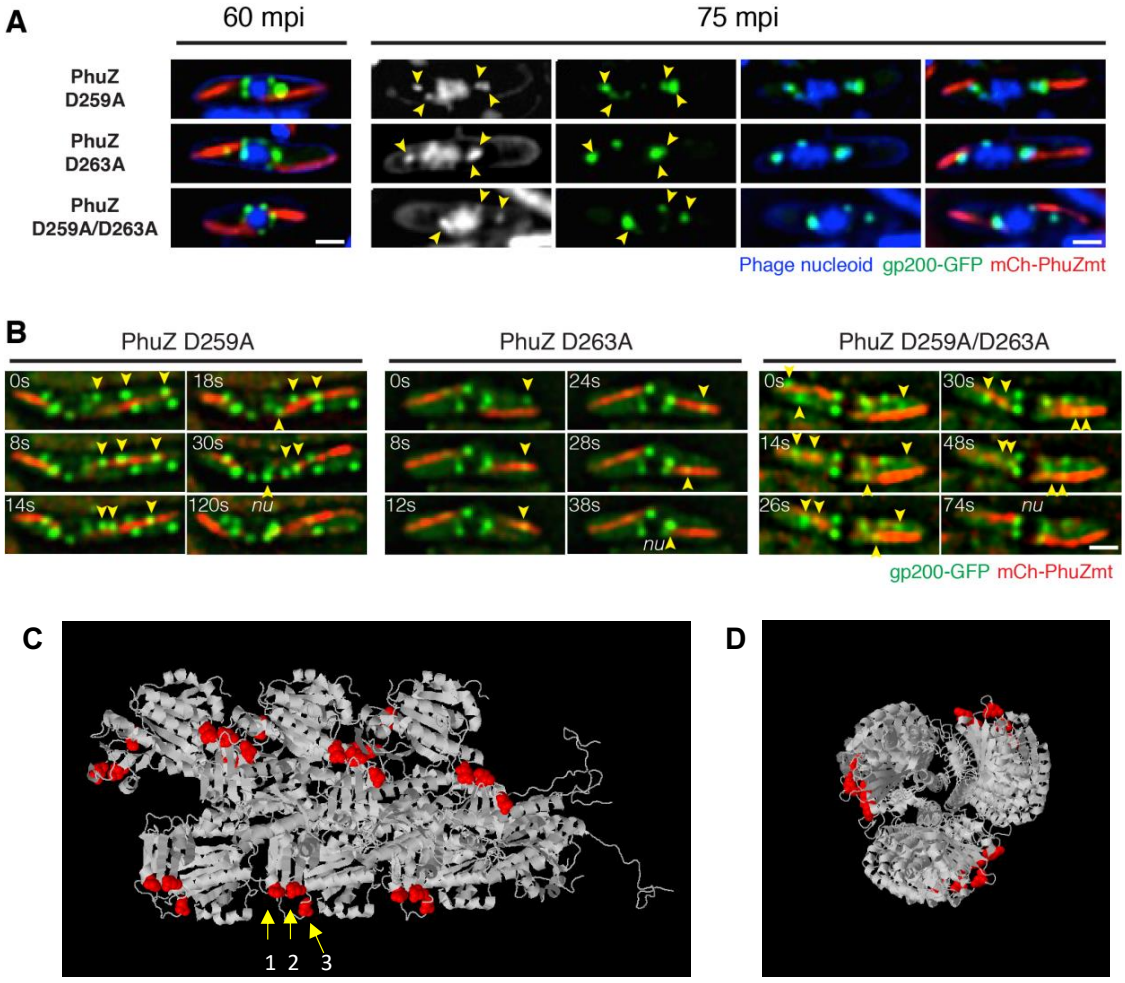

Figure S4.13: Phage 201 capsids traffic to the phage nucleus along PhuZ filaments containing mutations in conserved aspartic acid residues (**a, b**). Structure of PhuZ filament with the conserved aspartic residues highlighted **(c, d). a,** Fluorescence microscopy of phage-201 infected strains containing PhuZD259A, D263A, and D259A-D263A mutant filaments at 60 and 75mpi. Arrows indicate position of 201 capsids (gp200; green) along respective mutated PhuZ filaments (gp059; red). **b,** Time-lapse microscopy of phage-201 infected strains containing PhuZD259A, D263A, and D259A-D263A mutant filaments. Arrows indicate the position of 201 capsids (gp200; green) along respective mutated PhuZ filaments (gp059; red). Scale bar, 1 micron. Structure of a PhuZ 201 filament (PDB ID: 3J5V) viewed from the side (**c**) and top (**d**). Arrow 1 indicates amino acid D235, arrow 2 indicates D263, and arrow 3 indicates D259 (**c**).

Experimental Procedures

Strain, growth condition, and bacteriophage preparation

Pseudomonas chlororaphis strain 200-B was grown on Hard Agar (HA) containing 10 g Bacto-Tryptone, 5 g NaCl, and 10 g agar in 1L ddH_2O and incubated at 30°C overnight. *Pseudomonas aeruginosa* strains PA01 and PA01-K2733 (pump-knockout strain) were grown on Luria-Bertani (LB) media containing 10g Bacto-Tryptone, 5g NaCl, 5g Bacto-yeast extract in 1L ddH_2O and incubated at 30ºC overnight. Lysates for phages 201Φ2-1 and ΦPA3 were made by infecting respective saturated host cultures with 10μl of high titer lysate, incubating for 15 minutes at room temperature, mixing with HA top agar (0.35%; phage 201Φ2-1) or LB top agar (0.35%; phage ΦPA3) and pouring over corresponding HA or LB plates. Plates were incubated at 30ºC overnight. Plates that formed web-lysis were then flooded with 5mL of phage buffer and incubated at room temperature for 5 hours. The phage lysates were then aspirated, clarified by centrifugation at 15,000 rpm for 10 minutes, and stored at 4°C with 0.01% chloroform by volume.

Plasmid constructions and bacterial transformation

Fluorescent-tagged phage proteins were constructed into the pHERD30T vector backbone. Phage genes were directly amplified from high-titer lysates of phages 201Φ2-1 or ΦPA3 using PCR amplification. Amplicons and vector backbones were then ligated together to generate phage gene-containing plasmids via isothermal assembly, immediately followed by transformation into *E. coli* DH5α plated on LB supplemented with gentamycin sulfate (15μg/mL). Constructs were confirmed with sequencing and

subsequently electroporated into either *P. chlororaphis* strain 200-B or *P. aeruginosa* strains PA01 and/or PA01-K2733. *P. chlororaphis* strain was grown on HA supplemented with gentamycin sulfate (25*μ*g/mL) and *P. aeruginosa* strains PA01 and PA01-K2733 were grown on LB supplemented with gentamycin sulfate either at 300 *μ*g/mL or 15*μ*g/mL, respectively. See Supplemental Table 1 for a list of plasmids and strains.

Single cell-infection assay

The bacterial cells were grown on 1.2% agarose pads, supplemented with desired arabinose to induce fluorescent-tagged protein expression to label wild-type proteins from phage. The cells were then incubated at 30°C for 3 hours without a coverslip in a humid chamber. 5 µl of high-titer lysate (10^{10} pfu/ml) was added to the corresponding host cells on agarose pads to begin the phage infection, and then the cells were further incubated to allow phage infections occur. For ticarcillin treated experiments, 10*μ*l of 50mg/ml TIC stock was added to cells 1.5 hours post inoculation on agarose pads and infection was performed thereafter as mentioned above. At desired time points after phage infection, a coverslip was put on the slide and fluorescent microscopy was then initiated. Data of static images and time-lapse imaging were collected and processed as described below.

Fixed and live cell static-image fluorescence microscopy

The fixed cell imaging protocol was adopted from “Fixed Cell Imaging” methodology in Chaikeeratisak et al., 2017. The DeltaVision Spectris Deconvolution microscope (Applied Precision, Issaquah, WA, USA) was used to visualize the fixed and live cells. For static images, the cells were imaged at 8 stacks in the Z-axis from the focal plane with 0.15 µm increments. Images were further processed by the deconvolution

algorithm in DeltaVision SoftWoRx Image Analysis Program. Further image analysis and processing was performed in Fiji.

Time-lapse fluorescence microscopy

For time-lapse imaging, the cells were prepared and infected as indicated above. Cells were imaged from a single stack at the focal plane for desired length of time at selected intervals using Ultimate Focusing mode. Timelapse images were later deconvolved and analyzed as stated above.

3D-Structured Illumination Microscopy (SIM)

Pseudomonas cells were grown, infected, and fixed as indicated above. Cells were stained with 1 μg/mL DAPI and then imaged using an Applied Precision/GE OMX V2.2 Microscope. Microscopic raw data were sequentially taken by SI-super-resolution light path to collect 3 mm thickness of samples with 125 nm increments in the z-axis with compatible immersion oils (Applied Precision). 3D-SIM images were then rendered by standard OMX SI reconstruction parameters in DeltaVision SoftWoRx Image Analysis Program.

Fluorescence Recovery After Photobleaching

For time-lapse imaging, the cells were prepared and infected as indicated above. Filaments were photobleached using a laser (QLM module, API) for 0.05 sec at 31.3% power and then followed with time lapse imaging – images taken every 2 seconds for 1 minute with the Applied Precision/GE OMX V2.2 Microscope. Images were deconvolved with DeltaVision SoftWoRx.

Yeast Two-hybrid assay

Interaction between the proteins of interest was investigated using the Yeastmaker Yeast Transformation System 2®. Partial gene and full-length gene were cloned into the bait (pGBKT7) and prey (pGADT7) vector (Clontech), as described in Supplemental Table 1. The resulting recombinant constructs were transformed into the yeast *Saccharomyces cerevisiae* strain Gold and Y187 (Clontech) using the Yeastmaker™ Yeast Transformation System 2 (Clontech). Both yeast colonies containing the protein of interest were paired in a single 1.5mL centrifuge tube containing 500μL of 2X YPDA and vortexed to mix. Colonies were incubated shaking at 200 rpm at 30ºC overnight. The mated cultures were plated on selective agar plates DDO and QDO/X/A to investigate the positive interaction. All constructs were tested for toxicity and autoactivation prior to the experiments. Y2HGold containing pGBKT7-53 with Y187 containing pGADT7-T was used as the positive control and Y2HGold containing pGBKT7-Lam with Y187 containing pGADT7-T was used as the negative control.

Tomography Sample Preparation and Data Acquisition

Infection of *P. aeruginosa* cells with phage ΦPA3 was done as indicated above. At 70 mpi, cells were scraped off from the surface of the pad using ¼ LB media. 7 μl of cells were deposited on holey carbon coated QUANTIFOIL® R 2/1 copper grids that were glow discharged using Pelco easiGlow™ glow discharge cleaning system. Manual blotting from the side of the grid opposite to the cells using Whatman No. 1 filter paper removed excess liquid such that cells form a monolayer on the surface of the grid. Cells were then

plunge-frozen in a mixture of ethane/propane using a custom-built vitrification device (Max Planck Institute for Biochemistry, Munich).

Grids were then mounted into modified FEI Autogrids™ to avoid any mechanical damage to the delicate grids during subsequent transfer steps. Then, these clipped grids were transferred into Scios (Thermo Fisher Scientific, formerly FEI), a dual-beam (cryo-FIB/SEM) microscope equipped with a cryogenic stage. Thin sections of 100-250 nm, or lamellae, were prepared as previously described in Chaikeeratisak et al., 2017 containing 10-12 cells each.

Tilt-series were collected from typically -65° to +65° with 1.5° or 2° tilt increments using SerialEM[4] in a 300-keV Tecnai G2 Polara microscope (FEI) equipped with post-column Quantum Energy Filter (Gatan) and a K2 Summit 4k x 4k direct detector camera (Gatan). Images were recorded at a nominal magnification of 34,000 with a pixel size of 0.61 nm. The dose rate was set to 10-12 e/physical pixel at the camera level. Frame exposure was set to 0.1 seconds, with a total exposure in a frame set to be determined by an algorithm targeting an average count number. The total dose in a tomogram was typically ~100-120 e/A^2 with a defocus of -5 μm. The dataset for this study consists of 16 tomograms from 7 FIB-milled lamellas. Reconstruction of tilt-series was done in IMOD (Kremer et al., 1996) using patch tracking method. Semi-automatic segmentation of the membranes was done using TomoSegMemTV (Martinez-Sanchez et al., 2014), an open-source software based on tensor voting, followed by manual segmentation with Amira software (FEI Visualization Sciences Group). Filaments were traced manually using Amira as well.

Quantitative and statistical analysis

To visualize the consensus location of gp200 (capsids), 32 single cell images from each experiment, wild type and mutant, were aligned and stacked using FIJI image analysis program (Schindelin et al., 2012). Then, the average GFP signals of all images in the stack were projected onto a single image. To visualize gp200 distribution of each cell, the GFP signal from each single cell image was combined in to a 1-pixel line and stacked. Performing on 8-bit GFP channel images, the location of gp200 from mid-cell was automatically measured by CellProfiler 2.0 image analysis program (Lamprecht et al., 2007) and normalized by cell length. Locations of bleach spots and capsids were measured from microscopy images in FIJI and plotted as distance over time in Microsoft Excel.

References

1. Cohen S, Au S, Pante N. 2011. How viruses access the nucleus. Biochim Biophys Acta 1813:1634-45.

2. Greber UF, Way M. 2006. A superhighway to virus infection. Cell 124:741-54.

3. Sodeik B, Ebersold MW, Helenius A. 1997. Microtubule-mediated transport of incoming herpes simplex virus 1 capsids to the nucleus. J Cell Biol 136:1007-21.

4. Portilho DM, Persson R, Arhel N. 2016. Role of non-motile microtubule-associated proteins in virus trafficking. Biomol Concepts 7:283-292.

5. Ward BM. 2011. The taking of the cytoskeleton one two three: how viruses utilize the cytoskeleton during egress. Virology 411:244-50.

6. Dohner K, Wolfstein A, Prank U, Echeverri C, Dujardin D, Vallee R, Sodeik B. 2002. Function of dynein and dynactin in herpes simplex virus capsid transport. Mol Biol Cell 13:2795-809.

7. Nturibi E, Bhagwat AR, Coburn S, Myerburg MM, Lakdawala SS. 2017. Intracellular Colocalization of Influenza Viral RNA and Rab11A Is Dependent upon Microtubule Filaments. J Virol 91.

8. Iwamoto M, Cai D, Sugiyama M, Suzuki R, Aizaki H, Ryo A, Ohtani N, Tanaka Y, Mizokami M, Wakita T, Guo H, Watashi K. 2017. Functional association of cellular microtubules with viral capsid assembly supports efficient hepatitis B virus replication. Sci Rep 7:10620.

9. Kraemer JA, Erb ML, Waddling CA, Montabana EA, Zehr EA, Wang H, Nguyen K, Pham DS, Agard DA, Pogliano J. 2012. A phage tubulin assembles dynamic filaments by an atypical mechanism to center viral DNA within the host cell. Cell 149:1488-99.

10. Erb ML, Kraemer JA, Coker JK, Chaikeeratisak V, Nonejuie P, Agard DA, Pogliano J. 2014. A bacteriophage tubulin harnesses dynamic instability to center DNA in infected cells. Elife 3.

11. Zehr EA, Kraemer JA, Erb ML, Coker JK, Montabana EA, Pogliano J, Agard DA. 2014. The structure and assembly mechanism of a novel three-stranded tubulin filament that centers phage DNA. Structure 22:539-48.

12. Zehr EA, Rohu A, Liu Y, Verba KA, Pogliano J, Grigorieff N, Agard DA. 2018. Mechanistic Origins of Dynamic Instability in Filaments from the Phage Tubulin, PhuZ. bioRxiv.

13. Chaikeeratisak V, Nguyen K, Khanna K, Brilot AF, Erb ML, Coker JK, Vavilina A, Newton GL, Buschauer R, Pogliano K, Villa E, Agard DA, Pogliano J. 2017. Assembly of a nucleus-like structure during viral replication in bacteria. Science 355:194-197.

14. Chaikeeratisak V, Nguyen K, Egan ME, Erb ML, Vavilina A, Pogliano J. 2017. The Phage Nucleus and Tubulin Spindle Are Conserved among Large Pseudomonas Phages. Cell Rep 20:1563-1571.

15. Mendoza SD, Berry JD, Nieweglowska ES, Leon LM, Agard D, Bondy-Denomy J. 2018. A nucleus-like compartment shields bacteriophage DNA from CRISPR-Cas and restriction nucleases. bioRxiv.

16. Aylett CH, Izoré T, Amos LA, Löwe J. 2013. Structure of the tubulin/FtsZ-like protein TubZ from Pseudomonas bacteriophage ΦKZ. J Mol Biol 425:2164-73.

17. Walker RA, O'Brien ET, Pryer NK, Soboeiro MF, Voter WA, Erickson HP, Salmon ED. 1988. Dynamic instability of individual microtubules analyzed by video light microscopy: rate constants and transition frequencies. J Cell Biol 107:1437-48.

18. Brouhard GJ, Stear JH, Noetzel TL, Al-Bassam J, Kinoshita K, Harrison SC, Howard J, Hyman AA. 2008. XMAP215 is a processive microtubule polymerase. Cell 132:79-88.

19. Ayaz P, Munyoki S, Geyer EA, Piedra FA, Vu ES, Bromberg R, Otwinowski Z, Grishin NV, Brautigam CA, Rice LM. 2014. A tethered delivery mechanism explains the catalytic action of a microtubule polymerase. Elife 3:e03069.

20. Brouhard GJ, Rice LM. 2018. Microtubule dynamics: an interplay of biochemistry and mechanics. Nat Rev Mol Cell Biol 19:451-463.

21. Mitchison T, Kirschner M. 1984. Dynamic instability of microtubule growth. Nature 312:237-42.

22. Zhang R, Alushin GM, Brown A, Nogales E. 2015. Mechanistic Origin of Microtubule Dynamic Instability and Its Modulation by EB Proteins. Cell 162:849-59.

23. Margolis RL, Wilson L. 2019. Microtubule treadmills—possible molecular machinery. Nature 293:705.

24. Shaw SL, Kamyar R, Ehrhardt DW. 2003. Sustained microtubule treadmilling in Arabidopsis cortical arrays. Science 300:1715-8.

25. Grego S, Cantillana V, Salmon ED. 2001. Microtubule treadmilling in vitro investigated by fluorescence speckle and confocal microscopy. Biophys J 81:66-78.

26. Rodionov V, Nadezhdina E, Borisy G. 1999. Centrosomal control of microtubule dynamics.

27. Rodionov VI, Borisy GG. 1997. Microtubule Treadmilling in Vivo.

28. Waterman-Storer CM, Salmon ED. 1997. Actomyosin-based retrograde flow of microtubules in the lamella of migrating epithelial cells influences microtubule dynamic instability and turnover and is associated with microtubule breakage and treadmilling. J Cell Biol 139:417-34.

29. Waterman-Storer CM, Salmon ED. 1997. Microtubule dynamics: Treadmilling comes around again. Current Biology 7:R369-R372.

30. Roohvand F, Maillard P, Lavergne JP, Boulant S, Walic M, Andreo U, Goueslain L, Helle F, Mallet A, McLauchlan J, Budkowska A. 2009. Initiation of hepatitis C virus infection requires the dynamic microtubule network: role of the viral nucleocapsid protein. J Biol Chem 284:13778-91.

Acknowledgements

Chapter 4, in full, has been submitted for publication in *Cell*, 2019. Chaikeeratisak, V., Khanna, K., Nguyen, K., Sugie, J., Egan, M., Erb, M.L., Vavilina, A., Nonejuie, P., Pogliano, K., Nieweglowska, E., Villa, E., Agard, D.A., Pogliano, J. (2019). Viral Capsid Trafficking along Treadmilling Tubulin Filaments in Bacteria. *Cell*. The dissertation author was a significant contributor to this paper.

Chapter 5: Additional Components of the Phage Nucleus Shell

Abstract

Recently we described the infection systems of jumbo *Pseudomonas* phages 201Φ2-1, ΦKZ, and ΦPA3. When these phages infect a bacterium, they reorganize the cell into a configuration resembling the eukaryotic nucleus. Viral DNA is enclosed by a proteinaceous structure along with proteins related to DNA and RNA processes. Host ribosomal proteins are excluded by this structure, as are metabolic enzymes. This compartment, called the phage nucleus, also interacts with the phage-encoded tubulin, PhuZ. The cytoskeletal element polymerizes into a bipolar spindle in the cell that pushes the phage nucleus to midcell using dynamic instability. Later in infection, the tubulin treadmills, which serves two purposes. Empty phage capsids traffic along the filaments to the phage nucleus where they are filled with viral DNA. In addition, the filaments rotate the nucleus so that each capsid can attach to an unoccupied surface position. Though major components of the phage nucleus system, including the main compartment proteins and the tubulins, are conserved among the three phages, differences exist between the systems. Here we explore components of the phage nucleus shell, some of which are conserved among the phages, and some of which diverge. Investigation into the proteins that make up the shell might give us greater insight into how these proteins evolved in these phage genomes. In addition, we may be able to determine how the phages use these compartments to recognize and sort proteins.

Introduction

Eukaryotic cells are organized spatially and functionally into organelles, including the nucleus, mitochondria, and the Golgi apparatus. The majority of eukaryotic organelles are specialized and bound by their own membranes. The compartmentalization of different functions prevents diffusion by sequestering enzymes and molecules needed for certain processes as well as preventing toxins from going where they are not wanted. Bacteria generally lack the membrane bound organelles but utilize other methods for compartmentalization within the cell. When nutrients are low, *Bacillus subtilis* encapsulates its DNA in an endospore that can lie dormant for centuries, resistant to antibiotics and dehydration. During this process, a *Bacillus* cell creates the forespore with additional cell wall synthesis then engulfs it with the cellular membrane [88]. Some phototropic bacteria contain chromatophores, invaginations of the cell membrane that contain pigments for photosynthesis. Magnetotactic bacteria use lipid-bound magnetosomes containing iron compounds for interaction with the earth's magnetic fields [89]. Bacterial microcompartments (BMCs) are also found in a variety of bacteria with a variety of functions. BMCs are comprised of a single selectively permeable protein shell that self-assembles in the cell around an enzyme core. Carboxysomes, for example, are anabolic microcompartments encapsulating Rubisco for fixation of carbon dioxide [90].

Similarly, the protein-bound phage nucleus was first discovered in the 316kb phage 201Φ2-1, which infects *Pseudomonas chlororaphis*. The major component of the phage nucleus shell is gp105, which a proteomics study identified as the earliest and most highly expressed phage protein [71]. When fused to a fluorescent protein, gp105

formed a spherical compartment that enclosed phage DNA. In cross-section, the fluorescent fusion appeared as a ring, encircling the DNA nucleoid. CryoEM tomography showed that the phage nucleus border was apparently continuous with no visible openings or pores. The border was approximately 5nm, which is thinner than the cellular membrane. The shell appears to be made entirely of protein, as neither cryo-EM nor fluorescent membrane dyes, identified any membrane in the structure. The major shell proteins were conserved in the genomes of the related *Pseudomonas aeruginosa* phages ΦPA3 and ΦKZ as gp53 and gp54, respectively [62]. Fluorescent microscopy and cryo-EM of these phages showed no major differences in their phage nucleus compartments [62].

In our systematic localization of phage encoded proteins, we encountered two sets of proteins that show the same phenotype as the major shell proteins. Fluorescent fusions to these proteins formed spherical compartments around the phage DNA, suggesting that these proteins might also be part of the phage compartment structure. The second largest protein encoded by phage 201Φ2-1 is gp230 at 155.8kDa. 201Φ2-1gp230 is conserved in the other two phages, although as multiple, overlapping genes. The protein shows 51% identity to KZgp145 and 27% to KZgp146. An SDS-page gel identified gp230 as a uncleaved component of the 201Φ2-1 virion [18]. The presence of a collagen-like domain suggests that gp230 functions as a tail protein or tail fiber. KZgp145 has also been identified as an abundant virion protein [24]. A stretch of proteins from ΦPA3 were also identified as homologous to KZgp145 and KZgp146 [23]. PA3gp165-9 were annotated as components of the tail, including tube and sheath. While

gp230 and its homologs have been investigated previously, no work has been done on the second set of proteins. These homologous proteins are annotated as gp2 in each phage. They are located in a large stretch of homology between all three phages, which also contains the enzyme dihydrofolate reductase and the conserved protein family DUF1353/pfam07087, whose function is unknown [23].

Investigating these additional components of the phage nucleus shell will give us greater insight into the shell itself. We may be able to identify mechanisms of protein transport or sorting. In addition, studying these proteins may answer a number of evolutionary questions, such as how the shell evolved in these phages or how related these systems are.

Results

An alignment of the homologous proteins showed that gp230 has homology to KZgp145 and KZgp146 as well as PA3 proteins gp164, gp165, gp166, gp167, and gp169 (Figure S1).

A fluorescent fusion to gp230 appears as a ring around the viral DNA nucleoid in cross-section (Figure 1A). We also performed fluorescence recovery after photobleaching (FRAP) experiments to determine if the protein was stable. Timelapse microscopy following photobleaching indicated that gp230 is highly dynamic, with the structure recovering in less than a second (Figure 1B). In a co-expression fusion with the major shell protein gp105, gp230 appears to co-localize with gp105 after infection (Figure 1C). In addition, timelapse microscopy from the beginning of infection shows that the proteins are co-localized from early stages of infection. They appear together

as a small focus near the cell pole that grows in size as it is pushed to midcell (Figure 1D). Although homologs of gp230 exist in the other two phages, fluorescent fusions to the ΦPA3 or ΦKZ homologs do not show the ring phenotype (Figure 1E).

The gp2 proteins from all three phages, 201Φ2-1, ΦKZ, and ΦPA3, are conserved, with about 29% identity shared (Figure 1S). When the gp2 proteins from 201 and PA3 are fused to sfGFP, both fluorescent fusions form a spherical shape around the viral DNA (Figure 2A). However, KZgp2 lacks the same phenotype, failing to form a ring during infection (data not shown). The PA3 and 201 proteins appear to be conserved enough to be functional in cross-infection. We express fluorescent fusions to phage proteins on an arabinose inducible plasmid in the host bacterium before infection. In uninfected cells, the fluorescence is usually diffuse but after infection, we can observe the localization of the fluorescent proteins. When the gp2 of one phage is expressed in a cell which is subsequently infected with a different phage, the fluorescent ring still assembles. Specifically, when PA3gp2 is expressed on a plasmid in a *P. chlororaphis* cell and infected with 201Φ2-1, a fluorescent ring is visible in infected cells. The reverse is also true – *P. aeruginosa* cells expressing the 201gp2 and infected with ΦPA3 also show a fluorescent ring (Figure 2B). In a co-expression fusion, 201gp2 colocalizes with the major shell protein 201gp105 (Figure 2C). In addition, timelapse microscopy following laser ablation indicates that PA3gp2 is highly dynamic, recovering almost immediately after FRAP (Figure 2D).

Discussion

The evidence indicates that gp230 is a tail protein. The protein is present in proteomics performed on phage lysates, indicating that it is present in the mature virion. Gp230 contains a collagen domain, which is commonly found in phage tail proteins. In addition, the homologous proteins in the other two phages are annotated as tail proteins. However, none of the homologs in phages ΦKZ or ΦPA3 appear to make the ring phenotype associated with the shell. It is possible that 201Φ2-1 simply constructs a different shell, perhaps with more components than the other two phages. In addition, gp230 may serve dual functions. The protein could form a compartment either around the major shell protein or with it, but gp230 may serve as a docking place where the capsids attach for DNA packaging. Gp230 could act as a portal protein that the capsids bind to and when they leave for further maturation in the cytoplasm, gp230 goes with them.

The function of gp2 is phages ΦPA3 and 201Φ2-1 is even more unclear. The proteins have no homology to any other bacterial or phage proteins with known function, although they do appear to be conserved in some related phages from the ΦKZ family. PA3gp2 shares 28.57% identity to 201gp2 and 29.12% identity with KZgp2. However, KZgp2 does not share the shell phenotype. Though the identity shared between PA3gp2 and 201gp2 is still relatively low, the phenotype is conserved between the two. Moreover, it appears that one phage can either use the other phage's gp2 or that the proteins are similar enough to co-assemble. Only one other protein, the RecA/UvsX-like protein, has shown this ability to conserve its phenotype and possibly its function in

cross-infection [62]. The highly dynamic properties of these additional shell proteins are also in contrast to gp105 which did not recover after FRAP. It is possible the dynamic proteins form an outer coat that envelops gp105 along with the viral DNA or that gp105 forms a stable scaffold for the other components of the phage nucleus.

Identifying additional proteins that make up the phage nucleus will give us insight into this novel structure. By determining exactly how many proteins comprise the compartment, we can establish how these proteins fit and work together. We may be able to figure out the method of protein sorting and transport once we have elucidated the full structure of the phage nucleus.

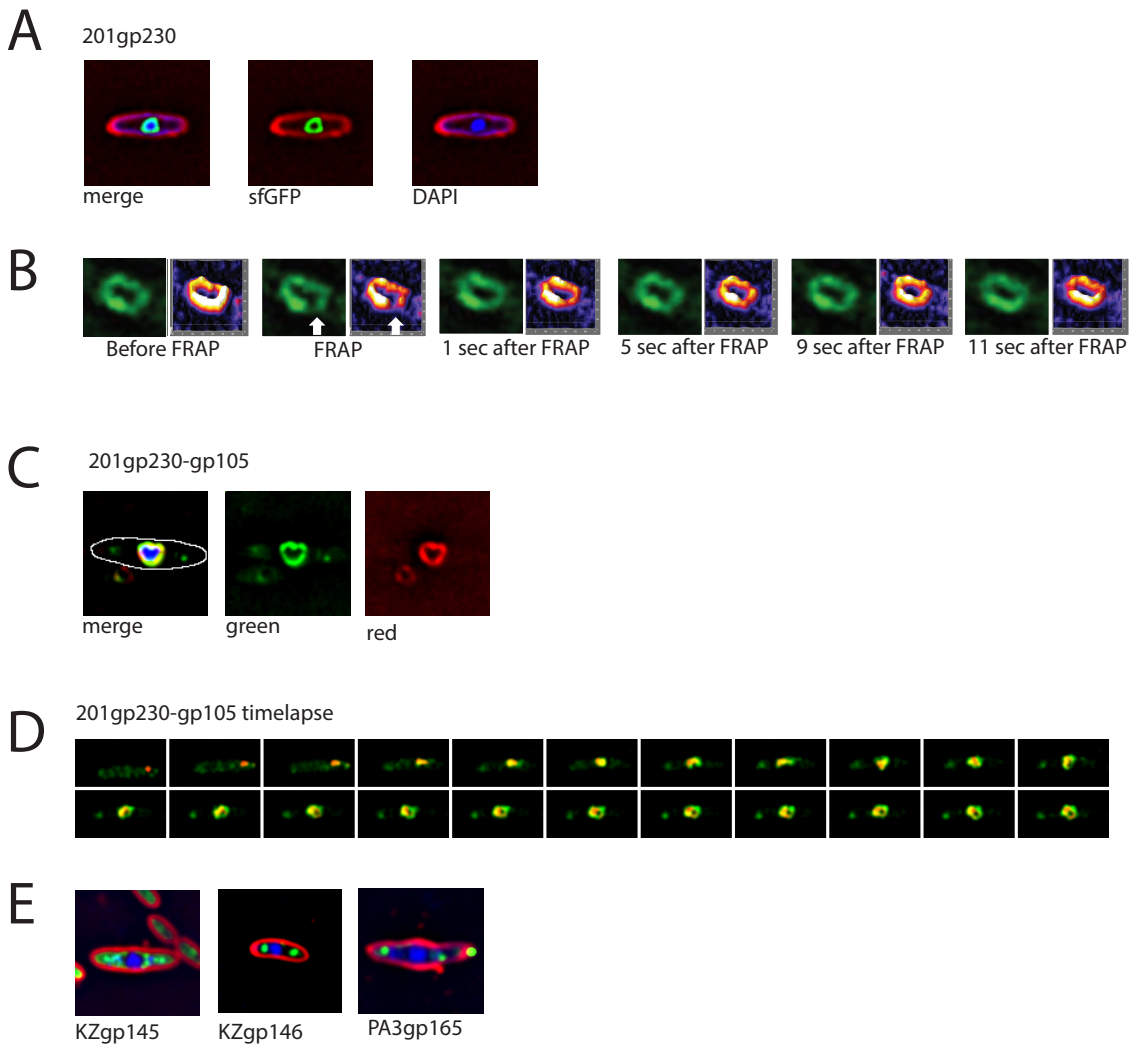

Figure 5.1: gp230 forms a dynamic shell around viral DNA that colocalizes with the major compartment protein, gp105.

A. 201gp230-GFP forms a ring around viral DNA after infection
B. Fluorescence recovery after photobleaching (FRAP) of the gp230-GFP structure shows nearly instantaneous recovery after laser event. Heat maps to the right of the images indicate GFP intensity.
C. When gp230-GFP is co-expressed with the major shell protein gp105, they appear to co-localize in a ring around the viral DNA.
D. Timelapse of the co-expression show that gp230 and gp105 are co-localized from the early stages of infection. Timelapse begins at 15 minutes post infection.
E. Homologs to gp230 in phages ΦPA3 and ΦKZ are annotated as tail proteins and do not form a ring. The shell phenotype is not conserved in these homologs.

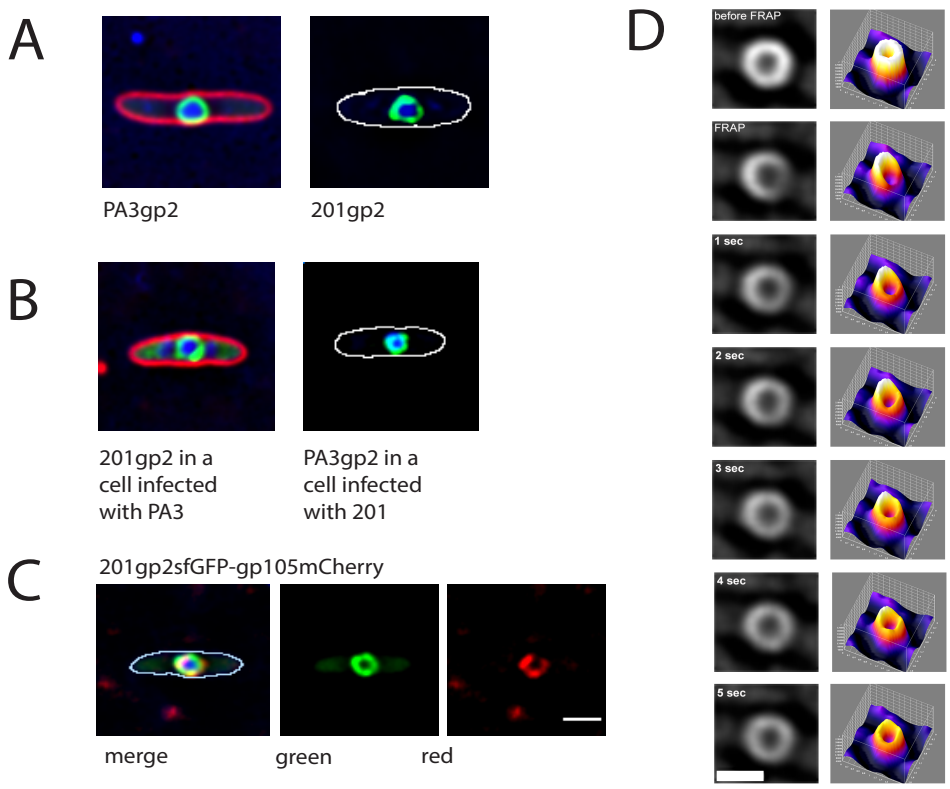

Figure 5.2: PA3gp2 and 201gp2 form a dynamic ring around viral DNA after phage infection.

A. 201gp2-GFP and PA3gp2-GFP form rings around viral DNA after infection.
B. Both PA3gp2 and 201gp2 retain the ring phenotype after cross-infection. 201gp2 expressed in *P. aeruginosa* before infection forms the ring upon infection with ΦPA3. PA3gp2 also assembles a ring when expressed in a *P. chlororaphis* cell infected with 201Φ2-1.
C. 201gp2 fused to sfGFP colocalizes with the major shell protein 201gp105 fused to mCherry.
D. Fluorescence recovery after photobleaching (FRAP) of the PA3gp2-GFP structure shows nearly instantaneous recovery after laser event. Heat maps to the left of the images indicate GFP intensity.

```
CLUSTAL O(1.2.4) multiple sequence alignment


164      ---MAKATKISEYEILTELTGDEYVEVIAPTPEGEQPFKNYRVSTAKF---GMGKSAYEL   54
230      MADQKKAGMISGMSPLAVLTGDELMEVSSRQPDGS--WKTFSIIVSKIRT-NAGLSAYEV   57
145      MANVTDKGKISQLPDLATLNDSEYIELIHTDAAGQ--VDNYKFPLSKLQTGAPGLSAYEI   58
165      MAANPNPGMISQMPSLNIVTGEEFLEVIKRETDGS--YKNYRLMVSKIRT-NEGLSAYEV   57
169      ------------------------------------------------------------   0
146      ------------------------------------------------------------   0
166      ------------------------------------------------------------   0
167      ------------------------------------------------------------   0


164      AVEGGYTGTQEEWLASLQGESAYQIAVKYGYTGSEAEWNAVFDTIYIRDASSAGKILVVG   114
230      AVVNGFVGTQAEWLESLNGKSAYQVAVELGYVGTEAEWLESLVG---KSAY--EDAVAQG   112
145      AVKNGFQGTETEWLDSLKGKSSYQIAVDLGFVGTEEEFIASLKGDAGKSAY--EVAVENG   116
165      AVKNGFVGTEQEWLDSLQGKSIYQLALEHGFVGSEQEYLDSLKGEAGKSAY--QTAVDEG   115
169      ------------------------------------------------------------   0
146      ------------------------------------------------------------   0
166      ------------------------------------------------------------   0
167      ------------------------------------------------------------   0


164      TAG-TPEWQALTKTRVGLDQVD-N-----TAD------------ADKPISN----------   146
230      YNGTLSEWLNSLKGQSAYQIAVANGFVGTEAAWLESLKGQSAYQLAKIIDPTVGTEEEWL   172
145      FQGTEQEWLTSLH-------------------------------------------------   129
165      YTGTEAQWLQTLVGQSAYDIAVEQGFVGDKDAWLASLKGEKGD-----------------   158
169      ------------------------------------------------------------   0
146      ------------------------------------------------------------   0
166      ------------------------------------------------------------   0
167      ------------------------------------------------------------   0


164      ------------------------------------------------AVAVALASKADLG   159
230      ATLVGKSAYQVALDNGFVGTEAAWLKSLEGKSSYQVWLSIPGNEDKTEVEFIEAITGQQG   232
145      ------------------------------------------------------------   129
165      ------------------------------------------------------------   158
169      ------------------------------------------------------------   0
146      ------------------------------------------------------------   0
166      ------------------------------------------------------------   0
167      ------------------------------------------------------------   0


164      EDGKINPEQ---LPASTAPVAATV----------EEVLEGVDNTKFITAETVFALLA---   203
230      EDGKSAYEVWVELPGNAGKTEAEFFESLKGEGMTQAKLQELLDLGYYTTEGKFVVKGTNS   292
145      -------------------------------ATMTAELLQSLLNQQGYTVKDVLRVTGKNG   159
```

Figure S5.1: An alignment of 201gp230 to proteins from PA3 (gp164, 165, 166, 167, and 169) and KZ (gp 145, 146) show that 201gp230 has homology to a number of smaller, sequential proteins in the other two phages.

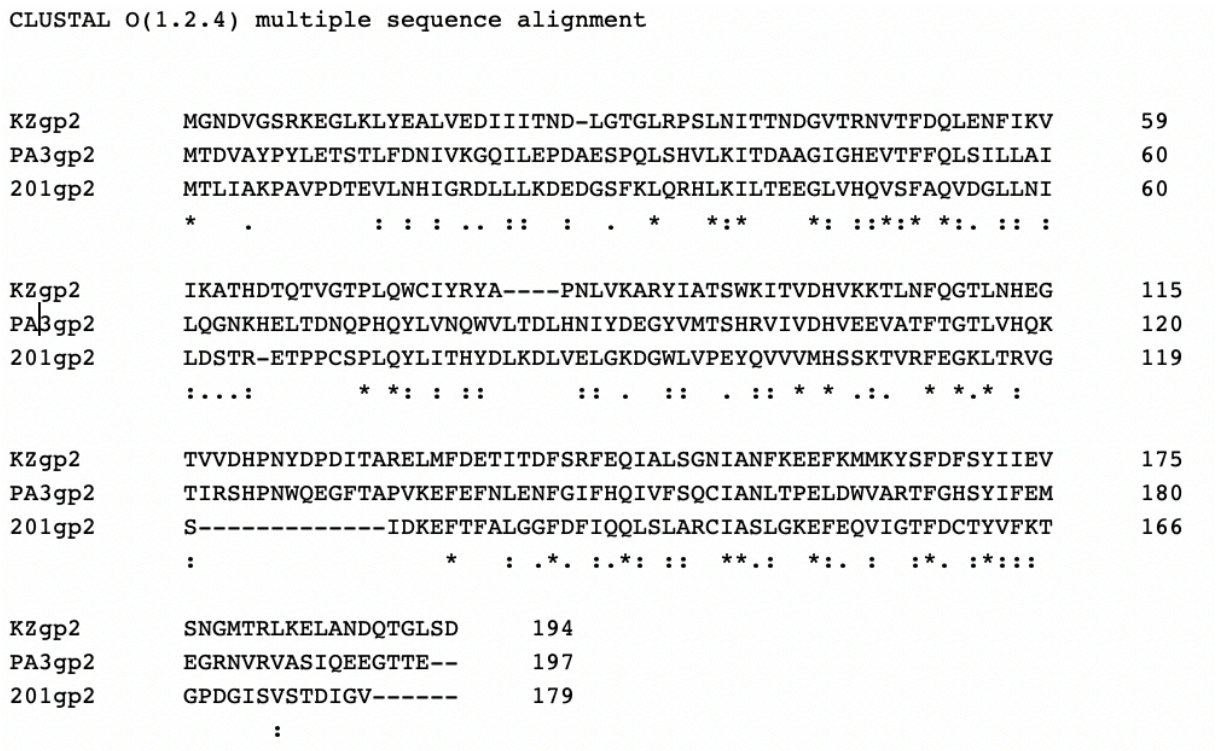

Figure S5.2: An alignment of the gp2 protein from phages 201Φ2-1, ΦKZ, and ΦPA3. Though KZgp2 has homology to the other proteins, it does not retain the same shell phenotype.

Table 5.1: Strains and plasmids used in this study

KN042	*E.coli - DH5α*	pKN013	GP230 from 201phi2-1 genome and C-terminal GFPmut1
KN043	*Pseudomonas chlororaphis*	pKN013	GP230 from 201phi2-1 genome and C-terminal GFPmut1
KN058	*E.coli - DH5α*	pKN021	C-terminal GFPmut1 and 201phi2-1 GP230; N-terminal mCherry and 201phi2-1 GP105
KN059	*Pseudomonas chlororaphis*	pKN021	C-terminal GFPmut1 and 201phi2-1 GP230; N-terminal mCherry and 201phi2-1 GP105
KN115	*E.coli - DH5α*	pKN045	C-terminal GFPmut1 and GP146 from phiKZ genome
KN117	*Pseudomonas aeruginosa (PA01)*	pKN045	C-terminal GFPmut1 and GP146 from phiKZ genome
KN152	*E.coli - DH5α*	pKN054	N-terminal GFPmut1 and GP165 from PA3 genome
KN154	*Pseudomonas aeruginosa (PA01)*	pKN054	N-terminal GFPmut1 and GP165 from PA3 genome
KN385	*E.coli - DH5α*	pKN127	C-terminal sfGFP and gp2 from PA3 genome
KN386	*Pseudomonas chlororaphis*	pKN127	C-terminal sfGFP and gp2 from PA3 genome
KN387	*Pseudomonas aeruginosa (PA01)*	pKN127	C-terminal sfGFP and gp2 from PA3 genome
KN418	*E.coli - DH5α*	pKN138	C-terminal sfGFP and gp2 from 201 genome
KN419	*Pseudomonas chlororaphis*	pKN138	C-terminal sfGFP and gp2 from 201 genome
KN420	*Pseudomonas aeruginosa (PA01)*	pKN138	C-terminal sfGFP and gp2 from 201 genome
KN456	*E.coli - DH5α*	pKN150	201gp2-sfGFP and 201gp105-mCh co-exp
KN457	*Pseudomonas chlororaphis*	pKN150	201gp2-sfGFP and 201gp105-mCh co-exp
KN458	*Pseudomonas aeruginosa (PA01)*	pKN150	201gp2-sfGFP and 201gp105-mCh co-exp
KN472	*K2733 - PA01 pump knockout*	pKN150	201gp2-sfGFP and 201gp105-mCh co-exp
KN513	K2733 - PA01 pump knockout	pKN166	C-terminal sfGFP and gp146 from PhiKZ genome
KN514	*E.coli - DH5α*	pKN167	C-terminal sfGFP and gp145 from PhiKZ genome
KN515	*K2733 - PA01 pump knockout*	pKN167	C-terminal sfGFP and gp145 from PhiKZ genome

References

1. Cornejo E, Abreu N, Komeili A. 2014. Compartmentalization and Organelle Formation in Bacteria. Curr Opin Cell Biol 26:132-8.

2. Grant CR, Wan J, Komeili A. 2018. Organelle Formation in Bacteria and Archaea. Annu Rev Cell Dev Biol 34:217-238.

3. Kerfeld CA, Aussignargues C, Zarzycki J, Cai F, Sutter M. 2018. Bacterial microcompartments. Nat Rev Microbiol 16:277-290.

4. Chaikeeratisak V, Nguyen K, Khanna K, Brilot AF, Erb ML, Coker JK, Vavilina A, Newton GL, Buschauer R, Pogliano K, Villa E, Agard DA, Pogliano J. 2017. Assembly of a nucleus-like structure during viral replication in bacteria. Science 355:194-197.

5. Chaikeeratisak V, Nguyen K, Egan ME, Erb ML, Vavilina A, Pogliano J. 2017. The Phage Nucleus and Tubulin Spindle Are Conserved among Large Pseudomonas Phages. Cell Rep 20:1563-1571.

6. Thomas JA, Rolando MR, Carroll CA, Shen PS, Belnap DM, Weintraub ST, Serwer P, Hardies SC. 2008. Characterization of Pseudomonas chlororaphis myovirus 201varphi2-1 via genomic sequencing, mass spectrometry, and electron microscopy. Virology 376:330-8.

7. Mesyanzhinov VV, Robben J, Grymonprez B, Kostyuchenko VA, Bourkaltseva MV, Sykilinda NN, Krylov VN, Volckaert G. 2002. The genome of bacteriophage phiKZ of Pseudomonas aeruginosa. J Mol Biol 317:1-19.

8. Monson R, Foulds I, Foweraker J, Welch M, Salmond GP. 2011. The Pseudomonas aeruginosa generalized transducing phage phiPA3 is a new member of the phiKZ-like group of 'jumbo' phages, and infects model laboratory strains and clinical isolates from cystic fibrosis patients. Microbiology 157:859-67.

Chapter 6: Forcing selective transport into the phage nucleus

Katrina T. Nguyen[1], Joseph Sugie[1], Kanika Khanna[1], MacKennon E. Egan[1], Christopher Beierschmitt[1], Elizabeth Villa[1], Joe Pogliano[1*]

Abstract

Upon infection of *Pseudomonas* cells, jumbo phages 201Φ2-1, ΦPA3, and ΦKZ assemble a phage nucleus. Viral DNA as well as proteins associated with both DNA replication and RNA transcription are enclosed within a proteinaceous shell. Proteins involved in metabolic processes and translation, including host ribosomes, are excluded from the nucleus. As a result of this compartmentalization, RNA synthesis occurs inside the phage nucleus but messenger RNA must be transported into the cytoplasm to be translated. Many of the newly synthesized proteins, such as those involved in DNA replication, repair, or gene expression, specifically translocate into the nucleus. The molecular mechanisms governing protein sorting and import are currently unclear. To gain insight into this process, we studied the localization of five reporter fluorescent proteins (pMutinGFP, sfGFP, GFPmut1, mCherry, CFP). During infection with PA3 or 201, all five fluorescent proteins were excluded from the nucleus in unless fused to a nuclear targeted protein; however, we have discovered one anomaly with the ΦKZ nuclear transport system. The fluorescent protein GFPmut1 expressed by itself was transported into the ΦKZ phage nucleus. In addition, fusing GFPmut1 to any protein, including proteins that normally reside in the cytoplasm, results in transport of the fusion into the nucleus. Although the mechanism of transport is still unclear, we demonstrate

that GFPmut1 is a useful tool that can be used for fluorescent labelling and targeting of proteins into the ΦKZ phage nucleus.

Introduction

Protein localization within a cell is directly linked to many cellular processes, such as cell division and growth. Targeting of proteins to intracellular destinations is essential in all organisms. Generally, eukaryotes use a sorting sequence to target proteins to specific organelles, such as a nuclear localization signal to send proteins to the nucleus or an N-terminal signal peptide to target proteins to the ER. Additional sequences are known to target proteins even more specifically to regions within an organelle. These signal sequences are usually highly conserved, even among different species. Though bacteria lack the membrane-bound organelles of eukaryotes, bacterial cells are still highly organized and require targeting of proteins either extracellularly or to specific intracellular locations. Bacteria utilize a number of protein sorting strategies simultaneously. For proteins secretion from the cytoplasm, a signal sequence directs unfolded proteins to the SecYEG pore where secretion is powered by the ATPase SecA and the proton motive force (1). In contrast, the TatA system exports fully folded proteins across the plasma membrane after recognizing a pair of arginine resides at the C-terminus (2).

We recently described the phage nucleus assembled by jumbo phages 201Φ2-1, ΦPA3, and ΦKZ during infection of *Pseudomonas* cells (3, 4). During infection, proteins synthesized by bacterial ribosomes in the cytoplasm appear to be sorted to specific destinations in the cell based on their biological functions. Both host and phage-encoded proteins involved in DNA replication, repair, and transcription localize inside the nucleus,

while proteins involved in metabolic processes and protein synthesis localize in the cytoplasm outside the nucleus. Time-lapse microscopy experiments show that proteins already synthesized and fully folded before phage infection accumulate in the nucleus over the course of 30 minutes, suggesting a mechanism exists for posttranslational nuclear protein import (4). How such proteins are selected for intracellular transport and the mechanism by which it occurs are still unknown.

One of the barriers to understanding this phenomenon is the lack of tools to genetically manipulate the phage DNA. In order to develop such tools, we sought to establish a method by which we can specifically target gene-editing proteins into the shell. Here, we report our newfound ability to target proteins into the nucleus of ΦKZ phage. Although the ΦKZ nucleus appears to be largely similar to that of phages ΦPA3 and 201Φ2-1, we surprisingly found that it naturally imports the fluorescent protein GFPmut1, but not any of the other tested fluorescent proteins. In addition, any protein fused to GFPmut1 will also be targeted for transport into the ΦKZ nucleus. We have serendipitously discovered a mechanism to target proteins into the shell, providing a reliable method for delivering specific proteins into the ΦKZ nucleus for the first time.

Results

During our investigation of comparative protein localization during phage infection among the three different phages (ΦPA3, ΦKZ, 201Φ2-1), we noticed a discrepancy in protein localization. All fluorescent protein controls (GFPmut1, pMutinGFP, sfGFP, mCherry, and CFP) localized in the cytoplasm of ΦPA3 and 201Φ2-1 as expected. Four of these proteins, GFP, sfGFP, mCherry, and CFP were also localized in the cytoplasm

of ΦKZ infected cells as expected (Figure 1A). However, GFPmut1 localized to the ΦKZ nucleus even though it was excluded by the 201Φ2-1 nucleus in *P. chlororaphis* and that of ΦPA3 in *P. aeruginosa* (Figure 1B). Since each of these proteins was expressed by itself, unfused to any other proteins, this suggests that difference in localization is caused by variances in either the fluorescent proteins, the phage transport systems, or both.

Studying nearly identical fluorescent proteins with strikingly different localization might provide insight into nuclear targeting. Comparison of the protein sequences of these fluorescent proteins revealed several amino acid differences (Figure 1C) which could be responsible for the differential localization. We identified three amino acids where GFPmut1 differed from the other proteins tested (Figure 1, S1)(5-7). In the protein structure, phenylalanine (F99) and methionine (M153) both extended outward from one face of the GFP, while valine (V163) is along the same surface but facing inward toward the beta barrel (Figure 2A). To determine which of these mutations might influence import into ΦKZ, we used site-directed mutagenesis to individually mutate each amino acid to that found in versions of GFP that remained in the cytoplasm (sfGFP and pMutin). GFPmut1 with the V163T mutation (n=82) retained the same localization as the unaltered GFPmut1 (n=111), inside the nucleus. However, the F99S mutation resulted in exclusion from the nucleus in 100% of cells (n=177) (Figure 2B, 2C). The M153T mutation partially altered GFP localization, with some of the cells showing the fluorescent protein excluded from the nucleus, some showing full inclusion, and some showing an indistinct localization, with GFP both inside and outside the nucleus (n=115) (Figure 2B, 2C). These results suggest that the amino acids on the surface of GFP could contribute to its

selective protein import.

Knowing that the soluble GFPmut1 could be transported into the nucleus, we attempted to test the ability of the fluorescent protein to ferry other proteins into the compartment along with it. As shown previously using fluorescence microscopy and cryoEM, bacterial ribosomes are excluded from the nucleus (4). For example, ribosomal subunit L28 tagged with mCherry is excluded from the phage nucleus (Figure 3A). However, tagging the same subunit with GFPmut1 results in its localization inside the nucleus. Similarly, when tagged with sfGFP, the tail protein of ΦKZ, gp146, shows puncta outside the nucleus where it would be expected to assemble with mature virions. Strikingly, fusions of gp146 to GFPmut1 localize inside the nucleus. ΦKZ will even import proteins from other phages when they are tagged with GFPmut1. When tagged with mCherry, PA3PhuZ forms filaments in the cytoplasm of a cell infected by ΦKZ. However, when fused to GFPmut1, PA3PhuZ is localized inside the ΦKZ phage nucleus (Figure 3A).

To further test the abilities of GFPmut1 to force localization into the nucleus, we created two fusions of mCherry to both the N and C terminal ends of GFPmut1 (mCherry-GFPmut1 and GFPmut1-mCherry). This allowed us to determine if the GFPmut1 localization was based on the location of the fluorescent tag. Both fusions were transported into the nucleus, indicating that the position of the GFPmut1 tag made no difference (Figure 3B). In time-lapse microscopy, mCherry-GFPmut1 was visibly fluorescent in the cytoplasm before infection as well as in the nucleus post-infection suggesting that the protein is already fully folded upon transport (Figure 3C).

Given the unique ability of the ΦKZ phage nucleus to import GFPmut1, we used cryo-EM to confirm that this phage assembles a nucleus-like structure similar to ΦPA3 and 201Φ2-1. *P. aeruginosa* was infected for 60 minutes with ΦKZ, plunge frozen in liquid ethane, and processed for FIB milling and cryo-ET. We found that the subcellular organization of ΦKZ infected cells were identical to those of 201Φ2-1 and ΦPA3. The protein shell of the nucleus forms an unstructured, largely continuous border with a thickness of approximately 5nm (Figure 4A). Phage at various stages of maturation were observed, including capsids attached to the side of the nucleus that were either empty or filled with viral DNA, as well as phage tails, some of which were attached to capsids. Bacterial ribosomes were clearly excluded from the phage nucleus compartment as in PA3 and 201. These results confirm and extend our fluorescence microscopy experiments (3, 4) showing that, despite the differences in their ability to import GFPmut1, the phage replication and assembly pathway is conserved among all three phages.

We next attempted to use GFPmut1 to bring in proteins that might disrupt phage replication. The host protein sbcB is a single-stranded DNA nuclease that likely functions in host DNA recombination and repair(8). Inducing expression of sbcB reduces cell growth, compared to either cells expressing only GFPmut1 or uninduced sbcB strains (Figure 5A). When microscopy was performed on sbcB-sfGFP, the fusion was visible in the cytoplasm, excluded from the phage nucleus. However, when SbcB was then fused to GFPmut1, fluorescence was observed localized inside the phage nucleus (Figure 5B). Quantitation of the DAPI intensity of the infection nucleoid in both strains showed that infected SbcB-mut1 cells had a lower average DAPI intensity compared to sbcB-sfGFP,

suggesting that internalization of SbcB-mut1 reduces DNA replication or enhances its degradation (Figure 5C). When comparing cells expressing sbcB-GFPmut1 to the sbcB-sfGFP counterpart, ΦKZ replication was reduced approximately 10-fold (Figure 5D). Fusions of sfGFP to nucleases from three different CRISPR systems, cas3, cas9, and cas13, indicate that the natural phenotype of these proteins is exclusion from the nucleus. However, tagging them with GFPmut1 brings them into the nucleus (Figure 5E).

Discussion

Our major finding is that the fluorescent protein GFPmut1, and any fusion made with GFPmut1, is transported into the ΦKZ phage nucleus. However, this phenotype is not seen in the infection systems of the two related phages ΦPA3 and ΦKZ. We had previously discussed the high degree of similarity between these three related jumbo *Pseudomonas* phages, namely that they all construct a proteinaceous phage nucleus centered in an infected cell by PhuZ filaments (3). However, these results suggest that these phages and their infection systems may be more divergent than first thought. Though the cryoEM tomogram shows us a ΦKZ nucleus that appears to be identical to that of its related phages, the GFPmut1 localization suggests that there must be at least one difference in methods of transportation into the nucleus. The lack of a visible phenotypic difference in the cryo-tomogram of a ΦKZ infected cell suggests that this difference is more likely to be a mechanistic difference than a physical one.

It remains unclear why GFPmut1 is able to target proteins to the ΦKZ nucleus. A single amino acid change (F99S) is able to prevent localization to the nucleus. One hypothesis is that some sort of protein recognition allows transport into the nucleus. The

positions of the mutations which have an effect on localization (F99S, M153T) on the outer surface of GFPmut1 imply a recognition of the folded structure as opposed to the unfolding primary sequence. The fluorescence of both GFPmut1 and mCherry prior to localization within the phage nucleus supports this idea as well. However, the genome of ΦKZ shows no homology to any transporter proteins or chaperone proteins. Given the high divergence of the proteins in the phage genomes, it is likely that any transport system used would be greatly different from that seen in bacteria or other organisms.

In addition to localization of the soluble GFPmut1, we found that any protein fused to GFPmut1 will be transported into the phage nucleus as well. The mCherry-GFPmut1 fusions suggest that at least some of the proteins maintain their folding and functionality throughout the fusion and localization process. The unexpected finding of GFPmut1 nuclear targeting raised the possibility that we might be able to use this protein as a convenient way to both label and target proteins to the nucleus in ΦKZ. Understanding which fluorescent proteins are localized outside the ΦKZ nucleus versus which ones are imported, is critical for studies of protein localization and will allow us to develop valuable tools for future studies. These tools will allow us to tag proteins with different colors to visualize their native localization as well as to artificially manipulate protein localization by forcing their nuclear import. These results suggest that we can use three different colors of fluorescent proteins (blue, CFP; red, mCherry; or green, sfGFP, pMutinGFP, and GFPmut1) to localize proteins during ΦKZ infection, and that we can use GFPmut1 as a tool to specifically target proteins into the nucleus.

Using GFPmut1 to manipulate the ΦKZ nucleus gives us the ability to target and possibly edit phage DNA. Previous attempts to modify the DNA of these large phages have failed, most likely because of the physical protein afforded to the DNA by the nuclear shell. We have previously hypothesized that the phage nucleus serves to protect phage DNA against host defenses, such as CRISPR and restriction enzymes, as well as other stressors. GFPmut1 targeting will allow us to circumvent the nucleus. Creating mutant phage with this method will let us greatly expand our scope of study in these large phages. Further studies of this targeting phenomenon will also give us insight into the methods utilized by phage ΦKZ for protein sorting. Though the mechanisms used by ΦKZ may differ from the other two phages, determining the specific differences will shed light on the transport systems of the phage nucleus as well as the relationships between these phages. Once we understand the system, we may be able to manipulate it to allow us to target the nucleus in the other phages as well. In addition, further investigation of this import phenomenon could lead to understanding of the transport mechanisms in this primitive nucleus system.

Experimental Procedures

Strain, growth condition, and bacteriophage preparation

Pseudomonas chlororaphis strain 200-B was grown on Hard Agar (HA) containing 10 g Bacto-Tryptone, 5 g NaCl, and 10 g agar in 1L ddH_2O and incubated at 30°C overnight. *Pseudomonas aeruginosa* strains PA01 and PA01-K2733 (pump-knockout strain) were grown on Luria-Bertani (LB) media containing 10g Bacto-Tryptone, 5g NaCl, 5g Bacto-yeast extract in 1L ddH_2O and incubated at 30ºC overnight. Lysates for phages 201Φ2-1 and ΦPA3 were made by infecting respective saturated host cultures with 10μl of high titer lysate, incubating for 15 minutes at room temperature, mixing with HA top agar (0.35%; phage 201Φ2-1) or LB top agar (0.35%; phage ΦPA3) and pouring over corresponding HA or LB plates. Plates were incubated at 30ºC overnight. Plates that formed web-lysis were then flooded with 5mL of phage buffer and incubated at room temperature for 5 hours. The phage lysates were then aspirated, clarified by centrifugation at 15,000 rpm for 10 minutes, and stored at 4°C with 0.01% chloroform by volume.

Plasmid constructions and bacterial transformation

Fluorescent-tagged phage proteins were constructed with the pHERD30T vector as a backbone. Phage genes were PCR amplified from phage lysates then ligated into the pHERD30T backbone with via isothermal assembly. The assemblies were electroporated into DH5α *E. coli* and plated on LB supplemented with gentamycin sulfate (15μg/mL). Constructs were confirmed with sequencing and subsequently electroporated into either *P. chlororaphis* strain 200-B or *P. aeruginosa* strains PA01 and/or PA01-

K2733. *P. chlororaphis* strain was grown on HA supplemented with gentamycin sulfate (25*μ*g/mL) and *P. aeruginosa* strains PA01 and PA01-K2733 were grown on LB supplemented with gentamycin sulfate at 300 *μ*g/mL or 15*μ*g/mL, respectively. See Supplemental Table 1 for a list of plasmids and strains.

Fluorescent Microscopy

The bacterial cells were grown on 1% agarose pads in glass well slides, containing 25% LB, 1ug/mL FM4-64, 1ug/mL DAPI, and 0.1-0.5% arabinose to induce protein expression at desired levels. These pad slides were incubated at 30°C for 3 hours in a humid chamber. For infection beginning at timepoint 0, 5-10 µl of high-titer lysate (10^{10} pfu/ml) was added to pads then incubated again at 30°C. At desired time points after phage infection, a coverslip was put on the slide and fluorescent microscopy performed. Data of static images and time-lapse imaging were collected and processed as described below.

Tomography Sample Preparation and Data Acquisition

Infection of *P. aeruginosa* cells with phage ΦKZ was done as indicated above. At 70 mpi, cells were scraped off from the surface of the pad using ¼ LB media. 7 *μ*l of cells were deposited on holey carbon coated QUANTIFOIL® R 2/1 copper grids that were glow discharged using Pelco easiGlow™ glow discharge cleaning system. Manual blotting from the side of the grid opposite to the cells using Whatman No. 1 filter paper removed excess liquid such that cells form a monolayer on the surface of the grid. Cells were then plunge-frozen in a mixture of ethane/propane using a custom-built vitrification device (Max Planck Institute for Biochemistry, Munich). Grids were then mounted into modified

FEI Autogrids™ to avoid any mechanical damage to the delicate grids during subsequent transfer steps. Then, these clipped grids were transferred into Scios (Thermo Fisher Scientific, formerly FEI), a dual-beam (cryo-FIB/SEM) microscope equipped with a cryogenic stage. Thin sections of 100-250 nm, or lamellae, were prepared as previously described in Chaikeeratisak et al., 2017 containing 10-12 cells each. Tilt-series were collected from typically -65° to +65° with 1.5° or 2° tilt increments using SerialEM[4] in a 300-keV Tecnai G2 Polara microscope (FEI) equipped with post-column Quantum Energy Filter (Gatan) and a K2 Summit 4k x 4k direct detector camera (Gatan). Images were recorded at a nominal magnification of 34,000 with a pixel size of 0.61 nm. The dose rate was set to 10-12 e/physical pixel at the camera level. Frame exposure was set to 0.1 seconds, with a total exposure in a frame set to be determined by an algorithm targeting an average count number. The total dose in a tomogram was typically ~100-120 e/A^2 with a defocus of -5 μm. The dataset for this study consists of 16 tomograms from 7 FIB-milled lamellas. Reconstruction of tilt-series was done in IMOD (Kremer et al., 1996) using patch tracking method. Semi-automatic segmentation of the membranes was done using TomoSegMemTV (Martinez-Sanchez et al., 2014), an open-source software based on tensor voting, followed by manual segmentation with Amira software (FEI Visualization Sciences Group). Filaments were traced manually using Amira as well.

Point mutation graph

PA01 cells infected by PhiKZ were imaged 60 to 70 minutes post infection with DAPI staining. Infected cells were identified by the presence of a bright, circular DAPI stain in the center of the bacterial cells corresponding to the presence of phage DNA

within the phage nucleus. ImageJ (imagej.nih.gov/ij) was used to bisect infected cells and obtain GFP intensity profiles along their lengths. Each of these intensity profiles were normalized by the length of the cell and normalized again to the GFP intensity at the initial measured end of the cell. Intensity profiles were plotted per cell as well as averaged.

PDB structure of GFPmut1

The amino acid structure for GFPmut1 was used with the Phyre2 Protein Fold Recognition Server (www.sbg.bio.ic.ac.uk/phyre2) to obtain an estimated structure for GFPmut1 from pSG1729. This sequence differs from EGFP structure 2Y0G by substitutions V1M, L195S and L232H. The resulting structure was viewed with ChimeraX (www.rbvi.ucsf.edu/chimerax). Alignment of fluorescent proteins was made using Clustal Omega (https://www.ebi.ac.uk/Tools/msa/clustalo/)

DAPI quantification

Individual infected cells were cropped using ImageJ. A mask of the phage nucleus was generated using Otsu's method in Matlab 2017b and the mean DAPI fluorescence was calculated from the raw image intensity within the region of the mask. The complementary image to the mask was used to estimate background fluorescence.

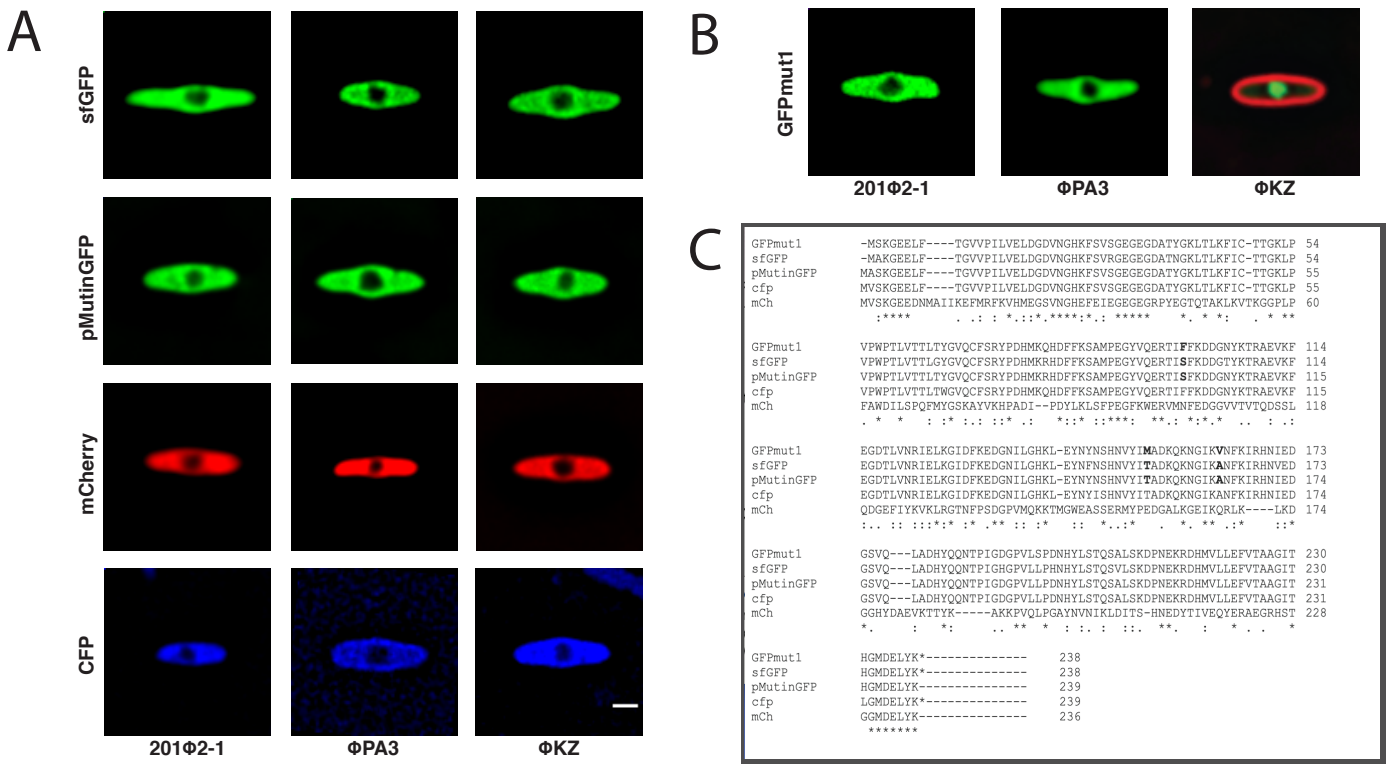

Figure 6.1: After infection, most fluorescent proteins localize to the bacterial cytoplasm and are excluded by the phage nucleus but GFPmut1 is transported into the ΦKZ nucleus. Scale bar = 1 micron

A. SfGFP, pMutinGFP, mCherry, and CFP are excluded by the phage nucleus in *P. chlororaphis* cells infected with 201Φ2-1 and *P. aeruginosa* cells infected with ΦPA3 or ΦKZ.
B. GFPmut1 localizes inside the ΦKZ phage nucleus while staying in the cytoplasm, excluded from both the 201Φ2-1 nucleus and ΦPA3 nucleus.
C. Alignment of the protein sequences of these fluorescent proteins, showing key differences in bold letters

Figure 6.2: One amino acid mutation is enough to transform the localization of GFPmut1

A. Three mutations in the GFPmut1 sequence separate it from newer fluorescent proteins. The mutations are all located on the beta-barrel but two (F99S, M153T) are on the outer surface while V163A is inside the barrel.
B. When these mutations were expressed, V163A results in nearly 100% localization inside the phage nucleus. M153T appears to localize inside and outside the nucleus in equal measure. F99S results in nearly 100% cytoplasmic localization, exclusion from the phage nucleus. Scale bar = 1 micron
C. Normalization of GFP intensity in these strains of GFPmut1 was used to quantify the localization of these point mutations in comparison with unaltered GFPmut1. GFPmut1 (n = 111), F99S (n=177), M153T (n=115), V163A (n=82) (Left) Each cell expressing GFPmut1 is represented with one black line, showing 100% inclusion into the nucleus. An almost identical phenotype is seen with the red lines representing cells with the V163 mutation. GFPmut1 F99S, shown with green lines, presents GFP intensity outside the nucleus, indicating 100% exclusion. M153T, represented by the blue lines, exhibits both inclusion and exclusion. (Right) A plot showing the averages of the individual cells graphed in the left plot. GFPmut1 in black and V163T in red indicate overall inclusion into the nucleus. F99S is represented by green line indicating exclusion. The blue line showing the average of M153T localization profiles is at baseline, showing that the average localization is at baseline.

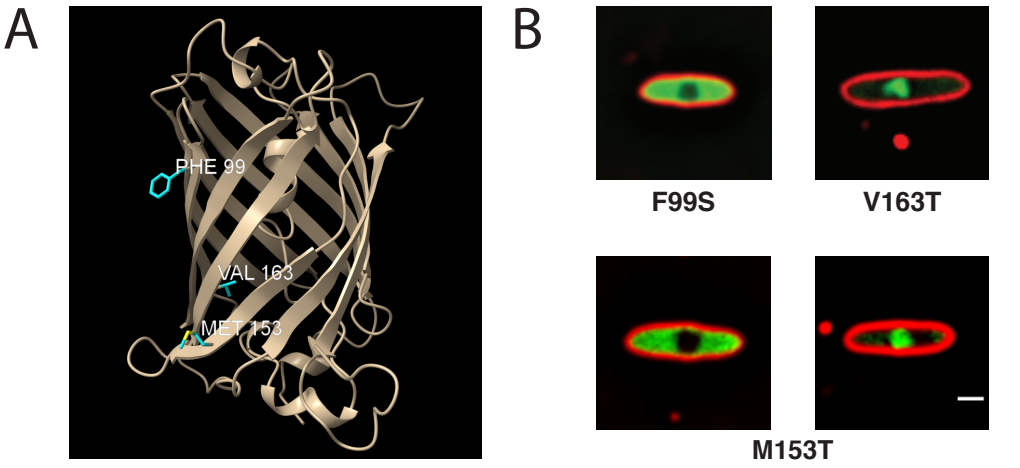
A
PHE 99
VAL 163
MET 153
B
F99S
V163T
M153T

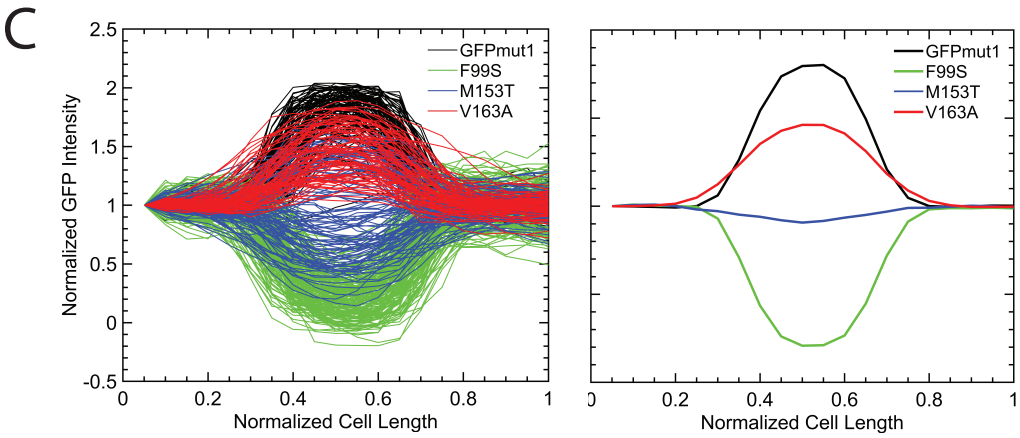
C
Normalized GFP Intensity
Normalized Cell Length
GFPmut1
F99S
M153T
V163A
Normalized Cell Length
GFPmut1
F99S
M153T
V163A

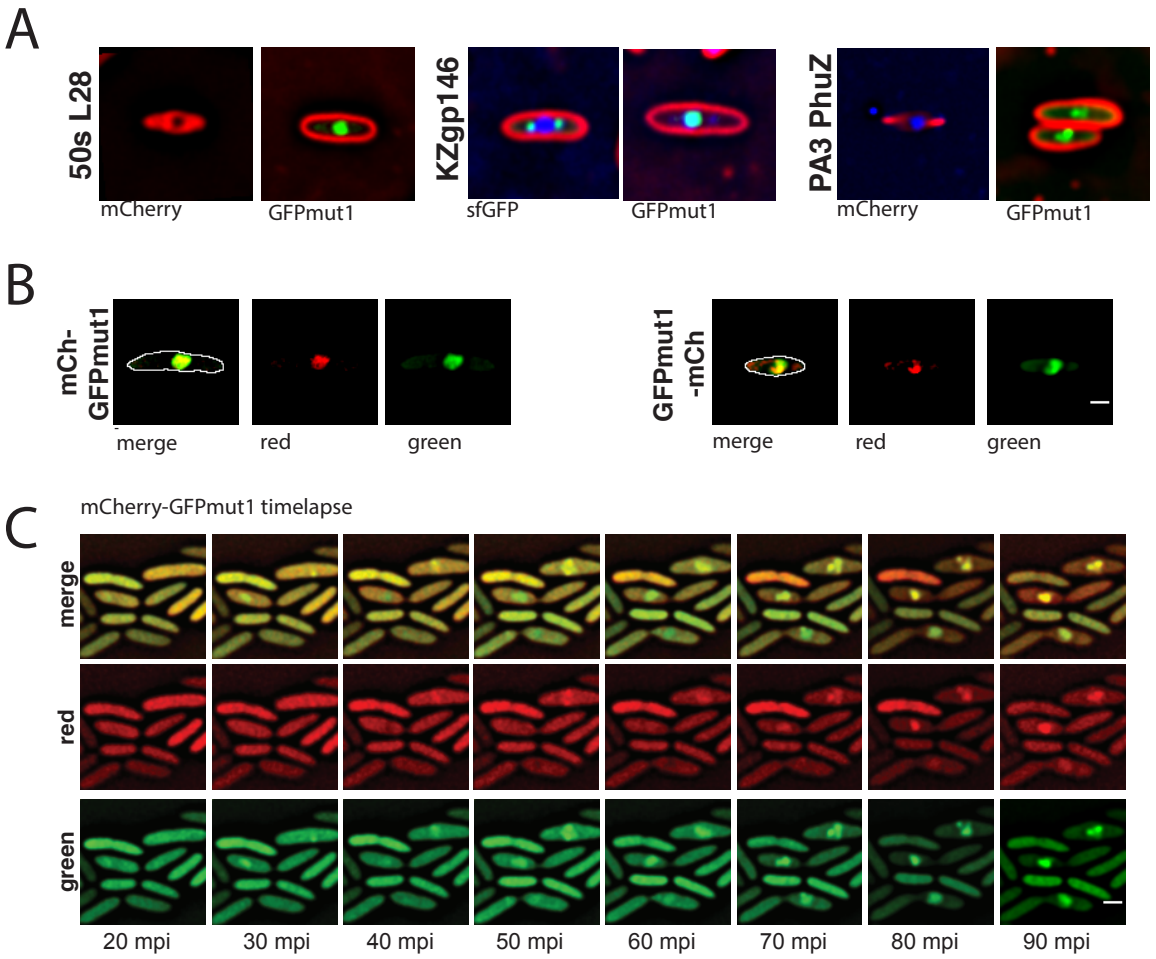

Figure 6.3: GFPmut1 alters the cell localization phenotype of any protein fused to it. Scale bar = 1 micron

A. Top: GFPmut1 fused to host protein 50s ribosomal subunit L28 localizes inside the phage nucleus while a fusion of the same protein to mCh localizes in the cytoplasm. Middle: GFPmut1 fused to ΦKZ tail protein gp146 is mislocalized inside the phage nucleus while a fusion of the same protein to sfGFP shows the classic tail phenotype of foci around the phage nucleus. Bottom: GFPmut1 fused to ΦPA3 PhuZ protein is seen inside the phage nucleus while a fusion of the same protein to sfGFP forms filaments in the cytoplasm.
B. GFPmut1 fused to mCherry at both the C-terminus and N-terminus show both proteins inside the phage nucleus. In addition, the ability of mCherry to fluoresce indicates that the protein is folded and functional as a protein.
C. Timelapse of mCh-GFPmut1 shows that both proteins are diffuse in the cytoplasm before infection but move into the nucleus as infection progresses.

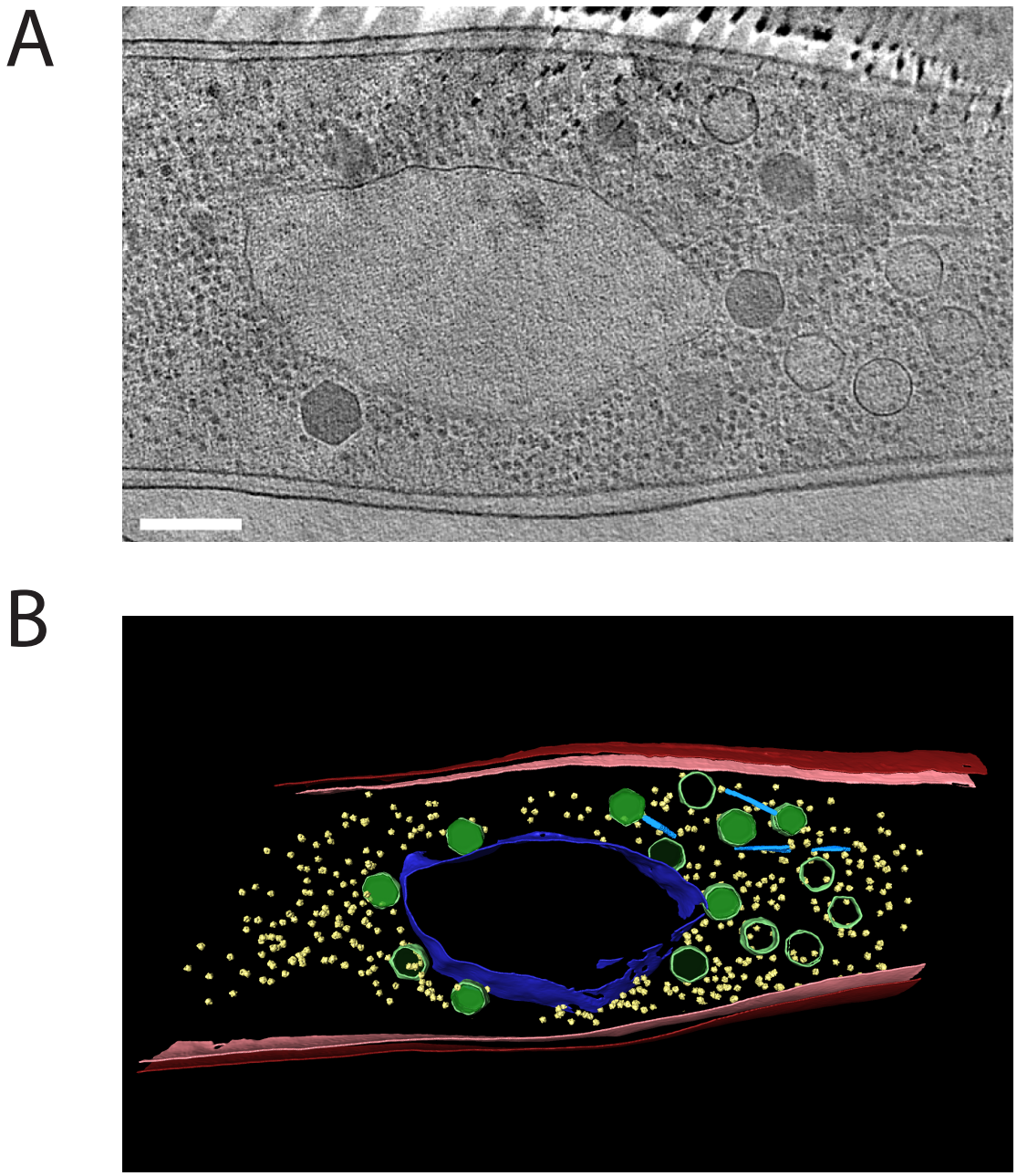

Figure 6.4: Cryo-EM Tomogram of a *Pseudomonas aeruginosa* cell infected with ΦKZ.

A. Slice through a tomogram of cryo-focused ion beam–thinned phage-infected cell at 60 mpi.
B. Segmentation of the tomogram shown in (A).

Figure 6.5: GFPmut1 can be used to artificially import proteins into the ΦKZ nucleus, even those that are detrimental to phage reproduction. Scale bar = 1 micron

A. SbcB-sfGFP and SbcB-GFPmut1 both hinder growth of *P. aeruginosa* when induced, compared to uninduced strains or strains expressing GFPmut1 alone.
B. SbcB-sfGFP shows localization of the fluorescent fusion outside the nucleus while sbcB-GFPmut1 shows the fusion inside the nucleus, with the phage DNA. In addition, cells expressing sbcB-GFPmut1 often have misshapen phage DNA compared to the smooth nuclei of cells expressing sbcB-sfGFP.
C. A histogram of DAPI (DNA stain) intensity indicates that cells expressing sbcB-mut1 (n=187) have lower intensity, compared to cells expressing sbcB-sfGFP (n=133). This suggests that DNA concentration is reduced by the presence of the host nuclease inside the phage nucleus.
D. GFPmut1 fused to the host nuclease SbcB reduces phage titer by 10-fold, compared to sbcB-sfGFP.
E. GFPmut1 can also be used to bring CRISPR proteins, which are normally excluded from the nucleus, as seen in the fusions of sfGFP, into the nucleus.

A

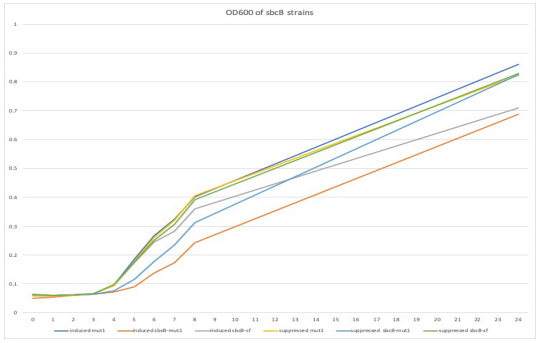

B

sbcB-sfGFP

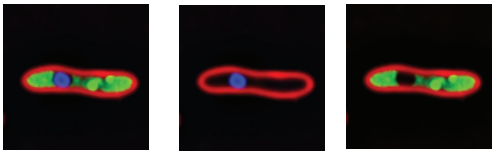

sbcB-GFPmut1

merge DAPI GFP

C

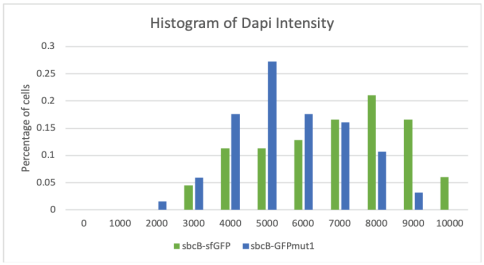

D

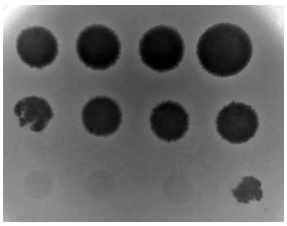

PhiKZ titer on SbcB-GFPmut1

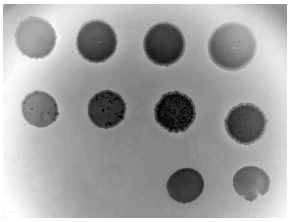

PhiKZ titer on SbcB-sfGFP

E

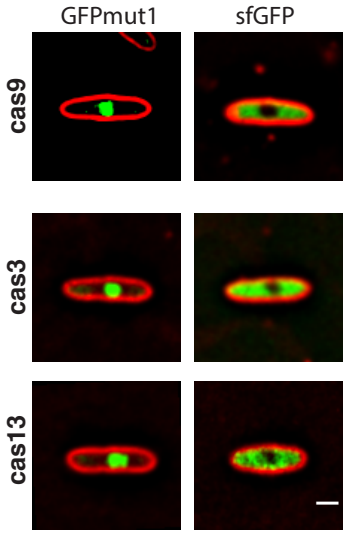

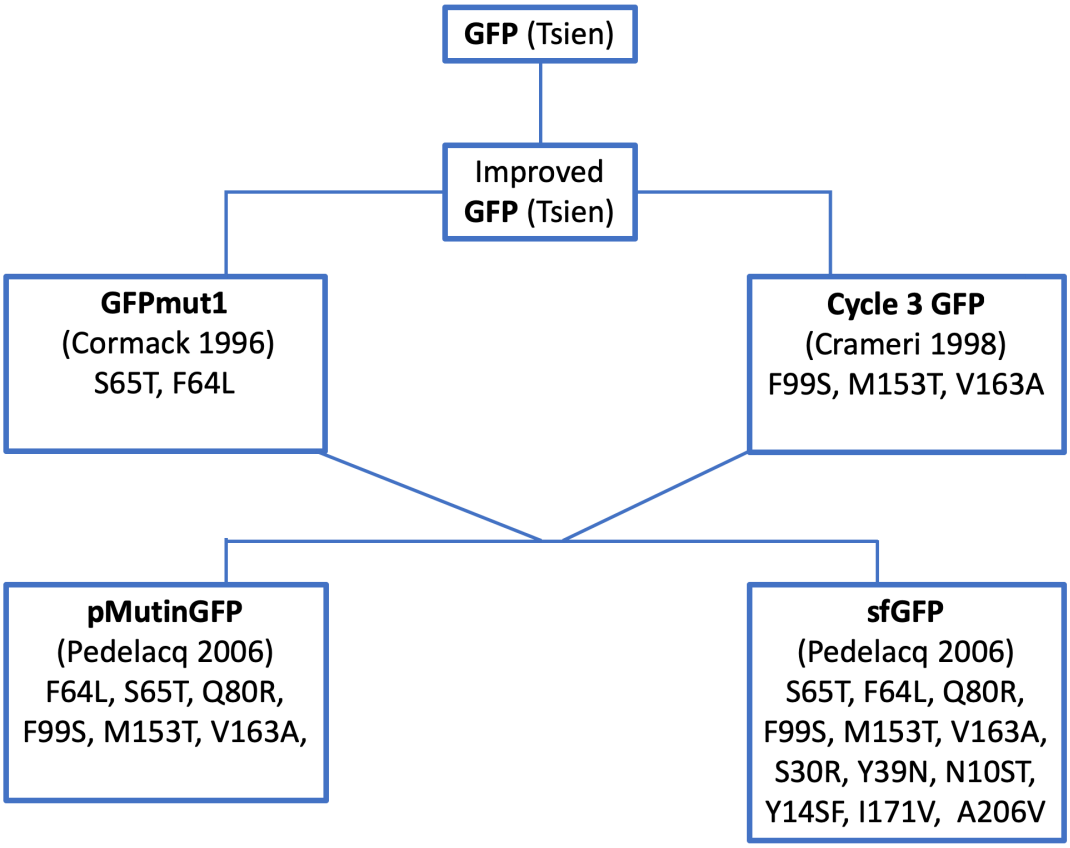

Figure S6.1: A chart showing the amino acid modifications of GFP variants over time.

Table 6.1: Strains and plasmids used in this study

KN155	*E.coli - DH5α*	pKN055	mCherry from PRSET-mCherry
KN156	*Pseudomonas chlororaphis*	pKN055	mCherry from PRSET-mCherry
KN157	*Pseudomonas aeruginosa (PA01)*	pKN055	mCherry from PRSET-mCherry
KN149	*E.coli - DH5α*	pKN053	GFPmut1 from pSG1729
KN150	*Pseudomonas chlororaphis*	pKN053	GFPmut1 from pSG1729
KN151	*Pseudomonas aeruginosa (PA01)*	pKN053	GFPmut1 from pSG1729
KN201	*E.coli - DH5α*	pKN69	sfGFP
KN202	*Pseudomonas chlororaphis*	pKN69	sfGFP
KN203	*Pseudomonas aeruginosa (PA01)*	pKN69	sfGFP
KN209	*E.coli - DH5α*	pKN70	pMutin GFP
KN210	*Pseudomonas chlororaphis*	pKN70	pMutin GFP
KN211	*Pseudomonas aeruginosa (PA01)*	pKN70	pMutin GFP
KN212	*E.coli - DH5α*	pKN71	CFP
KN213	*Pseudomonas chlororaphis*	pKN71	CFP
KN214	*Pseudomonas aeruginosa (PA01)*	pKN71	CFP
KN381	*Pseudomonas aeruginosa (K2733)*	pKN053	GFPmut1 from pSG1729
KN464	*E.coli - DH5α*	pKN152	GFPmut1 F99S
KN465	*Pseudomonas aeruginosa (PA01)*	pKN152	GFPmut1 F99S
KN466	*E.coli - DH5α*	pKN153	GFPmut1 M153T
KN467	*Pseudomonas aeruginosa (PA01)*	pKN153	GFPmut1 M153T
KN468	*E.coli - DH5α*	pKN154	GFPmut1 V163A
KN469	*Pseudomonas aeruginosa (PA01)*	pKN154	GFPmut1 V163A
KN473	*K2733 - PA01 pump knockout*	pKN152	GFPmut1 F99S
KN474	*K2733 - PA01 pump knockout*	pKN153	GFPmut1 M153T
KN475	*K2733 - PA01 pump knockout*	pKN154	GFPmut1 V163A
KN524	*K2733 - PA01 pump knockout*	pKN057	C-terminal GFPmut1 and 50sL28 (rpmB) from PA01 genome
KN525	*K2733 - PA01 pump knockout*	pKN70	pMutin GFP
KN526	*K2733 - PA01 pump knockout*	pKN151	WTGFP
KN527	*K2733 - PA01 pump knockout*	pKN71	CFP

Table 6.1 continued: Strains and plasmids used in this study

KN528	*K2733 - PA01 pump knockout*	pKN055	mCherry from PRSET-mCherry
KN529	*K2733 - PA01 pump knockout*	pKN69	sfGFP
KN569	*K2733 - PA01 pump knockout*	pKN62	C-terminal mCherry from PRSET and 50S ribosomal protein L28 from PA01 genome
KN513	*K2733 - PA01 pump knockout*	pKN166	C-terminal sfGFP and gp146 from PhiKZ genome
KN568	*K2733 - PA01 pump knockout*	pKN45	C-terminal GFPmut1 and gp146 from phiKZ genome

References

1. Tsirigotaki A, De Geyter J, Sostaric N, Economou A, Karamanou S. 2017. Protein export through the bacterial Sec pathway. Nat Rev Microbiol 15:21-36.

2. Patel R, Smith SM, Robinson C. 2014. Protein transport by the bacterial Tat pathway. Biochim Biophys Acta 1843:1620-8.

3. Chaikeeratisak V, Nguyen K, Egan ME, Erb ML, Vavilina A, Pogliano J. 2017. The Phage Nucleus and Tubulin Spindle Are Conserved among Large Pseudomonas Phages. Cell Rep 20:1563-1571.

4. Chaikeeratisak V, Nguyen K, Khanna K, Brilot AF, Erb ML, Coker JK, Vavilina A, Newton GL, Buschauer R, Pogliano K, Villa E, Agard DA, Pogliano J. 2017. Assembly of a nucleus-like structure during viral replication in bacteria. Science 355:194-197.

5. Pedelacq JD, Cabantous S, Tran T, Terwilliger TC, Waldo GS. 2006. Engineering and characterization of a superfolder green fluorescent protein. Nat Biotechnol 24:79-88.

6. Tsien RY. 1998. The green fluorescent protein. Annu Rev Biochem 67:509-44.

7. Crameri A, Whitehorn EA, Tate E, Stemmer WP. 1996. Improved green fluorescent protein by molecular evolution using DNA shuffling. Nat Biotechnol 14:315-9.

8. Phillips GJ, Kushner SR. 1987. Determination of the nucleotide sequence for the exonuclease I structural gene (sbcB) of Escherichia coli K12. J Biol Chem 262:455-9.

Acknowledgements

Chapter 6 is currently being prepared for submission for publication of the material. This chapter was co-authored with Joseph Sugie, Kanika Khanna, MacKennon Egan, Christopher Beierschmitt, Elizabeth Villa, and Joe Pogliano. The dissertation author was the primary investigator and author of this material.

Chapter 7: Conclusion and Perspectives

Assembly of a nucleus-like structure during viral replication in bacteria

Upon infection of *Pseudomonas chlororaphis*, phage 201Φ2-1 assembles a proteinaceous shell. This compartment encloses viral DNA as well as phage and host encoded proteins related to DNA and RNA. Outside of the compartment, localized in the cytoplasm, are host bacterial ribosomes and other proteins related to translation and metabolism. This structure is called the phage nucleus for its resemblance to the eukaryotic nucleus, specifically the separation of functions within a cell. The phage nucleus appears near one cell pole upon infection and grows in size, as DNA is replicated inside. PhuZ, a tubulin encoded by the phage, forms a bipolar spindle to push on the phage nucleus shell until it is centered in the infected cell. Capsids are packaged with DNA at the periphery of the phage nucleus.

This is the first account of compartmentalization of processes in a bacterial cell. In addition, the phage nucleus is the first instance of a bacteriophage constructing such an organized, regulated system during infection. We hypothesize that the phage nucleus evolved in this phage to streamline the process of phage reproduction with an exceptionally large genome.

The phage nucleus and tubulin spindle are conserved among large Pseudomonas phages

The major components of the 201Φ2-1 phage nucleus infection system are conserved in the related *Pseudomonas aeruginosa* phages ΦKZ and ΦPA3. All three phages encode the tubulin PhuZ, although the proteins show low similarity in terms of

amino acid sequence. Each homolog of PhuZ polymerizes into filaments *in vivo* and utilizes dynamic instability to center viral DNA in an infected cell. The viral nucleoid is enclosed by the phage nucleus shell, the major protein of which is also conserved in the three phages. In addition, homologs to UsvX/RecA are encoded by all three phage and localize inside the phage nucleus. Major capsid proteins are also conserved and localize on the edges of the phage nucleus, presumably for DNA packaging.

The conservation of the phage nucleus system shows that the reorganization of a bacterial cell is more widespread than first thought. Although the individual proteins in these phages generally have low sequence similarity to each other, their phenotypes and functions are conserved. In addition, our results show that the phages can recognize and perhaps utilize certain proteins from each other. Exploring the differences and similarities between these phages further will give us greater insight into the evolution of these phage species.

Viral capsid trafficking along treadmilling tubulin filaments in bacteria

Phage capsids from many species, including 201Φ2-1 and ΦPA3, are assembled on the host cell membrane. We showed that after assembly, the 201Φ2-1 and ΦPA3 capsids move along PhuZ filaments to the phage nucleus for DNA packaging. PhuZ uses dynamic instability early on during infection to center the phage nucleus at midcell. However, at a later point, PhuZ transitions to treadmilling, in which polymerization at the plus end of the filament is matched by depolymerization at the minus end. The exact mechanism of the functional switch is unclear but may be related to the overall cellular concentration of PhuZ. Treadmilling serves two purposes during infection: moving empty

capsids down the filament and rotating the phage nucleus for better positioning of capsids for DNA packaging.

Eukaryotic viruses are known to utilize cellular cytoskeleton proteins to move viral components for replication. However, this is the first evidence of a bacteriophage doing the same, utilizing its own cytoskeletal element in an infected bacterial cell. In fact, the movement of capsids along PhuZ is the first instance of cargo trafficking in bacterial cells. This study established the ability of PhuZ to treadmill in addition to using dynamic instability, as well as resolving the functions that pair with each mechanism of movement. Our results highlight the importance of the tubulin in phage reproduction as well as the plasticity of PhuZ.

Additional Components of the Phage Nucleus

The phage nucleus is enclosed by a proteinaceous border in all three phage systems. The major shell protein, gp105, was identified as the earliest and most highly expressed phage protein after infection with 201Φ2-1. Gp105 is also conserved in phages ΦKZ and ΦPA3 and fluorescent fusions to these homologs, PA3gp53 and KZgp54, show the same phenotype. However, we have identified two additional proteins that appear to be components of the phage nucleus shell. 201gp230 is the second-largest protein encoded by 201Φ2-1. Although evidence, including homologs that are annotated as tail proteins in the other phages, suggest gp230 is a tail protein, it also appears to be part of the shell. 201gp230 forms a ring in cross-section microscope and co-localizes with 201gp105. It is unclear how these proteins function as part of the phage nucleus

shell but identifying additional proteins that make up the phage nucleus will give us further insight into this novel structure.

Forcing selective transport into the phage nucleus

In the phage nucleus system, the default localization for unknown proteins appears to be cytoplasmic. In ΦPA3 or 201Φ2-1 infected cells, fluorescent proteins alone are excluded from the cytoplasm. However, we discovered that the ΦKZ infection system differs from in one major way. The fluorescent protein GFPmut1 is transported into the ΦKZ phage nucleus, but not that of ΦPA3 or 201Φ2-1. In addition, any protein fused to GFPmut1, either at the C-terminus or the N-terminus will also be transported into the ΦKZ phage nucleus. Therefore, we can utilize GFPmut1 to manipulate transport into the phage nucleus. This allows us to circumvent the natural protection of the phage nucleus and potentially edit the phage genome. In addition, exploring this mechanism of transport further could give us greater insight into the transport mechanisms of the phage nucleus.

Conclusion

The phage nucleus system highlights just how little we know about the vast world of phages. The phage nucleus is the first instance of a bacteriophage reorganizing an infected bacterial cell to resemble the eukaryotic nucleus. These ΦKZ phages utilize a tubulin spindle to center a nucleus-like structure that separates DNA and RNA processes from translation in the cytoplasm. In addition, intercellular trafficking of viral cargo occurs along treadmilling tubulin filaments. The major components of the phage nucleus mirror the defining hallmarks of eukaryotic cells. Subsequent characterization of the system

could shed light on the evolution of compartmentalization of processes in cells or even the genesis of eukaryotes.